Mesoscopic Distinct Element Method for Computational Design of Carbon Nanotube Materials

A DISSERTATION

SUBMITTED TO THE FACULTY OF

UNIVERSITY OF MINNESOTA

BY

Yuezhou Wang

IN PARTIAL FULFILLMENT OF THE REQUIREMENTS

FOR THE DEGREE OF

DOCTOR OF PHILOSOPHY

Advisor: Traian Dumitrică

July, 2017

Acknowledgement

Since I joined Department of Chemical Engineering and Materials Science in Spring 2013, I received extensive help on my graduate research from many people, both from inside and outside the University. Without their firm support, my work will not be accomplished.

I would like to express deep gratitude to my adviser Prof. Traian Dumitrică for his insightful guidance in my professional development from a student to a scientific researcher. During my four and half years working with him, I received both financial and technical support. It is his brilliant mind and passion that pave my academic path towards success.

I would like to sincerely thank my colleague, Dr. Igor Ostanin, who laid a strong foundation of the computational model used in this thesis. Through his mentorship, my early stage research became efficient and productive. I also appreciate the constant help from my other colleagues, Dr. Jihong Al-Ghalith, Dr. Yuxing Ni, Mr. Cristian Gaidau and Mr. Grigorii Drozdov for their support in my daily work.

I would like to acknowledge my collaborators from various institutes. I thank Prof. Erik Hobbie (North Dakota State University) for the experimental data and Prof. Catalin Picu (Rensselaer Polytechnic Institute) for his programming code. I thank Dr. Benjamin Jensen (NASA Langley Research Center) for the guidance and encouragement.

I would also like to thank the engineers and researchers of Itasca Consulting Group: Dr. David Protyondy, Dr. Sacha Emam, Dr. Matthew Purvance, Mr. Benjamin Harris, and Ms. Linh Wagner. Though Itasca Educational Program, they provided me software training and great instructions in problem solving.

Finally, I would like to thank National Science Foundation, MnDRIVE Informatics Assistantship, and NASA for financially supporting my research and writing this thesis.

Abstract

Carbon Nanotubes (CNTs) are hollow molecular cylinders conceptually formed by rolling single or multiple layers of graphene into tubes. CNT materials have become an attractive research subject during the last decades owning to the superior mechanical and electronic properties of individual CNTs. Developing applications, such as structural materials, supercapacitors, batteries or nanomechanical devices, depend on our ability to understand, model, and design the structure and properties of realistic CNT assemblies. Toward this goal, here we have applied a recently developed mesoscale computational method, titled the mesoscopic distinct element method (MDEM) that makes it possible to simulate the formation, stability, and mechanics of CNT aggregates and ultrathin CNT films. We first combine experiments and distinct element method simulations to understand the stability of rings and rackets formed by single-walled carbon nanotubes assembled into ropes. The obtained agreement validates MDEM and indicates that the stability of the experimental aggregates can be largely explained by the competition between bending and van der Waals adhesion energies. Next, we have considered the geometry and internal packing in twisted CNT ropes. Compared to the state of the art, MDEM accounts in a computationally tractable manner for both the deformation of the fiber and the distributed van der Waals cohesive energy between fibers. These features enable us to investigate the torsional response in a new regime where the twisted rope develops packing rearrangements and aspect-ratio-dependent geometric nonlinearities, in agreement with phenomenological models. Finally, we have performed MDEM simulations and developed an atomic-scale picture of the CNT network stress relaxation. On this basis, we put forward the concept of mesoscale design by the addition of excluded-volume interactions. Silicon nanoparticles are integrated into the model and the nanoparticle-filled networks present superior stability and mechanical response relative to those of pure films. The approach opens new possibilities for tuning the network microstructure in a manner that is compatible with flexible electronics applications. As a distinct direction, MDEM was explored for modeling the mechanics of nanocrystalline particles. Simulations that rely on the fitting of the peak stress, strain, and failure mode on the experimental testing of Au and CdS hollow nanocrystalline particles illustrate the promising potential of MDEM for bridging the atomistic-scale simulations with experimental testing data.

Table of Content

Acknowledgement i

Abstract ii

List of Table v

List of Figures vi

List of Publications xi

Chapter 1 Introduction 1

1.1. Fundamentals of Carbon Nanotubes 1

1.2. Modeling Techniques for Carbon Nanotubes 3

1.3. Multiscale Modeling 5

1.4. Organization of the Thesis 7

Chapter 2 Essentials of Mesoscopic Distinct Element Method (MDEM) 9

2.1. Introduction to Distinct Element Method (DEM) 9

2.2. MDEM for CNT Mesoscopic Simulations 10

Chapter 3 Verification and Validation of MDEM: Mechanics of Self-Assembled CNT Structures 15

3.1. Introduction 15

3.2. Stability and Structure of SWCNT Ring Windings 16

3.3. Bending of Crystalline SWCNT Ropes 24

3.4. Self-assembled Rings and Rackets from SWCNT Ropes 27

3.5. Concluding Remarks 38

Chapter 4 Nanomechanics of Twisted CNT Ropes 39

4.1. Introduction 39

4.2. Description of Highly Twisted CNT Rope Morphologies 41

4.3. Energetics and Mechanics of Bird Cage Transformation 45

4.4. Energetics and Mechanics of Helix Transformation 51

4.5. Reversibility and Stability of Twisted CNT Ropes 53

4.6. Packing Defects and Spontaneity of Twist 57

4.7. Concluding Remarks 59
Chapter 5 Carbon Nanotube Networks by Computational Design 61
5.1. Introduction 61
5.2. MDEM Representation of CNT Network 64
5.3. Development of Nanoparticle Contact Models 66
5.4. Relaxation and Bundling Effect 71
5.5. Elasticity and Deformation Mechanism 78
5.6. Cyclic Loading Condition 90
5.7. Concluding Remarks 95
Chapter 6 Mechanics of Nanocystalline Particles 98
6.1. Introduction 98
6.2. MDEM Representation of Nanocystalline Particle 100
6.3. Contact Models in Nanoparticle Assemblies 103
6.4. Elasticity and Plasticity of Au Nanoparticles 106
6.5. Brittle failure of CdS Nanoparticles 109
6.6. Concluding Remarks 110
Chapter 7 Conclusions and Future Research Directions 112
7.1. Conclusions 112
7.2. Future Research Directions 114
References 120
Appendix A 133
Appendix B 137

List of Table

Table 2-1 Parameters for the MDEM model of a (10,10) CNT used in simulations. 11

Table 2-2 Parameters used in adjusting the vdW contact model.[68] 14

Table 2-3 Explicit laws to determine forces and stiffnesses from the vdW contact model. 14

Table 3-1 vdW adhesion energy densities as a function of overlap Δl and number of turns n. For each n, the Δl range can be identified with Eq. 12. Coefficients $V_1 = 2.114$ eV/nm, $V_2 = 0.018$ eV/nm, and $V_3 = 0.007$ eV/nm represent the vdW interaction between 1 and 2, 2 and 4, and 2 and 5, respectively, in Figure 3-2a, right. They were obtained by direct integration of the microscopic vdW interactions (details obtained from Ref. [66]). 19

Table 3-2 Bending stiffness B as a function of the number of SWCNTs in the rope n. Results are obtained from four-point bending simulations conducted with MDEM. 27

Table 3-3 Values for the dimensionless coefficients α and β describing the vdW adhesion. x is the normalized total overlap length and n is the number of SWCNTs in the rope. Only rings with up to two turns are considered here. 31

Table 4-1 Summary of twist conditions and resulting morphologies shown in Figure 4-7. 51

Table 4-2 Summary of shift angles and energetics of three cases shown in Figure 4-13. 59

Table 5-1 Physical properties of CNT networks designed in MDEM models 65

Table 5-2 Parameters of CNT-CNT, CNT-NP and NP-NP vdW contact models. 71

Table 5-3 Young's Modulus of pristine CNT networks before and after relaxation measured from uniaxial tensile tests. 79

Table 5-4 Summary of uniaxial tensile tests of pristine and hybrid networks. Young's Modulus and percentage of CNTs in tension are measured at 2% strain before yield; Lateral shrinkage (i.e. necking) is measured at 20% strain. 90

Table 5-5 Young's Modulus (unit: GPa) measured in cyclic loading tests for pristine and hybrid CNT networks; 95% Confidence Interval is an estimation based on assumption of normal distribution. 94

List of Figures

Figure 1-1 Formation of CNT (a) Schematic of rolling graphene into CNT. (b) formation of an armchair CNT (5,5) from a graphene sheet (the shaded rectangle represents its unit cell) [12]. 1

Figure 1-2 Typical length and time scale for major modeling tools in materials science [48]. 5

Figure 1-3 Left: full-atoms representation of a CNT; right: Bead Spring model representation of a CNT segment [52]. 6

Figure 2-1 A sample diagram of velocity-Verlet algorithm used in DEM [64]. 10

Figure 2-2 Schematic illustration of contact models in MDEM: (a) Concept of coarse graining and representative element; (b) Parallel bond contact model; (c) vdW contact model. 12

Figure 3-1 Ring formation in SWCNT: (a) Scanning electron micrograph of a SWCNT sample; (b) Transmission electron microscope image of the ring wall section. [71] 16

Figure 3-2 MDEM simulations of ring windings assembled from a single (10,10) CNT with L = 340 nm, showing initial and final configurations. The final radii are (a) 38 nm and (b) 23 nm. ... 17

Figure 3-3 SWCNT cross-sections showing two models for the ring wall, a 2D (left) and 3D (right) model. V_1, V_2 and V_3 are vdW adhesion energy density between first, second and third nearest neighbors. (b) Analytical model predictions of the total potential energy as a function of the overlap length for the 2D (left) and 3D (right) wall models. 19

Figure 3-4 (a) A stable DEM simulated n = 3 winding with R = 35 nm. (b) Potential energy vs. overlap length for L = 680 nm showing both DEM (circles) and analytical (line) models. 21

Figure 3-5 Details of DEM simulations showing: (a) twisting in the wall of the n = 3 winding of Figure 3-4a and b; (b) local separation of SWCNT portions in the shown n = 5 winding. 22

Figure 3-6 (a) Set-up for four-point bending simulations conducted with MDEM. The down arrows indicate the location of the applied forces. The displacement in the scale bar is in Å. (b) Bending energy versus curvature squared for SWCNT ropes of various diameters. The inset shows the variation of the bending modulus with rope diameter. 25

Figure 3-7 (a) A ring (diameter = 250 nm, height = 15 nm) spontaneously formed in a dried suspension of SWCNT ropes (scale bar = 50 nm). (b)–(d) Knots and rackets formed during the deposition of length-enriched suspensions of individual SWCNTs (scale bar = 100 nm). The height legend for panels (b)–(d) is shown at the right. All shown structures are located on silicon wafer substrates. (Experimental preparation procedures are available in Appendix B) 28

Figure 3-8 (a) Ring with one turn formed by a rope containing 7 SWCNTs each 400 nm in length. The inset illustrates the sliding of SWCNT rope at the free end. The final ring diameter is 104 nm. The overlap length xL is also shown. (b) A ring winding with three turns formed by a 540 nm

long SWCNT. The final ring diameter is 64 nm. (c) Normalized total potential energy versus overlap for the two simulated ring morphologies, where the curves are predictions based on Eq. 20 and Table 3-3. Parameter z was set to -6.426 eV·nm^{-1} for the rope–rope and to -2.114 eV nm^{-1} for the tube–tube interactions.[78] In deriving z for rope–rope, we assumed a hexagonal close-packed rope structure and considered vdW tube–tube interactions up to the 3rd neighbor... 29

Figure 3-9 A 400 nm CNT self-assembled into racket shaped simulated by MDEM. 32

Figure 3-10 Total energy of self-assembled racket computed from both analytical model (Eq. 22) and MDEM simulations. 34

Figure 3-11 Racket morphology formed by (a) a 400 nm long rope containing SWCNT and (b) 460 nm (upper) and 900 nm (lower) SWCNTs. The lengths (widths) of the racket heads are 125 (76) nm, 77 (39) nm, and 70 (36) nm, respectively. (c) Total potential energy versus overlap the three simulated racket morphologies. The lines are predictions based on Eq. 23 and Table 3-3… 35

Figure 3-12 (a) Measured and computed ring diameter as a function of rope diameter with a linear fit. (b) Measured and computed racket head dimensions as a function of rope diameter with fits, as described in the text. Black markers are measured and gray (full and empty) markers are predicted by the models of Eq. 20 and Eq. 23. The number of SWCNTs in the rope n is also shown. 36

Figure 4-1 Carbon nanotube yarns manufactured through spinning process. 39

Figure 4-2 High twisted CNT morphologies: (a) bird cage structure formed by a short thick CNT rope (L = 40 nm, R = 10.8 nm and T = 52 nN·nm); (b) separation of bird cage due to over twist (T = 60 nN·nm); (c) spindle formed by long thin rope (L = 163 nm, R = 8.56 nm and T = 40 nm·nN); (d) a distorted rope due to over twist (T = 52 nN·nm). 42

Figure 4-3 (a) A CNT bundle sample labeled with defined length L and radius R. (b) Mid cross-section (shaded tubes are selected as effective calculation area). 44

Figure 4-4 (a) Rope morphologies at different twist angles β. Cross sections and Q values are shown below. The CNT length is L = 67.8 nm. (b) Time evolution of the energy stored in the parallel and vdW contacts and of Q. The light-gray area is the loading stage (steady loading with 1.0 nm·nN/ps). The dark-gray area is the stabilization stage under T = 64 nm·nN. A−D mark the rope morphologies shown in (a). 46

Figure 4-5 (a) Strain energies of twisted CNT rope with two boundary conditions. (L = 67.8 nm, R = 8.75 nm, T = 60 nm·nN and steady loading rate of 1.0 nm·nN/ps). Torsional loads are added in Phase I and maintained in Phase II (b) Local tensile force in twisted rope with sliding prohibited boundary condition (unit: eV/ Å) (c) Local tensile force in twisted rope with sliding allowed boundary condition (unit: eV/Å). 47

Figure 4-6 (a) “Bird caging” of a twisted CNT rope with L = 41 nm invisible in its cross-section

(top). The strain energy during “bird cage” formation. The light-gray area is the loading stage. The dark-gray area is the stabilization stage under T = 64 nm·nN (bottom). (b) Alternative “spindle morphology arising when the rope is only under geometric twist. In the cross-section, red and blue elements represent 5- and 7-fold packing defects, respectively. 48

Figure 4-7 Morphologies of twisted CNT rope under boundary two boundary conditions: constant moments (left) and twist relaxation (right). (a-b) T = 40 nm·nN; (c-d) T = 52 nm·nN; (e-f) T = 64 nm·nN. Ropes shown here have L = 67.8 nm and R = 8.7 nm. 50

Figure 4-8 (a-c) Straight-to-helix transformation in a rope with L = 163 nm. Color bars show the distribution of torsional moments (left) and bending moments (right) in unit of eV on the corresponding distinct element. (d) Time evolution of the strain energy stored in the parallel bonds. Light area I is loading (steady rate with 0.68 nN·nm/ps). Dark gray region IV is the stabilization stage where T = 64 nN·nm. A−C mark the morphologies shown in (a-c)..... 52

Figure 4-9 Helix formation of a highly twisted long-thin CNT rope (L = 326 nm, R = 8.75 nm) subjected to torsional moments (T = 60 nN·nm, loading rate = 0.53 nN·nm/ps) (a) Helix transformation initiated by a distorted rope axis. (b) Formation of winding. (c) Morphology of compact helices with four windings. Color bars show the distribution of bending moments magnitude on each element in unit of eV. 53

Figure 4-10 (a) Elastic and plastic twist of an N = 4 CNT bundle with various lengths. (b) A typical failure in plastic region II. 54

Figure 4-11 Twisted CNT rope morphology phase diagram. Pink region represents Bird Cage favored region; Light blue region represents stable spindles; White region is helix favored region. 56

Figure 4-12 Residual twist of defected bundle with their defect type presenting: (a) A line defect (b) Four point defects. 57

Figure 4-13 Shift angle of CNT bundle with three kinds of defects (view along axial direction): (a) Four-point defects; (b) A wide single-line defect; (c) Two narrow short-line defects (Blue and cyan color represent the left and right end, respectively). 58

Figure 5-1 MDEM representation of a medium size CNT network: (a) Pristine; (b) Hybrid with 2000 NPs (c) CNT network under electron microscopy [134]. 65

Figure 5-2 MDEM fitting of NP-NP potential using isotropic model in Eq. 25. 67

Figure 5-3 (a) Atomistic model of Si nanoparticle and a segment of CNT. (b) Atomistic model incorporated into MDEM representation. (c) Atomistic vdW interaction energy of a sliding nanoparticle along the CNT at equilibrium spacing of 0.346 nm. The periodicity of energy curve is a natural result of length of unit cell, but not artifact. (d) Mesoscopic potential corrugation due to isotropic model compared to modified anisotropic model..... 68

Figure 5-4 (a) Schematic illustration of NP-CNT interaction. (b) Plot of the NP-CNT vdW potential as obtained with the developed MDEM contact. 69

Figure 5-5 (a) MDEM simulated SWCNT network, measuring 500 nm x 500 nm x11 nm in size, after 4.5 ns relaxation. Color reflects the magnitude of the bending moments stored by the parallel contact bonds. Inset details a SWCNT bundle and a bent SWCNT. (b) Force chains (tension and compression) in the relaxed SWCNT network. 72

Figure 5-6 Property changes during the relaxation process of the medium size CNT network (a) Energy evolution (b) Number of aligned pairs (c) Pore size of the relaxed network compared to experimental data (d) CNT network prepared in experiments. 74

Figure 5-7 Particle influence on alignment: (a) A simple demo of two CNTs with a 30-degree crossing angle interfered by no particle, one particle and two particles on both sides. (b) Time evolution of aligned pairs of three configurations. 76

Figure 5-8 Number of aligned pairs in relaxation under the influence of NPs (a) Small size network (b) Medium size network (c) Relaxed medium size CNT networks in three cases: pristine, filled with 2000 NPs and 4000 NPs (correspond to a volume fraction of 4.8% and 9.5%). 77

Figure 5-9 Engineering stress-strain relations obtained through 2% uniaxial tensile tests on large size CNT networks. Particles are deposited either before or after relaxation. Moduli of pristine, 5000 NPs and 10000 NPs are measured as 9.5 GPa, 21.5 GPa and 22.8 GPa for unrelaxed network; 8.3 GPa, 13.3 GPa and 15.0 GPa for relaxed networks. 80

Figure 5-10 Role of nanoparticles in mechanics of CNT network. 81

Figure 5-11 Tensile force development within large size CNT network: (a) Pristine network under 1% and 2% strain; (b) Hybrid network with 10000 NPs under 1% and 2% strain. Particles are not shown for clarity. 83

Figure 5-12 Force chain (tension and compression) of large size CNT network under 2% tensile strain: (a) Pristine network; (b) Hybrid network filled with 10000 NPs. 84

Figure 5-13 (a) Engineering stress-strain curves and evolution of aligned pairs in large size pristine and hybrid CNT networks. Point A and B represent yield points of pristine and hybrid networks, respectively. (b) Pore size distribution in the initial and stretched CNT networks. Local microstructures highlighting opening of pores during stretching are shown below. 85

Figure 5-14 Medium size CNT network (same as in Figure 5-5a) under strain showing 37% transversal shrinking in the middle compared to the initial state. Color reflects the magnitude of the tensile force (above) and bending moment (below) stored by the parallel contact bonds. (a) Pristine; (b) Hybrid with 4000 NPs. 87

Figure 5-15 (a) Strain-Stress curves of pristine and hybrid medium size CNT films up to 300% strain. (b) Morphology of pristine film under 200% strain. (c) Morphology of hybrid under 200%

strain..... 88

Figure 5-16 (a) Energy dissipation and (b) Young's Modulus measured in each loading-unloading cycle with different strain rates. 92

Figure 5-17 Stress measure under cyclic loading condition for pristine and hybrid network with the reference of applied strain. 93

Figure 6-1 (a) Schematic representation of indentation test setup. (b) Force–displacement curves of elastic, plastic, and brittle bond contact models for a simple normal tension test. (c) Elastic response of a spherical nanoparticle averaged over 10 realizations, as compared to an analytical (Hertzian) solution. 102

Figure 6-2 (a) DEM stress–strain curves and (b) slip vector diagrams obtained in indentation tests of Au nanoparticle for different values of yield strength σ_y. 108

Figure 6-3 Brittle failure of a hollow CdS nanoparticle in indentation tests. Three DEM simulations were carried out: h = 40nm (test 1), h = 60nm (test 2), and h = 80nm (test 3). (a) Geometry of the particle. Color map gives magnitude of displacement. (b) Force–displacement curves of all three tests. 109

Figure 7-1 CNT Network configuration prepared for bending tests: (a) iso-view and (b) side-view. Loading slices are shown in red and gripped ends are shown in gray. (c) Bent pristine film shows flat center part. (d) Bent hybrid film shows curvy center part. 115

Figure 7-2 (a) Force vs. deflection curves obtained from bending tests on pristine and hybrid CNT networks. (b)Strain-stress curves of CNT networks with defects. 117

Figure 7-3 Crack development under 0%, 20% and 40% elongation strain (a) A flaw on the edge (b) A circular hole in the center 118

List of Publications

- **Wang, Yuezhou**, Drozdov, Grigory, Hobbie, Erik., Dumitrica, Traian, "Excluded volume approach for carbon nanotube network stabilization: A Mesoscopic Distinct Element Method Study", *ACS Applied Materials & Interfaces*, 2017, Volume 9, Issue 15, Pages 13611-13618.
- **Wang, Yuezhou**, Ostanin, Igor, Gaidau, Cristian, and Dumitrica, Traian, "Twisting carbon nanotube ropes with the mesoscopic Distinct Element Method: Geometry, Packing, and Nanomechanics," *Langmuir*, 2015, Volume 31, Number 45, Pages 12323 - 12327. (Cover Article)
- Ostanin, Igor, **Wang, Yuezhou**, Ni, Yuxiang, and Dumitrica, Traian, "Mechanics of nanocrystalline particles with the Distinct Element Method," *Journal of Engineering Materials and Technology*, 2015, Volume 137, Issue 2, Pages 024501.
- **Wang, Yuezhou**, Semler, Matthew R., Ostanin, Igor, Hobble, Erik K., and Dumitrica, Traian, "Rings and rackets from single-wall carbon nanotubes: manifestations of mesoscale mechanics," *Soft Matter*, 2014, Volume 10, Pages 8635 - 8640.
- **Wang, Yuezhou**, Gaidau, Cristian, Ostanin, Igor, and Dumitrica, Traian, "Ring windings from single-wall carbon nanotubes: A distinct element method study," *Applied Physics Letters*, 2013, Volume 103, Pages 183902.

Chapter 1 Introduction

1.1. Fundamentals of Carbon Nanotubes

Since their discovered in 1991, [1] Carbon Nanotubes (CNTs) have continuously attracted tremendous interests in both scientific and industrial application fields. Owing to their remarkable mechanical, electrical and thermal properties, [2-7] CNTs have shown promising potential in a myriad of applications, such as biosensor, structural support, supercapacitor, energy storage and flexible electronics. [8-11]

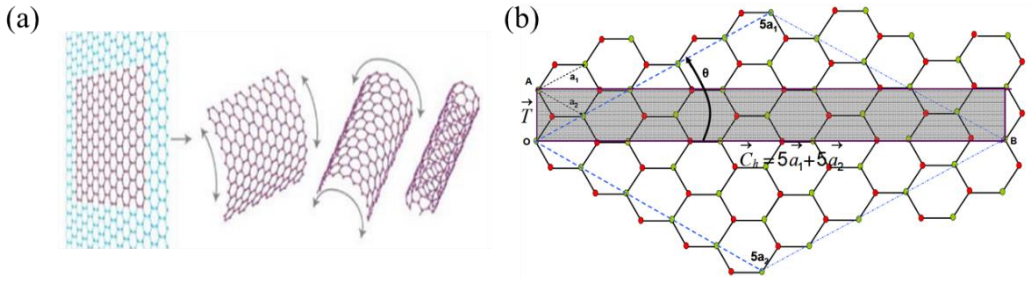

Figure 1-1 Formation of CNT (a) Schematic of rolling graphene into CNT. (b) formation of an armchair CNT (5,5) from a graphene sheet (the shaded rectangle represents its unit cell) [12].

The properties of individual CNTs are dictated by their morphologies. CNTs have a structure that is conceptually described as a graphene sheet seamlessly rolling up into a tubular structure with different chiral vectors ($\overrightarrow{C_h} = n\overrightarrow{a_1} + m\overrightarrow{a_2}$): zigzag ($n$, 0), armchair ($n$, n), and chiral (n, m) (Figure 1-1). The chiral vector is not only a structural character for each species of CNT and but also determines its metallic or semi-conductive properties. The common production process usually involves arc discharge, laser ablation or chemical vapor deposition of carbon-containing gas [13-16]. There are two types of

pristine CNTs that can be synthesized: single-wall and multiwall. Grown for example from cobalt catalyst nanoparticles [17], the single-wall carbon nanotube (SWCNT) has simple geometry with a typical size of ~1 nm in diameter and length of a few microns. The scale of CNT bulk materials ranges vastly from nanometer to centimeters forming various self-assemblies: rings, yarns, thin films and buckypapers, which are essential components for CNT-based devices. CNT thin film, for instance, can be manufactured into transistors by aerosol jet printer [18]. With high mobility (~52 cm^2 V^{-1} s^{-1}) and small resistance (~25 kΩ/sq) [19], CNT transistors become an excellent candidate for flexible electronics. CNT yarns assembled by forest spinning or drawing methods [20], achieve a stiffness of 357 GPa [21] and density as small as 0.8 g/cm^3. In the foreseeable future, CNT yarns could be utilized in aerospace, defense as well as biomedical industry, where lightweight ultra-strong materials are always demanding.

Undoubtedly, the development of such promising CNT-based devices heavily relies on the understanding on their structure-property relationship. In this aspect, direct experimental measurement is often challenging due to high instrumental cost and CNT's small scale, which hinders the new materials into application. Modeling, on the other hand, resolves such difficulties by providing predictive guidance in materials design and has become an essential research tool for nanoscience.

1.2. Modeling Techniques for Carbon Nanotubes

With the rapid growth of computation capability, computer aided modeling becomes a powerful tool for studying materials. Developed in 1960s, finite element method (FEM) is currently the dominating simulation methodology across almost every branch of industry and science, especially after its implementation in user friendly commercial software. Nonetheless, the assumption of continuum mechanics in FEM limits the application of this method at the nanoscale where materials start to demonstrate their discretized nature. There are some FEM studies on CNT systems, yet most of which are either single tube [22-24] or macroscopic continuous buckypaper [25].

Around the same period of FEM development, Molecular Dynamics (MD) [26] was proposed as a simulation method to study materials at the atomistic level. In MD, atoms are considered as material points whose interactions are described by analytical or empirical energy functions known as interatomic potentials. Being able to evolve in time millions of atoms in a typical time scale of nanoseconds, MD is applied to study the emergent properties in materials science, biophysics, and pharmaceutical engineering. [27]

In terms of CNT systems, MD has been widely used to conduct bending, tensile, compressive tests [28-30] and study the defect impacts [31, 32] on single or multiple tubes. Besides mechanical properties, MD is also a reliable tool to model thermal transport [33-35] and interaction of chemical functional groups [36]. Abundant studies based on MD have

provided fundamental understanding of CNT's properties that may be challenging to access from direct experimental measurements and tests. The intermolecular force for the carbon-carbon bond can be described by empirical potentials, such as Tersoff [37] or Stillinger-Weber potential, [38] while the van der Waals force between tubes is derived from classic Lennard-Jones potential: [39]

$$V(d) = 4\varepsilon_0 \left[\left(\frac{d_0}{d}\right)^{12} - \left(\frac{d_0}{d}\right)^{6} \right], \quad (1)$$

where d is the atom spacing, two constants are $d_0 = 0.385$ nm and $\varepsilon_0 = 0.004$ eV for carbon atoms. Newton's laws of motion are used to calculate the displacement of each atom by assuming constant acceleration within a microscopic time interval (~fs). A series of mechanical properties and phenomena have been studied by MD, namely, Young's Modulus, tensile strength, fracture, buckling and friction etc.,[28, 35, 40-43] which provided the fundamental insights of CNT behaviors.

Albeit MD is a fine modeling tool capable to more simulate up to millions of atoms with a time scale of several nanoseconds，for complex CNT assemblies and systems at larger scale (10^{-7}-10^{-6} m) or longer time evolution (~10^{-5} s), accumulating errors and tedious computations for tracking the motions of individual atoms make MD inefficient and even computationally prohibitive. With the experimental synthesis of ultra-long CNTs achieved, [44-46] to investigate CNT systems at realistic scale becomes urgent. In this aspect, multiscale simulation method shows its advantages.

1.3. Multiscale Modeling

As a relatively new concept, multiscale modeling has attracted research interest since late 1990s, mainly because of the advent of parallel computing. In industry, multiscale modeling has been applied to reduce the product development time and helped reduce the cost of system design. [47] In materials science, multiscale modeling is crucial in bottom-up materials design. By controlling the species and particular arrangement of atoms, for instance, one could evaluate the materials properties and reflect further into macroscopic behaviors for various application purposes.

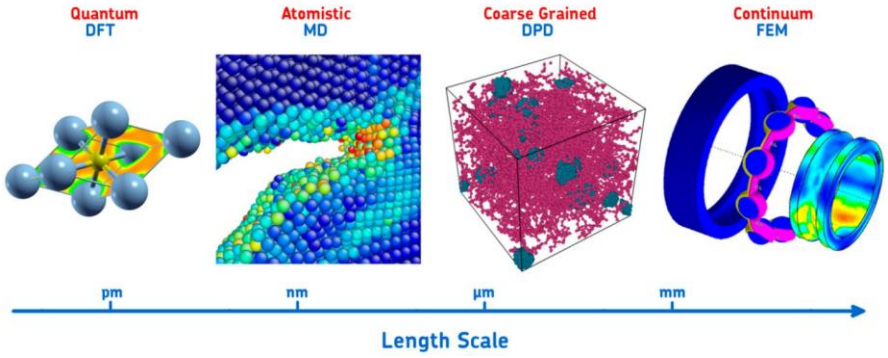

Figure 1-2 Typical length and time scale for major modeling tools in materials science [48].

Both MD and FEM, as discussed before, are modeling techniques in nanoscale and continuum materials, respectively. Despite its crucial role in the chain of multiscale modeling, mesoscale defined in length scale of microns is not well studied and yet has great significance. In mesoscale, CNT materials reveal tremendous variability in topology and a wide range of observable material defects with remarkable impacts on material properties and behaviors. A new modeling tool is required to span the gap between MD

and FEM models and to provide insights that are currently not accessible from experimental techniques. A common strategy is coarse graining, meaning to represent a system by a reduced number of degrees of freedom. [49-51] In comparison with all-atom representation, coarse grained MD generally requires less computational resource and can be extended to mesoscale.

Inherited from the studies of thermal dynamics of polymer solutions, the bead-spring (BS) model is often used to describe the mechanics of CNT. In BS model, a CNT can be represented by a chain of point masses connected by linear springs (Figure 1-3). The length r and relative angle θ capture the tensile and bending deformation. Depending on the scale of simulation, r can be chosen to represent hundreds of atoms. Intertube vdW forces are calibrated through all atoms MD simulations.

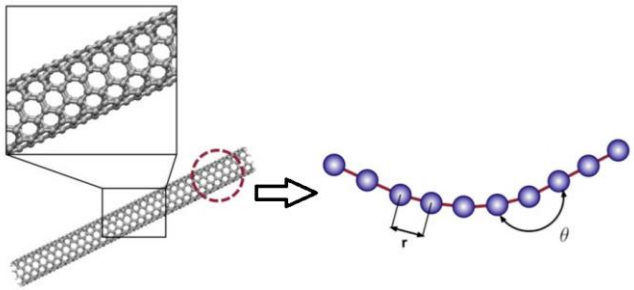

Figure 1-3 Left: full-atoms representation of a CNT; right: Bead Spring model representation of a CNT segment [52].

BS model has been implemented in MD and used to study self-assembling phenomena in single CNT system [52, 53] and CNT networks [54-56]. Nonetheless, the deficiency of BS model is also manifest. First, the point mass representation neglects the

cylindrical shape of the CNTs. Second, upon sliding, the vdW potential energy between two CNTs is expected to be smooth. However, the isotropic representation of the vdW potential will lead to strong corrugation. Third, the simple linear spring is unable to describe twisting and shear, which are essential components in full deformation modes.

Our current modeling technique, Mesoscopic Distinct Element Method (MDEM) overcomes these difficulties and is able to model the genuine mechanics at the mesoscale. It is an innovative adoption of conventional distinct element method, widely applied in geomechanics and civil engineering to solve the interaction between discretized objects, such as rocks and sand particles. Discussed in Chapter 2, the development of vdW contact models extends DEM to the mesoscale. The extension of DEM to the mesoscale makes this method promising for bridging the gap between atomistic and continuum mechanics simulations.

1.4. Organization of the Thesis

The thesis focuses mainly on validations and applications of MDEM. In Chapter 2, a review of MDEM development will be briefly discussed. The major part of this thesis is organized based on my own published works in [57-61][1]. Chapter 3 discusses verification and validation of MDEM through both analytical and experimental studies of CNT self-assemblies, followed by and an in-depth investigation of twisted CNT ropes in

[1] Copy rights are granted or permitted by AIP Publishing, Royal Society of Chemistry, American Chemical Society and American Society of Mechanical Engineers.

Chapter 4. MDEM is applied to understand topological defects and twist-to-helix transformation.

Chapter 5 explores the nanomechanics of CNT network (thin film). A complex CNT network in size of microns is constructed by MDEM. An accurate description of relaxation process is validated by comparing experimental measurements such as pore size distribution, density and degree of bundling. Mechanical properties are accessed through uniaxial tensile tests. In addition to a parametric study of various parameters that dictate the mechanical behaviors, a concept of nanoparticles is also introduced to manipulate the nanostructure in terms of the stability control and better load transfer ability. The concept of excluded volume repulsion explains the role of particles in network topology.

Chapter 6 is an extending work of MDEM applied in Au and CdS nanocystalline particles. Mechanical deformation through compression tests is investigated including elasticity, plasticity and fracture. Adapting different contact models in fracture mechanics enables a description of both ductile and brittle failure.

Chapter 7 concludes the thesis and manifests possible future research directions in general CNT systems, biological materials as well as comprehensive studies in CNT network.

Chapter 2 Essentials of Mesoscopic Distinct Element Method (MDEM)

2.1. Introduction to Distinct Element Method (DEM)

Distinct element method (DEM) is a computational modeling tool that deals with mechanical behaviors of discretized assemblies and particles. DEM was firstly developed in 1971 by P. Cundall, [62] initially aiming to solve soil particles response to pressure or disturbances. Afterwards, DEM is regarded as an important simulation technique in civil and petroleum engineering [63] to model interaction of sand and rock particles. Similar to MD, DEM models spherical particles or elements as rigid bodies. The contact models between two elements are described by linear springs with normal and shear stiffness, k_n and k_s, respectively. At each time step, contacting forces are identified and calculated for each element tracked in the Lagrangian frame. Regarding the translational and rotational degrees of freedom, the instantaneous displacements, linear and angular velocities are determined through the velocity-Verlet algorithm detailed in Figure 2-1 and the following equations:

$$\boldsymbol{x}(t+\Delta t) = \boldsymbol{x}(t) + \boldsymbol{v}(t+0.5\Delta t)\Delta t, \tag{2}$$

$$\boldsymbol{v}(t+0.5\Delta t) = \boldsymbol{v}(t-0.5\Delta t) + \frac{\boldsymbol{F}(t)}{m}\Delta t, \tag{3}$$

$$\boldsymbol{\omega}(t + 0.5\Delta t) = \boldsymbol{\omega}(t - 0.5\Delta t) + \frac{\boldsymbol{M}(t)}{I}\Delta t, \quad (4)$$

where $\boldsymbol{x}$ is displacement, $\boldsymbol{F}$ and $\boldsymbol{M}$ are force and moment acting on the object, $\boldsymbol{v}$ and $\boldsymbol{\omega}$ are linear and angular velocities, t is time and Δt is specified time step.

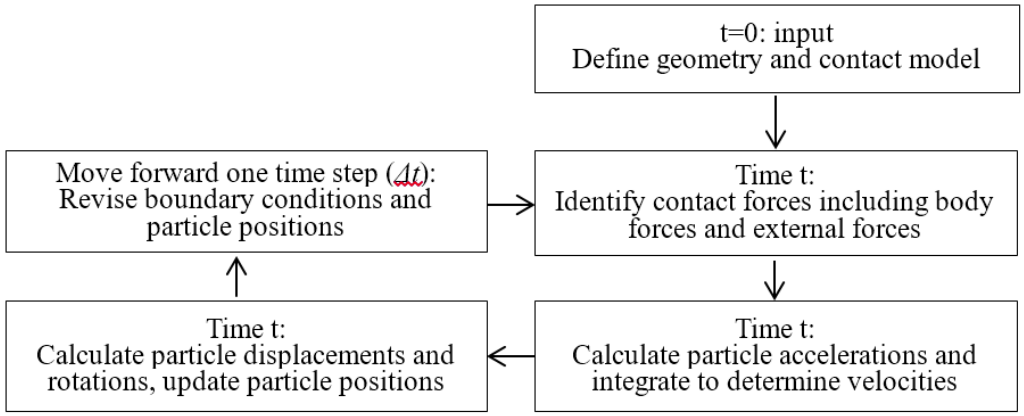

Figure 2-1 A sample diagram of velocity-Verlet algorithm used in DEM [64].

2.2. MDEM for CNT Mesoscopic Simulations

By introducing the microscopic van der Waals (vdW) interaction as a non-traditional contact model to DEM, our research group has enabled efficient simulations of the dynamics of the ultra-long CNT systems with complex configurations. [65, 66] The key advantage is the significant reduction of atomistic degrees of freedom while maintaining the accuracy of mesoscale mechanics. The modified DEM is then implemented in a commercial available software PFC3D (Particle Flow Code in Three Dimensions) [67] developed by a geotechnical company, Itasca Consulting Group, headquartered in Minneapolis, MN.

Our current MDEM model is built for a (10, 10) single wall carbon nanotube (SWCNT) with radius $r_{CNT} = 0.68$ nm. A SWCNT is firstly treated as a cylindrical elastic shell containing a chain of distinct mass representative elements (RE). Each RE has length $T = 1.36$ nm and thickness $t = 0.336$ nm, including approximately 220 carbon atoms (Figure 2-2a). Two main contact models are developed to encapsulate the short and long range atomistic interaction.

The first contact model, the parallel bond contact model (Figure 2-2b), describes the elastic response between two adjacent elements in a single CNT. The relative displacements of the two elements are resolved under the direct of versors *n* and *s*, located in and perpendicular to the contact plane. On one hand, the element normal and shear relative displacements U_n and U_s are resisted by forces F_n and F_s, respectively. On the other hand, the relative rotation angles θ_n and θ_s are resisted by moments M_n and M_s, respectively.

Table 2-1 Parameters for the MDEM model of a (10,10) CNT used in simulations.

A (nm^2)	I (nm^4)	J (nm^4)	k_n (eV/nm^4)	k_s (eV/nm^4)
1.427	0.348	0.696	4740	2110

To model elasticity, these forces and moments are generated by linear-elastic normal k_n and shear k_s springs that are uniformly distributed over a finite-sized section lying on the contact plane. The explicit laws are $F_n = -k_n A U_n$, $F_s = -k_s A U_S$, $M_n = -k_s I \theta_s$, and $M_s = -k_n J \theta_n$, where $A = 2\pi r_{CNT} t$, $I = \pi r_{CNT} t(r_{CNT}^2 + 0.25t^2)$, and $J =$

$2I$ are the area, moment of inertia, and polar moment of inertia of the parallel bond ring. Normal and shear stiffness are obtained from Young's and shear moduli (Table 2-1). In the above laws, we highlight the need for a rigid body treatment of the coarse-grained elements to resolve the resistance to a torsional deformation. The chain of parallel-bonded distinct elements describes the CNT as an Euler-Bernoulli beam. In lieu of point mass generally used in the conventional bead-spring model (BS model), MDEM can capture tension and bending, as well as shear and torsion, which provides a comprehensive study on mechanical properties of CNTs.

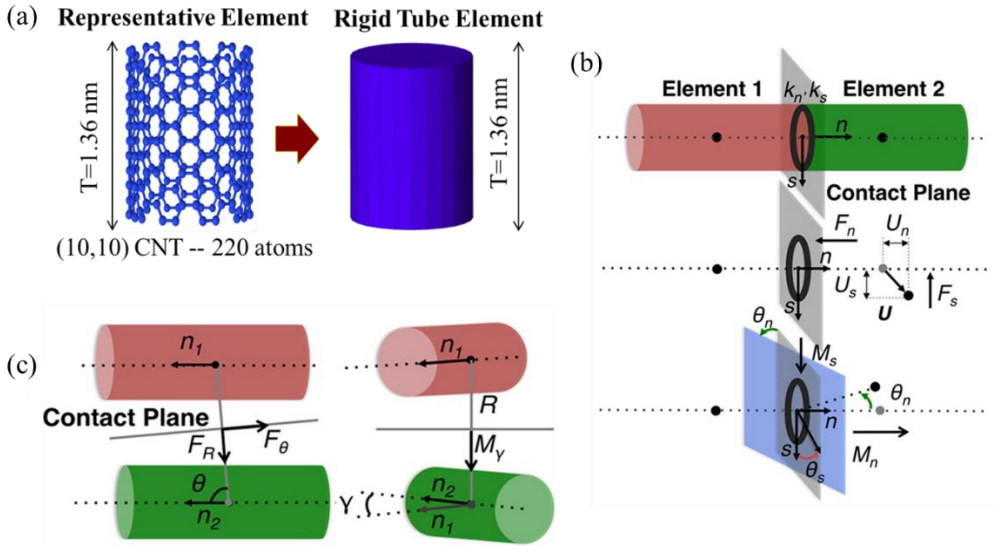

Figure 2-2 Schematic illustration of contact models in MDEM: (a) Concept of coarse graining and representative element; (b) Parallel bond contact model; (c) vdW contact model.

The second contact model deals with the long range vdW interaction between elements on two different CNTs (Figure 2-2c). This contact has been developed via a procedure that involves the integration of the atomistic vdW interactions between two

CNTs determined by the surface integral of L-J potential (Eq. 1) for all the carbon atoms from two CNT surfaces. Around the equilibrium distance, this potential is always negative. For each pair of elements, the vdW energy integral is evaluated numerically and can be eventually expressed as $U(R,\theta,\gamma)$ through Eq. 5 – Eq. 8:

$$U(R,\theta,\gamma) = f_c(R)V(R,\theta)M(R,\gamma), \tag{5}$$

$$V(R,\theta) = \varepsilon\left(\frac{A}{D(R,\theta)^{\alpha}} - \frac{B}{D(R,\theta)^{\beta}}\right), \tag{6}$$

$$M(R,\gamma) = 1 + W(R)(1 - cos(2\gamma)), \tag{7}$$

$$D(R,\theta) = \frac{R}{r_{CNT}\delta(\theta)} - 2, \tag{8}$$

where V is the interaction energy, M is the correction function concerning the interactions between crossed elements and aligning moment and f_c is the cut-off distance function. The constants A, B and ε are given in Table 2-2. We use normalized dimensionless distance $D(R,\theta)$ and the factors $\delta(\theta)$ and $W(R)$ are Fourier's fitting functions of the numerical solutions (see [65] for mathematical derivations). The contact force and stiffness are then built based on the first and second derivatives of the vdW interaction energy (Table 2-3). It is noted that only to avoid the corrugation artifacts and to describe the vdW energy lowering when CNTs are crossing, U is anisotropic, i.e., it depends not only on the center-to-center distances R but also on the θ and γ alignment angles.

Table 2-2 Parameters used in adjusting the vdW contact model.[68]

ε (meV)	A	B	α	β
149.3	0.0223	1.31	9.5	4

Table 2-3 Explicit laws to determine forces and stiffnesses from the vdW contact model.

Normal force	$F_R = \frac{\partial U}{\partial R}$	**Normal Stiffness**	$k_R = \left\|\frac{\partial^2 U}{\partial R^2}\right\|$
Shear force	$F_\theta = -\frac{1}{R}\frac{\partial U}{\partial \theta}$	**Shear Stiffness**	$k_\theta = \left\|\frac{1}{R^2}\frac{\partial^2 U}{\partial \theta^2}\right\|$
Aligning Moment	$M_\gamma = -\frac{\partial U}{\partial \gamma}$	**Aligning Stiffness**	$k_\gamma = \left\|\frac{1}{R^2}\frac{\partial^2 U}{\partial \gamma^2}\right\|$

The addition of the aligning moment to the vdW contact model makes it distinct from the previous BS model, where the huge adhesive shear strength prohibits relative sliding between tubes. Besides, the smoothness of intertublar potential with no artificial corrugations guarantees the sliding between two CNTs is captured in a correct manner. As will be shown in Chapter 3 and 5, sliding is essential for the self-assembling process of CNT structures, such as CNT rings, rackets, and networks. From thermodynamics point of view, sliding is also responsible for energy dissipation. It is noted that the elements in vdW contact will also experience forces resulting from a viscous damping contact representing the microscopic energy loss during such sliding.

Chapter 3 Verification and Validation of MDEM: Mechanics of Self-Assembled CNT Structures[2]

3.1. Introduction

Carbon nanotube rings and rackets are spontaneously assembled fibrous aggregates that store significant amount of bending energy, while naturally stabilized. Besides CNTs, the observation that similar shapes exist in several fibrous biological materials has prompted the hypothesis that it is the slender fiber geometry that lies at the origin of such shapes, as opposed to molecular structure of various species. It is therefore critical to understand the stability mechanism, an energy competition between bending and intermolecular attraction. Due to the simplicity and well-organized structures, CNTs serve an ideal system to fully investigate this hypothesis. This chapter focuses on a variety of self-assembled defect-free CNT aggregates, namely, rings and rackets, made by single or bundled tubes. Meanwhile, from a combined mesoscale modeling and experimental point of view, such study has not been pursued and will also be an excellent demonstration of the effectiveness and accuracy of MDEM. The approach reveals the importance of mesoscopic mechanics in agglomerates formation and the appeal of these morphologies for understanding the elastic and adhesion attributes of nanoscale fibers.

[2] This chapter has been published in *Applied Physics Letter* (DOI: 10.1063/1.4827337, 2013) and *Soft Matter* (DOI: 10.1039/C4SM00865K, 2014)

3.2. Stability and Structure of SWCNT Ring Windings

The CNT ring is one of self-assembled structures that have been discovered in experiment (Figure 3-1). [69-71] Their deformations and physics have been addressed in a few studies. [72-75] Inspired by the self-folding and unfolding phenomena, [52, 76] the study focused on the dynamics of ring formation based on an analytical continuum mechanics model. Simulations of its possible metastable states were used to predict CNT rings' usefulness in mechanical energy storage.

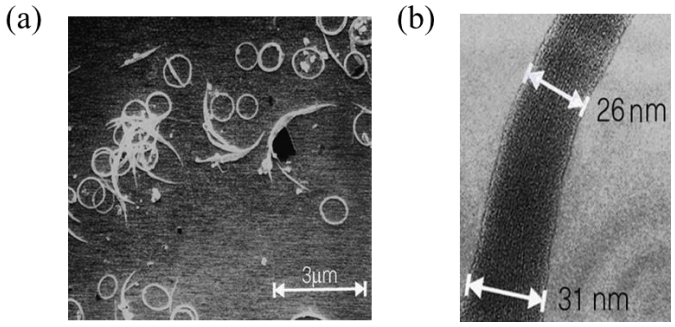

Figure 3-1 Ring formation in SWCNT: (a) Scanning electron micrograph of a SWCNT sample; (b) Transmission electron microscope image of the ring wall section. [71]

The CNT ring formation process is dominated by intertubular vdW forces. When the two ends of the CNT are bent to meet, they will become attached by vdW attractive forces. [52, 76] The potential energy of this ring system is proven to be reduced for further overlapping of the two ends. [77] Ipso facto, gliding of two ends is expected to occur until reaching the equilibrium state, at which the vdW potential balances the increase of strain energy. This mechanism could lead to several metastable ring structures which wind themselves more than once (Figure 3-2b).

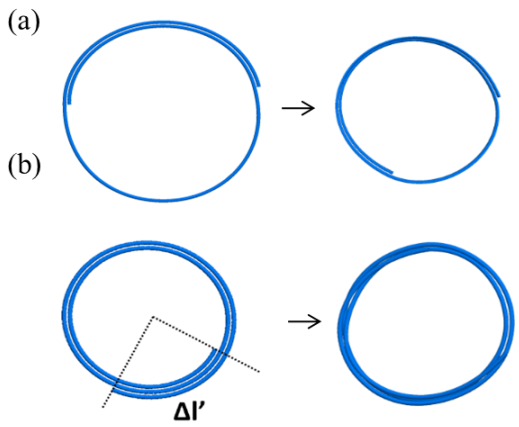

Figure 3-2 MDEM simulations of ring windings assembled from a single (10,10) CNT with L = 340 nm, showing initial and final configurations. The final radii are (a) 38 nm and (b) 23 nm.

For a broader view, there exists an analytical model able to account for the situations in which the SWCNT winds around itself more than once. This model is developed under the following assumptions: (i) the winding configuration containing n turns is assumed to be a perfect circle with no thickness (a characteristic radius R with this configuration is assumed, which only depends on L and the total overlap distance Δl), (ii) the elastic regime still holds and the turns are in a pure bending state, and (iii) the nearest-neighbor distance between the overlapping turns correspond to the 1.76 nm equilibrium intertube spacing between (10,10) SWCNTs. [78]

The total energy of the ring system with n turns consists of vdW and bending components:

$$U(L, \Delta l') = U_{vdw}(L, \Delta l') + U_b(L, \Delta l'). \quad (9)$$

Keeping in mind of the elastic continuum, bending strain energy can be written as:

$$U_b = 8\pi^2 B \frac{L}{(L-\Delta l')^2}, \tag{10}$$

where $B = 2.23\times10^3 \text{eV}\cdot\text{nm}$ is the bending stiffness of a (10,10) SWCNT. [79] The vdW energy can be written as a function of local overlap length:

$$U_{vdW} = \zeta_{n+1}\ \Delta l' + \zeta_n \cdot (2\pi R - \ \Delta l'), \tag{11}$$

where coefficients ζ_n and ζ_{n+1} are the vdW adhesive energy per unit length for the ring wall containing n and n+1 CNT cross-sections, respectively. To better capture the behavior of multi-winding rings, it is more convenient to express the total energy in global overlap length as $U_{vdW}(\Delta l,\ L)$. Based on the geometric relations $2n\pi R + \Delta l' = L$ and $\Delta l - \Delta l' = 2(n-1)\pi R$, the following variable change is applied:

$$\Delta l' = n\Delta l - (n-1)L. \tag{12}$$

In order to evaluate ζ_n, a model for the wall morphology is needed. In this respect, there is consideration of the two possible arrangements depicted in Figure 3-3a. In the 2D model, the SWCNT cross sections are located on a line, as in the planar Archimedean spiral of Figure 3-2b, left. In the 3D model they are instead "glued" together into a close-packed triangular lattice, inspired from the experimental observation of SWCNT ropes. [80] In the Δl variable, it follows that $U_{vdW}(\Delta l,\ L)$ becomes a piecewise function. Table 3-1 lists the vdW coefficients for both 2D and 3D models, as functions of the amount of overlap, as well as the number of turns.

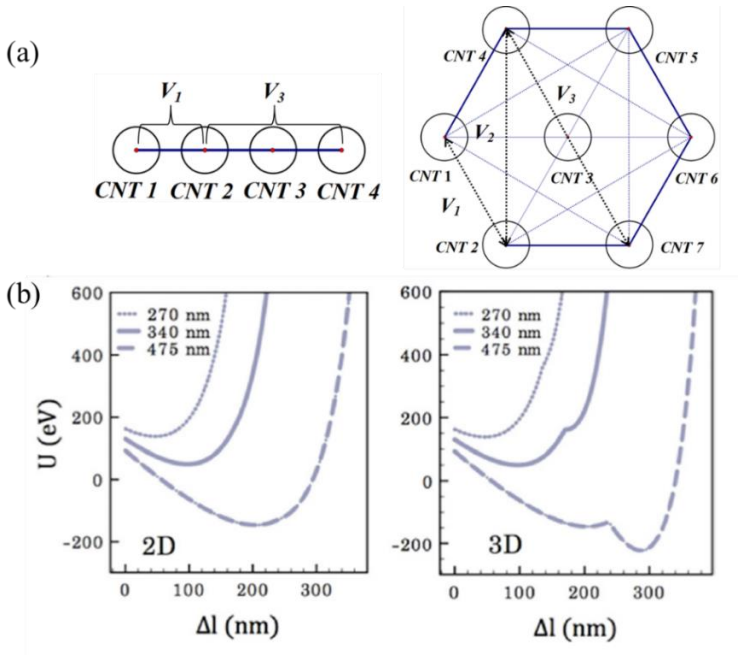

Figure 3-3 SWCNT cross-sections showing two models for the ring wall, a 2D (left) and 3D (right) model. V_1, V_2 and V_3 are vdW adhesion energy density between first, second and third nearest neighbors. (b) Analytical model predictions of the total potential energy as a function of the overlap length for the 2D (left) and 3D (right) wall models.

Table 3-1 vdW adhesion energy densities as a function of overlap Δl and number of turns n. For each n, the Δl range can be identified with Eq. 12. Coefficients $V_1 = 2.114$ eV/nm, $V_2 = 0.018$ eV/nm, and $V_3 = 0.007$ eV/nm represent the vdW interaction between 1 and 2, 2 and 4, and 2 and 5, respectively, in Figure 3-2a, right. They were obtained by direct integration of the microscopic vdW interactions (details obtained from Ref. [66]).

Ring Windings	Range of Overlap Length	vdW Energy Density 3D Arrangement (unit: eV/nm)	vdW Energy Density 2D Arrangement (unit: eV/nm)
1	$\Delta l < 1/2L$	$\zeta_2 = V_1 = -2.11$	$\zeta_2 = V_1 = -2.11$
2	$1/2L < \Delta l < 2/3L$	$\zeta_3 = 3V_1 = -6.34$	$\zeta_3 = 2V_1 + V_3 = -4.24$
3	$2/3L < \Delta l < 3/4L$	$\zeta_4 = 5V_1 + V_2 = -10.59$	$\zeta_4 = 3V_1 + 2V_3 = -6.36$
4	$3/4L < \Delta l < 4/5L$	$\zeta_5 = 7V_1 + 2V_2 + V_3 = -14.84$	$\zeta_5 = 4V_1 + 3V_3 = -8.48$
5	$4/5L < \Delta l < 5/6L$	$\zeta_6 = 9V_1 + 4V_2 + 2V_3 = -19.11$	$\zeta_6 = 5V_1 + 4V_3 = -10.6$
6	$5/6L < \Delta l < 6/7L$	$\zeta_7 = 12V_1 + 6V_2 + 3V_3 = -25.50$	$\zeta_7 = 6V_1 + 5V_3 = -12.72$

By comparing the last two columns of Table 3-1, it is obvious that in the 3D arrangement the ring wall has lower vdW energy states. The corresponding impact on the winding behavior is shown as U vs. Δl plots for three SWCNT lengths in Figure 3-3b. Note that U is measured with respect to the straight SWCNT state, where both U_b and U_{vdw} are vanishing. L is an important parameter as longer SWCNTs are associated with more stable winding. For all considered L, the 2D arrangement supports only one energy minimum state associated with n = 1. Meanwhile, the 3D arrangement offers two local minima for L of 340 nm and 475 nm, corresponding to n = 1 and n = 2, respectively. Interestingly, the n = 2 winding case predicted by MDEM simulations (Figure 3-2b) is only a local minimum at L = 340 nm, but becomes the global minimum at L = 475 nm. Apparently, 2D arrangement should be discarded, as it yields structures that are more than 30% higher in energy than the 3D ones and does not reflect the true stable configuration.

The agreement between MDEM simulations and the analytical model reveals longer SWCNTs tend to form multi-winding ring structure. It is noted that the analytical model yields continuous energy with no “cascading” or no more than two energy minima. A key observation is that larger L favors windings with multiple turns: As L increases, only the second minimum remains as the first energy minimum quickly becomes unstable. The surviving minimum shifts to the right, towards larger overlap, while its energy decreases significantly. In Figure 3-4b, this behavior is exemplified for L = 680 nm. Now,

there is only one energy minimum at $\Delta l = 473$ nm corresponding to an $n = 3$ winding. The trend of lowering the total energy with L makes SWCNT winding excellent for mechanical energy storage.

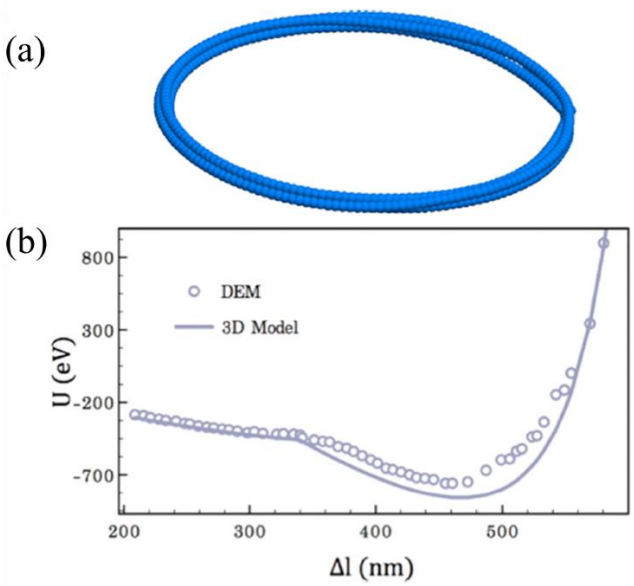

Figure 3-4 (a) A stable DEM simulated $n = 3$ winding with $R = 35$ nm. (b) Potential energy vs. overlap length for $L = 680$ nm showing both DEM (circles) and analytical (line) models.

In the MDEM realization of the SWCNT winding, a complete analysis of deformation involves other modes, such as twisting in Figure 3-5a. Nevertheless, these energy components are negligible compared to the bending mode. For example, the winding configuration shown in Figure 3-4a stores 571.5 eV total strain energy, in which bending energy covers 97.4%. Similarly, in another MDEM simulation of an $n = 8$ winding, twisting energy represents only 1.2% from the total strain energy. As shown in Figure 3-5b, other types of imperfections encountered in the simulations were local SWCNT separations other than the equilibrium distance of 1.76 nm, which lead to

lowering of the vdW energy. Despite these additional effects, the total energy computed in MDEM simulations (circles) follows closely the analytical predictions (line) with a deviation less than 10% (Figure 3-4b). Hence, the features captured by the analytical model are dominating the energetics.

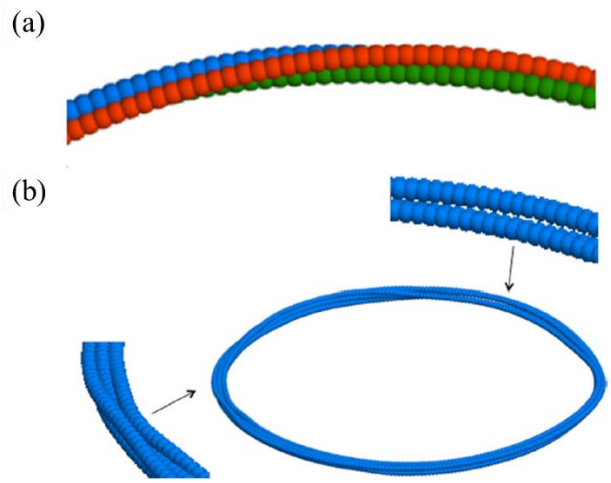

Figure 3-5 Details of DEM simulations showing: (a) twisting in the wall of the n = 3 winding of Figure 3-4a and b; (b) local separation of SWCNT portions in the shown n = 5 winding.

The validity of the analytical modeling predictions can be generalized to larger windings made of ultra-long SWCNTs. For convenience, the modeling is restricted to windings whose n satisfy the relation:

$$n = 3N^2 - 3N + 1, \tag{13}$$

where N is a positive integer. This relation ensures the ring wall always belongs to the family of ideal crystalline hexagonal arrangements. For example, N = 2 gives the arrangement depicted in Figure 3-3a, right. The advantage of this choice is to avoid the more complex calculations for the various arrangements of wall cross sections. The vdW

adhesion energy density is easily evaluated (details available in Appendix A), as:

$$\zeta_n = 3[(3N^2 - 5N + 2)V_1 + (3N^2 - 7N + 4)V_2 + (3N^2 - 7N + 3)V_3], \tag{14}$$

$$\zeta_{n+1} = 3\left[\left(3N^2 - 5N + \frac{8}{3}\right)V_1 + \left(3N^2 - 7N + \frac{13}{3}\right)V_2 + \left(3N^2 - 7N + \frac{11}{3}\right)V_3\right], \tag{15}$$

from which the total potential energy becomes available. Setting the derivative of U to zero yields the overlap corresponding to the minimum energy:

$$\Delta l = L - \sqrt[3]{\frac{4\pi^2}{[(n+1)\zeta_n - n\zeta_{n+1}]}BL}. \tag{16}$$

The above equation can be useful to estimate the ring formation condition of (10,10) SWCNT. By setting Δl = 0, the critical length needed to form a winding with n = 1 is found to be 204.1 nm, compared to 180 nm determined by MDEM simulations. An ultra-long CNT (~2 mm in length) is predicted to fold into a winding with 2611 turns and radius of 2 μm. The potential of such windings for energy storage is remarkable. The energy density stored in such a winding reaches ~85 Wh/kg. This value is two orders of magnitude larger than the mechanical energy that could be stored in conventional steel springs and comparable to the electrochemical energy density in currently used Li-ion batteries. [81-83]

Although so far only (10,10) SWCNTs are considered, the model predicts that

long SWCNTs of other chiralities will also form stable ring winding. For example, a (15,4) SWCNT has similar diameter and linear elastic attributes as the (10,10) SWCNT [84], despite the difference in electronic type (semiconducting vs. metallic) that gives a 23.7% increase in vdW adhesion. [85] As a consequence, it leads to a greater tendency for winding formation. For example, to form a n = 2611 winding, the model predicts that a (15,4) SWCNT length of 1.94 mm suffices with a stored energy density of 105 Wh/kg. Once the harvesting method is further developed, CNT rings could be widely used in braking systems of vehicles [82] and micro-electro-mechanical systems (MEMS) where the severe environmental factors [86] or dimensions of energy supplies play an important role.

3.3. Bending of Crystalline SWCNT Ropes

Made by a bundle of individual tubes, CNT ropes with high mechanical strength and low densities are viewed as promising structural materials. Due to the vdW adhesion, SWCNTs within the rope spontaneously assembled into a hexagonal close-packed configuration. Under loading conditions, such as non-uniform tension, twisting, and bending, the relative motion of each SWCNT within the rope can lead to a shearing that is only significant for shorter and thicker ropes. [87] The self-assembled aggregates often involve with CNT ropes. To further generalize the analytical model developed in Eq. 9 - Eq. 11, bending stiffness of the ropes must be first accessed with the consideration of

intertube sliding.

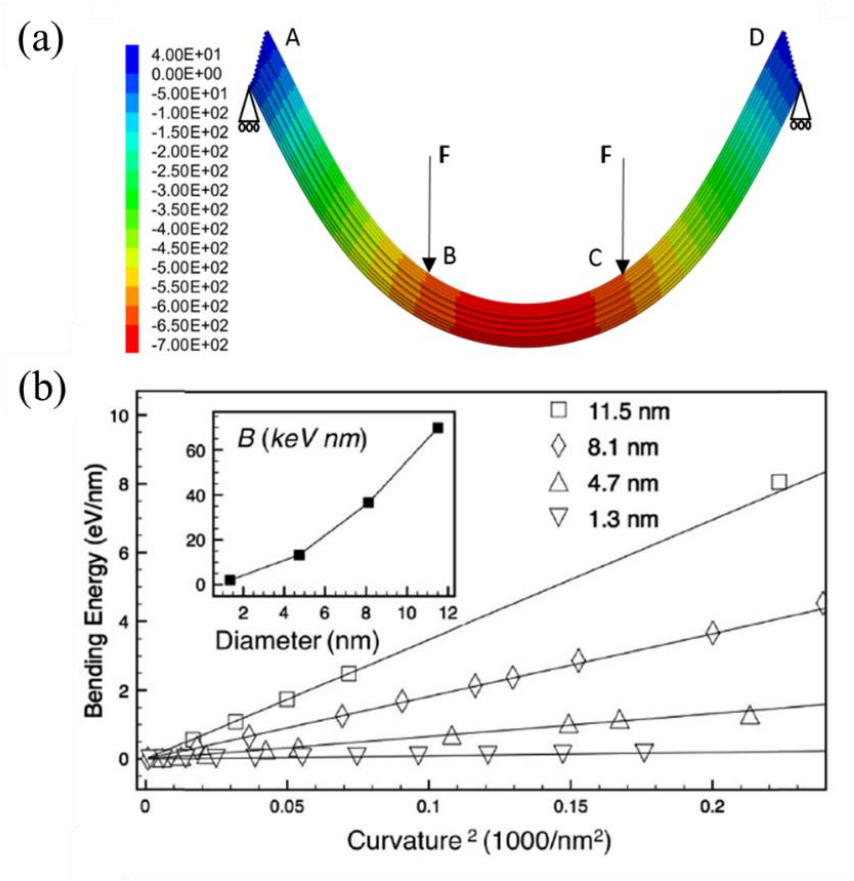

Figure 3-6 (a) Set-up for four-point bending simulations conducted with MDEM. The down arrows indicate the location of the applied forces. The displacement in the scale bar is in Å. (b) Bending energy versus curvature squared for SWCNT ropes of various diameters. The inset shows the variation of the bending modulus with rope diameter.

One straight forward approach is four-point bending test, also known as flexural test. Figure 3-6a demonstrates the basic setup and key features of our model in four-point bending simulations conducted on crystalline ropes containing 80 nm in length SWCNT. Two-end roller support was imposed by fixing the y coordinates of selected elements located at the two ends (A and D). The other degrees of freedom of these elements are

free so that the constituent SWCNTs are allowed to slide against each other. The load is applied on the elements located at the cross sections B and C, which are symmetrically spaced around the loading span with a distance of L = 26 nm. The magnitude of the applied load ranges from 0.032 nN to 0.48 nN. Bending process is monitored by measuring the difference in deflection, δ, between the elements located at the symmetry center and those at B and C, and the bending energy stored in the parallel contacts located in the volume between B and C. In the simulation, only the pure bending section BC is analyzed. The maximum deflection is expected to be in the center of the rope. From the classic Euler-Bernoulli beam theory, the bending strain energy is written as:

$$U_b = \frac{1}{2}\int_0^L B\left(v''(x)\right)^2 dx = \frac{1}{2}\int_0^L \frac{B}{R^2(x)} dx, \tag{17}$$

where R is the radius of curvature as a function of x and B is the bending stiffness of the rope. It can be shown in a four-point flexural test that the curvature of section BC is constant due to constant bending moment. By geometry, R can be solved numerically from the following relationship:

$$R\left(1 - \cos\left(\frac{L}{2R}\right)\right) - \delta = 0. \tag{18}$$

Given the dimension of a CNT bundle, B and R are constants. Bending energy density (i.e. energy per unit length) can then be simplified from Eq. 17:

$$\frac{U_b}{L} = \frac{B}{2R^2}. \quad (19)$$

Table 3-2 Bending stiffness B as a function of the number of SWCNTs in the rope n. Results are obtained from four-point bending simulations conducted with MDEM.

n	B (keV nm)	B/B_0
1	1.97	1
7	13.3	6.75
19	36.6	18.55
37	69.8	35.38

Figure 3-6b demonstrates linear variations of the bending energy vs. the curvature squared. The bending moduli extracted from these simulations are presented in the inset to Figure 3-6b and in Table 3-2. As shown in the last column of Table 3-2, the bending of a rope containing n SWCNTs can be described by an anisotropic beam with $B = nB_0$, where B_0 is the bending stiffness of an individual SWCNT. The sliding of the tubes against one another, [87] correctly captured by our anisotropic vdW model, represents a well-known obstruction towards the use of SWCNTs as building blocks in composite materials and structures. This behavior contrasts with what would be obtained by employing the usual isotropic treatment of the vdW interactions between coarse-grained elements. The isotropic treatment leads to staggering-induced corrugation, [65, 66] an artifact that prevents sliding of individual SWCNTs within the bent rope.

3.4. Self-assembled Rings and Rackets from SWCNT Ropes

With the knowledge of bending stiffness of SWCNT rope, the formation of self-assembled aggregates is ready to be revisited. In our collaborative experiments, [88]

self-folded ropes into rings and rackets are reported in dried film cast from dilute CNT suspension. The AFM images shown in Figure 3-7 were obtained by casting droplets of dilute SWCNT suspension on smooth silicon substrates and repeatedly wicking away excess isopropanol solution. (Detailed preparation and characterization procedures are available in Appendix B and [59].) Experimental evidence now offers direct validation of MDEM modeling.

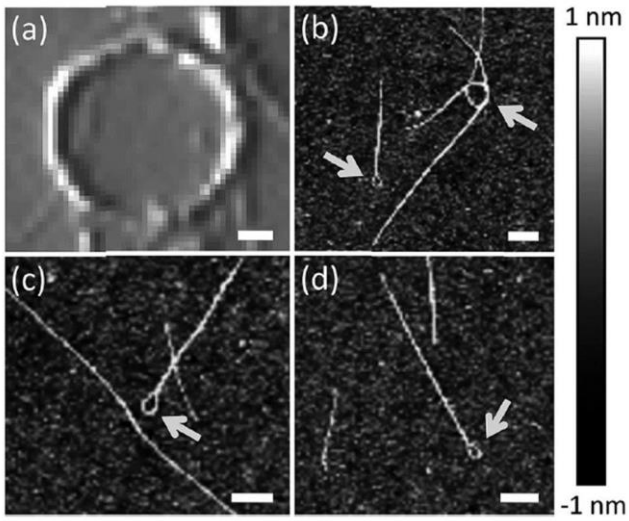

Figure 3-7 (a) A ring (diameter = 250 nm, height = 15 nm) spontaneously formed in a dried suspension of SWCNT ropes (scale bar = 50 nm). (b)–(d) Knots and rackets formed during the deposition of length-enriched suspensions of individual SWCNTs (scale bar = 100 nm). The height legend for panels (b)–(d) is shown at the right. All shown structures are located on silicon wafer substrates. (Experimental preparation procedures are available in Appendix B)[3]

In Figure 3-8a, we consider the direct winding of an entangled rope. Starting from the zero-energy straight configuration, the rope was gradually bent so that the two ends could be brought together into vdW contact (Figure 3-8a, left). After achieving some

[3] Experimental sample preparation and measurement in this chapter were performed by collaborator Prof. Erik Hobbie from North Dakota State University, Fargo, ND

overlap, the rope was relaxed and the two ends were stirred one past another. Stirring was necessary as the rope–rope sliding is a rather slow process. As shown in Figure 3-8c, stirring lowers of the total energy. The configuration shown in the right panel of Figure 3-8a corresponds to the lowest energy state. A SWCNT rope, such as the one shown in Figure 3-8a, can indeed be stabilized by vdW adhesion. The sliding of the constituent SWCNTs visible in Figure 3-8a ensures that bending of the rope remains a soft mode. MDEM simulations beyond this state suggest that a further increase in overlap increases the total potential energy.

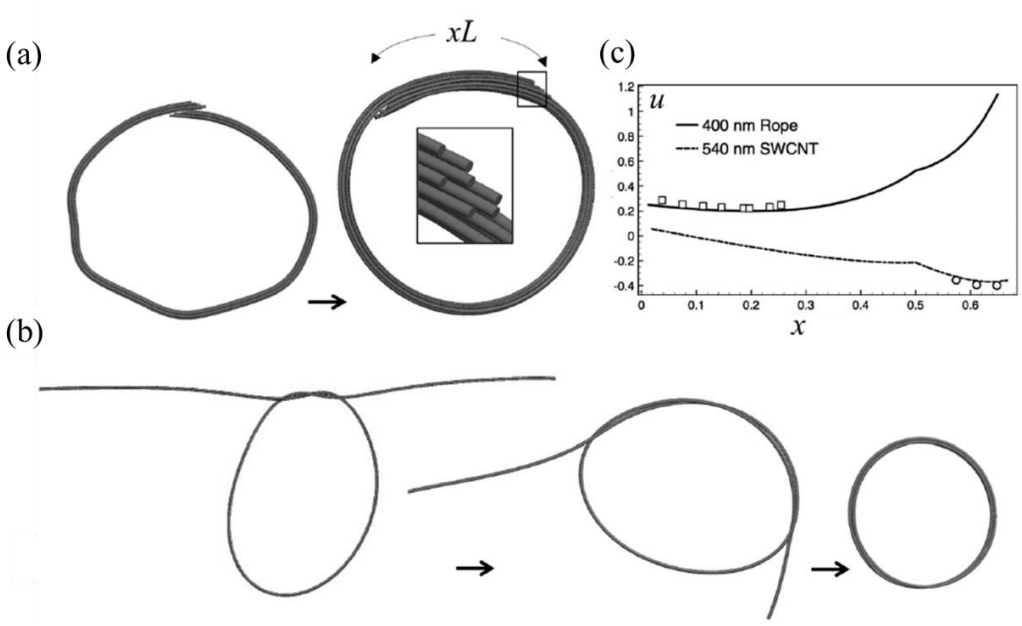

Figure 3-8 (a) Ring with one turn formed by a rope containing 7 SWCNTs each 400 nm in length. The inset illustrates the sliding of SWCNT rope at the free end. The final ring diameter is 104 nm. The overlap length *xL* is also shown. (b) A ring winding with three turns formed by a 540 nm long SWCNT. The final ring diameter is 64 nm. (c) Normalized total potential energy versus overlap for the two simulated ring morphologies, where the curves are predictions based on Eq. 20 and Table 3-3. Parameter z was set to -6.426 eV·nm^{-1} for the rope–rope and to -2.114 eV nm^{-1} for the tube–tube interactions.[78] In deriving z for rope–rope, we assumed a hexagonal close-packed rope structure and considered vdW tube–tube interactions up to the 3rd neighbor.

The dynamic ring winding formation is depicted in Figure 3-8b, starting from a SWCNT initially entangled knot. Under relaxation, the radius of the central loop is increasing while the vdW forces and aligning moments are helping to attach the two free ends on the knot's central loop. The attachment of the two ends is followed by a sliding process, which results in a reduction of the ring radius. Thus, our MDEM simulations demonstrate that knots with free ends (Figure 3-8b), are prone to form a ring winding. It is likely that the knot observed in experiment is stabilized by its contact with the other nanotube.

The analytical model discussed in Chapter 3.2 comprising bending and adhesion energy components can be generalized to explain the final equilibrium ring shapes. Let ζ be the vdW adhesion energy per length between two ropes (Figure 3-8a) or two SWCNTs (Figure 3-8b) and let x be the total overlap length, normalized by L. The dimensionless total potential energy, in units of $|\zeta|L$, has the following expression:

$$u = -\alpha - \beta x + \frac{2\pi^2 b}{(1-x)^2}. \tag{20}$$

The linear term represents the vdW adhesion energy normalized by $|\zeta|L$. In ring windings with multiple turns, this term is a piecewise function with the coefficients α and β given in Table 3-3. These coefficients were calculated analytically under the assumption that the nearest-neighbor distance between the overlapping turns corresponds to the 1.76 nm equilibrium intertube spacing between (10,10) SWCNTs and that the parallel ropes

ends do not coalesce into one to further lower the vdW energy. The last term represents the bending strain energy, where $b = \frac{B}{L^2|\zeta|}$. Depending on the number of constituent SWCNTs inside the rope, B takes the values indicated in Table 3-2.

Table 3-3 Values for the dimensionless coefficients α and β describing the vdW adhesion. x is the normalized total overlap length and n is the number of SWCNTs in the rope. Only rings with up to two turns are considered here.

x	**n = 1**		**n = 7**	
	α	β	α	β
(0, 1/2)	0	1	0	1
(1/2, 2/3)	-1.00474	3.009479	-1	3

Total potential energies predicted by Eq. 20 are plotted in Figure 3-8c. The analytical approach shows that the 400 nm rope and the 540 nm SWCNT have only one minima corresponding to a single and a multiple (three) turn ring, respectively. The equilibrium MDEM morphologies are located very close to the minima of the analytical curves. For the experimental longer and thicker rope, this analytical model also yields satisfactory prediction. For a rope with diameter 13.5 nm and length 750 nm, the stabilized configuration is predicted to be at radius of 116 nm with an overlap length of 20 nm. This is in good agreement with the experimental results shown in Figure 3-7a.

Another self-assembled agglomerate has the shape of tennis racket. The SWCNT rope is bent over onto itself, such that the inner sides of the two ends became parallel in vdW contact. Note that in the SWCNT case, it is not necessary that this entanglement be symmetric as the two ends are sliding past one another. Next, relaxation procedures were

conducted, which produced the racket structures shown in Figure 3-9. The aggregate thus obtained closely resemble the ones indicated in the experimental images of Figure 3-7 down to the scale of the racket head and the twisted structure of the handle.

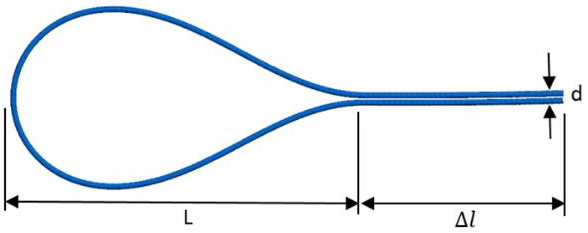

Figure 3-9 A 400 nm CNT self-assembled into racket shaped simulated by MDEM.

In Figure 3-9, the racket morphology is partitioned into the racket head (L) and handle (Δl), which contain strain energy and vdW potential energy, respectively. The stable configuration is governed by the balance between these two energies. Due to insufficient contact length Δl, short CNTs are not believed to form the racket assembly. Buehler et al. [53, 76] simulated this CNT folding phenomena through the mesoscopic BS model. They predicted that in vacuum, the critical length has positive correlation to $\frac{B}{\zeta}$, where B is the bending stiffness and ζ is the intertubular vdW potential per unit length.

Zhou and Huang [89] provided an approximate analytical model to study the total energy as a function of L and Δl, which is a key criterion to determine the stability of this configuration. Their Euler-Bernoulli beam model is based on solving the governing equation $EI\frac{d^4w}{dx^4}$ =0 with the boundary conditions: $w = \frac{d}{2}, \theta = 0$ at $x = 0$ and $w = 0, \theta = -\frac{\pi}{2}$ at L. In spite of the exact solution that was later found, [90] the complexity of

the integral prohibits the numerical calculation and thus Eq. 21 still holds for sake of simplicity:

$$U = EI\left(\frac{3d^2}{L^3} + \frac{\pi^2}{L} - \frac{3\pi d}{L^2}\right) - \zeta \Delta l. \tag{21}$$

Previous simulations [52, 53], although revealed to be accurate, lacked the connection to experimental conditions, since dealing with ultra-long CNT in units of microns remains challenging. Now, MDEM simulations of long CNTs (~1 micron) enables such realistic comparison. An analytical model must be solved to guide these simulations. To generalize Eq. 21, a dimensionless form is derived:

$$u = \beta\left\{\frac{3\alpha^2}{(0.5-x)^3} - \frac{\pi^2}{0.5-x} + \frac{3\pi\alpha}{(0.5-x)^2}\right\} - x, \tag{22}$$

based on the non-dimensional terms listed below:

Dimensionless total energy: $u = -U/L\zeta$;
Dimensionless bending stiffness: $\beta = EI/L^2\zeta$;
Dimensionless spacing: $\alpha = d/L$;
Dimensionless handle length: $x = \Delta l/L$.

Neglecting higher order terms, the competition between vdW adhesion and bending leads to a simplified equation:

$$u = -x + \frac{\pi^2 b}{x-0.5}. \tag{23}$$

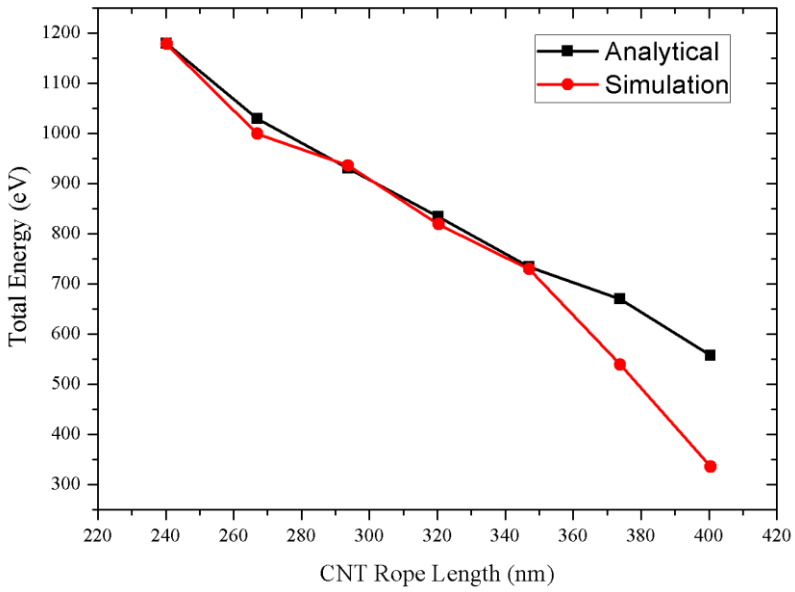

Figure 3-10 Total energy of self-assembled racket computed from both analytical model (Eq. 22) and MDEM simulations.

Based on Eq. 23, total energy can be evaluated for CNT ropes with different lengths. For shorter CNT ropes, MDEM simulations are in agreement with analytical model (Eq. 23), while for ropes longer than 350 nm, the discrepancy can be as large as 50%. However, the dimension of the structure, namely length of the handle part, is still well predicted. As can be seen from Figure 3-11c, the simulation data is located very close to the energy minima of the analytical curves. The lower energies obtained in computation can be explained by the new adhesion and elastic effects accounted for in the DEM simulations. Figure 3-11a shows that under vdW forces, the two ends of the rope containing 7 SWCNTs spontaneously mix their structure to form a single rope. Note that the end of the handle is still a new surface formed by sliding effect, whose energy penalty is about 10% of the total potential energy. In rackets formed by SWCNTs, Figure

3-11b, the two ends form a helical handle. For the morphology shown in the top of Figure 3-11b, our analysis of the strain energy indicates that the onset of twisting reduces the total elastic strain energy by approximately 11% while affecting the curvature and dimensions of the head. We also note that the racket head dimensions are not changing significantly with the SWCNT length.

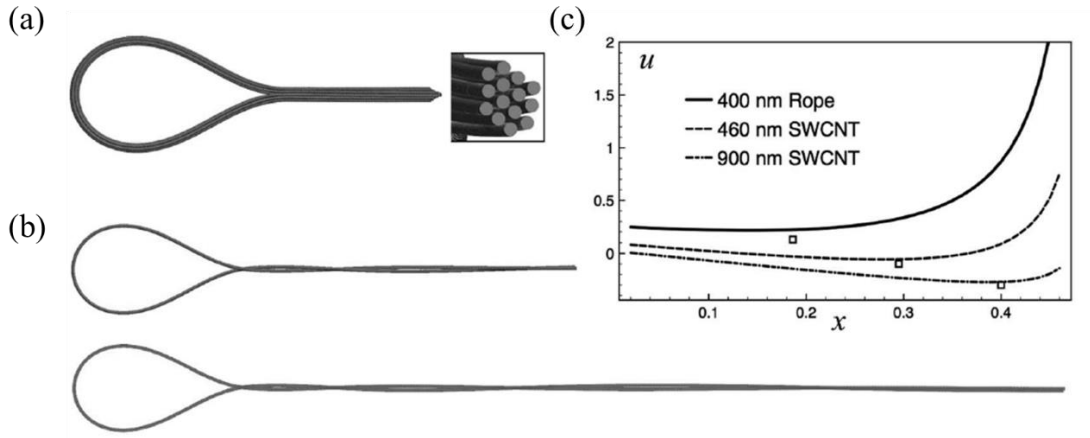

Figure 3-11 Racket morphology formed by (a) a 400 nm long rope containing SWCNT and (b) 460 nm (upper) and 900 nm (lower) SWCNTs. The lengths (widths) of the racket heads are 125 (76) nm, 77 (39) nm, and 70 (36) nm, respectively. (c) Total potential energy versus overlap the three simulated racket morphologies. The lines are predictions based on Eq. 23 and Table 3-3.

The MDEM simulated agglomerates have established the stability and can be further connected with experiments. An important feature of both ring and racket configurations is the weak dependence of the aggregate dimensions on *n*, number of tubes inside the rope. This dependence can be extracted by knowing the minimal length to yield stable agglomerates, [66, 89] which scales with $\left(\frac{B}{\zeta}\right)^{\frac{1}{2}}$. Accepting that $B \propto n^{\frac{1}{2}}$ and $\zeta \propto n^{\frac{1}{2}}$, it follows that the radius of curvature scales as $n^{\frac{1}{4}}$.

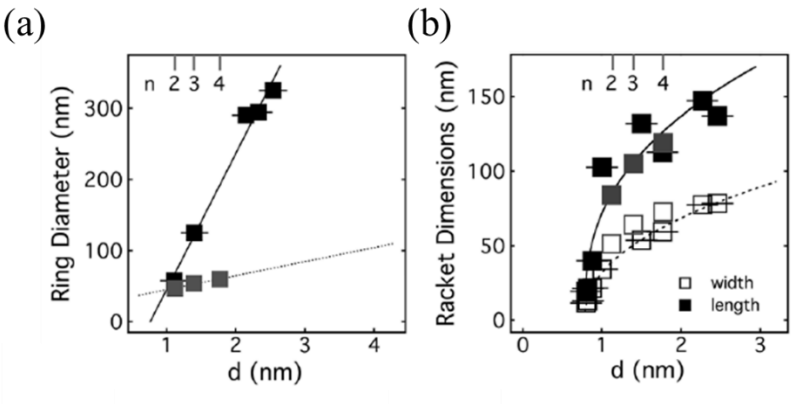

Figure 3-12 (a) Measured and computed ring diameter as a function of rope diameter with a linear fit. (b) Measured and computed racket head dimensions as a function of rope diameter with fits, as described in the text. Black markers are measured and gray (full and empty) markers are predicted by the models of Eq. 20 and Eq. 23. The number of SWCNTs in the rope *n* is also shown.

The scaling derived above indicates that there should be an increase in the sizes of the rings and rackets' heads that is most noticeable in the very small rope diameter range. To test it, we have performed collaborative experimentation to create and analyze aggregates of SWCNT ropes (experimental procedures are included in Appendix B). The analysis of the obtained aggregates is summarized in Figure 3-12. One can see that indeed the agglomerate dimensions are in positive relation with the rope diameter. The dependence of ring size on rope diameter is essentially linear and extrapolates to zero close to what corresponds to the mean minimum nanotube diameter in the ensemble (around 0.7-0.8 nm). The racket dimensions, in contrast, demonstrate percolative behavior, scaling roughly as $(d - d_c)^{\eta}$ with $\eta \cong 0.4$ for both the length and width of the racket heads. The measured aspect ratio of the rackets is always close to 2, independent of bundle diameter. Interestingly, the threshold d_c = 0.78 nm is also close to

the minimum diameter of an individual SWCNT. The region close to d_c should be viewed as a step corresponding to the smallest equilibrium racket size for an individual SWCNT.

As an important fact, when scrutinizing the experimental data, one needs to limit the analysis to agglomerates that have minimal contact with other aggregates and bundles. Otherwise, the measured trends shown in Figure 3-12 are obscured, or even reversed, suggesting that entanglements with other aggregates can act to stabilize rings and rackets at much larger dimensions than would occur in isolation. This makes sense physically, since external perturbations arising from other structures will compete with those identified in the model and simulations.

Judging from the comparison with theory, we conjecture that most of the morphologies characterized in Figure 3-12 are not far from the optimum balance between the elastic bending and rope–rope attraction. In Figure 3-12a, the measured diameter of the ring formed by a single SWCNT agrees with the predictions given by the Eq. 20 and MDEM simulations. The rings formed by the ~2.5 nm ropes appear, however, to be larger than what is predicted by the model, suggesting that these structures are not yet fully relaxed. Nevertheless, the predicted racket dimensions have similar magnitudes and increasing trends as the data in Figure 3-12b. Insights from the MDEM simulations help clarify these differences. While in the simulations SWCNT–SWCNT sliding occurs with ease, the rope-rope vdW sliding is rather a slower process. While the ring dimension is

directly impacted by the vdW sliding, the racket head dimensions are less sensitive to the degree of overlap achieved in the handle part.

3.5. Concluding Remarks

The agreement between experiment and theory supports the conclusion that the formation and stability of rings and rackets is the result of the interplay between the mesoscopic mechanics and adhesion attributes of SWCNTs. As the lengths of SWCNTs are ever increasing, winding them into the stable rings represents a natural way to store and manipulate them. Windings made out of cm-long SWCNTs store high energy densities, making them promising architectures for energy storage. This stored energy increases with the SWCNT length and could potentially be used to power nano- and micro-electromechanical systems.

On the other hand, it is expected that the racket morphologies could be exploited for quantifying the elastic and adhesion attributes of other fibrous materials. The recently developed DEM mesoscale simulation approach is both analytically and experimentally validated and should be also applicable to agglomerates formed by other fibrous nanomaterials.

Chapter 4 Nanomechanics of Twisted CNT Ropes[4]

4.1. Introduction

Weaving of braided and laid ropes has been well known as an important craft since prehistoric times. [91] The mechanical performance of a rope highly relies on not only the strength of the materials but also its twisted geometry during the spinning manufacturing process. [92-94] Modern technology has proposed a large variety of new synthetic materials for ultra-strong rope fabrication. More recently, besides the industrially produced nylon and polyester, carbon nanotubes (CNTs) have become a competitive candidate for yarn manufacturing (Figure 4-1). [95] The extraordinary torsional stiffness of CNTs leads to wide potential applications, including structural support, artificial muscle [96] and electric motor [97].

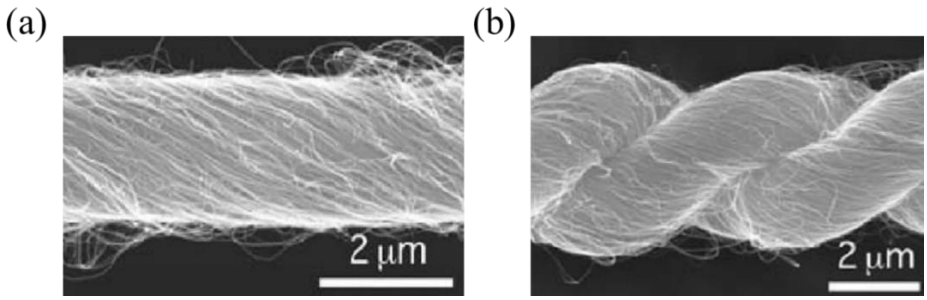

Figure 4-1 Carbon nanotube yarns manufactured through spinning process.

To manufacture advanced rope structures with such outstanding nanofibers [98], it

[4] Portions of this chapter have been published in *Langmuir* (DOI: 10.1021/acs.langmuir.5b03208, 2015)

is crucial to understand the relationship among geometry, internal packing, and the individual nanofiber mechanics. The ability to quantify total energy as a function of twist is an important step in this direction. All-atom simulations uncovered remarkable insights into the torsional mechanics of CNT systems. [99-101] Unfortunately, these methods are impractical for simulating twisted CNT assemblies approaching realistic dimensions.

Torsional deformation of cohesive fibers per se also has complex nature. Due to the limited sliding friction, [78, 102, 103] there is a poor load transfer between CNTs. When a crystalline close-packed aligned CNT rope is twisted, it is expected that the nanofiber constituents will acquire a variety of deformations, including geometric and physical twists. (Physical twist is the relative rotation of elements along the axis of the rope; geometric twist is bending in the direction of the binormal vector.) In terms of BS modeling, the coarse graining of a group of atoms into a point mass cannot be trained to describe the torsional deformations of the individual CNTs. In addition, theories and simulations of defects in twisted ropes [104-106] evidenced the relationship between packing defects and rope twist. The development of such defects cannot be described with large-diameter bead-and-spring models of the CNTs. These models introduce interfacial corrugated interactions, which prohibit smooth sliding [65, 107] and the CNTs' relaxation into the lowest-energy state.

Now, with efficient mesoscopic modeling tool at hand, such studies become

tangible. In this chapter, MDEM is applied to access the deformation regime needed to investigate packing in twisted CNT ropes. We achieve packing rearrangement conditions, where the vdW adhesion between CNTs decreases and even vanishes, and rope geometries dictated by the CNT mechanics. By contrast, previous simulations focused on the load-transfer regime and considered twisted ropes comprising only a few number of CNTs. [101, 107, 108]

4.2. Description of Highly Twisted CNT Rope Morphologies

As described in Chapter 2, the introduction of twist model enables transferring torsional moments through CNTs. The MDEM implementation of twist proceed in two stages described as the following. First, torsional moments $\boldsymbol{M}$ along the rope axis are applied in incremental steps when gripping distinct elements located at the two ends. At each incremental step, all elements are evolved in time by holding only the grip elements under the corresponding twisting moment to prevent the CNTs from twisting back. With this protocol, we relax the structure and avoid high distortions localized at the grips. The constituent CNTs will form helices so the parallel-bonds representing the helical state will store a superposition of bending and twist due to both physical and geometric twist experienced by individual CNTs. Second, at the end of the loading process the applied constraints are only maintained and the system is evolved under a longer time interval. The applied loading rates and final relaxation time were decided after making sure that

convergence was achieved. In both stages, the grip elements are allowed to change their axial positions.

A CNT rope responds in various ways to twist moments, depending on their dimensions. Due to crystallinity and symmetry of CNT ropes, we consider length and radius (number of layers N in the hexagonal closed packed cross-section) as two independent geometrical parameters. The CNT ropes in the simulations vary from 40 nm to 163 nm in length L and 3.4 nm to 12.0 nm (N from 3 to 8) in radius R.

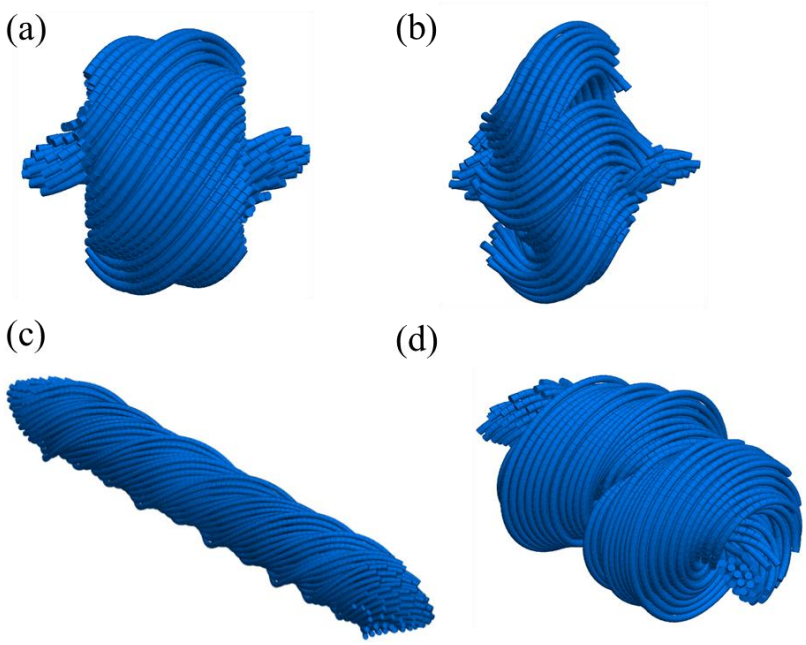

Figure 4-2 High twisted CNT morphologies: (a) bird cage structure formed by a short thick CNT rope (L = 40 nm, R = 10.8 nm and T = 52 nN·nm); (b) separation of bird cage due to over twist (T = 60 nN·nm); (c) spindle formed by long thin rope (L = 163 nm, R = 8.56 nm and T = 40 nm·nN); (d) a distorted rope due to over twist (T = 52 nN·nm).

Generally speaking, small torsional moments lead to fully reversible behaviors, while beyond the elastic limit, two modes, namely bird cage and spindles (Figure 4-2a

and 4-2c), occur for short thick and long thin rope respectively. Further increase the torsional moments T will introduce instability for the structure, separation and distortion (Figure 4-2b and 4-2d) are observed accordingly.

It is essential to point out these morphologies are generated by torsional moments associated with the free-end boundary conditions. Upon twisting, tubes on the rope surface first begin to bent, leaving cone shape exposure at two ends. The rope is then compressed in axial direction, while expanding in radial direction due to mass conservation and Poisson's effect. At certain point, the expansion leads to vacancies scattered inside the rope, known as topological defects. These defects break down the ideal hexagonal symmetry and are shown to be favorable in packing cohesive filaments in heavily twisted bundles, for their appearance lowers the energy. [106]

To quantify the topological defects inside the twisted ropes [104], it is convenient to introduce the concept of topological charge Q:

$$Q = \sum_n (6 - m)V(m), \tag{24}$$

where V counts for the number of tube whose coordination number is m. The mid cross-section (x=0 plane) is specified as a representative plane for monitoring the topological charges. Based on Isaac R.'s theory [104], topological charges, in most cases, appear around the center of the rope. For sake of computational simplicity, the effective calculating area is also chosen around the center to avoid the irregularity of highly

deformed boundary (Figure 4-3b). A CNT is considered to be internal if it has six nearest neighbors in the untwisted state. Due to hexagon or triangular arrangement, a nearest-neighbor element is situated within a $\sqrt{3}d$ distance, where d = 1.76 nm, which is the equilibrium interspacing of two parallel CNTs. When identifying the nearest neighbors, we approximate the distance between two helical CNTs with the smallest d between elements located on the two tubes. Due to symmetry considerations, the distinct elements at this location will tilt but not displace along the rope axis. The distance between neighbors does not always coincide with the separation between the corresponding elements in this cross section.

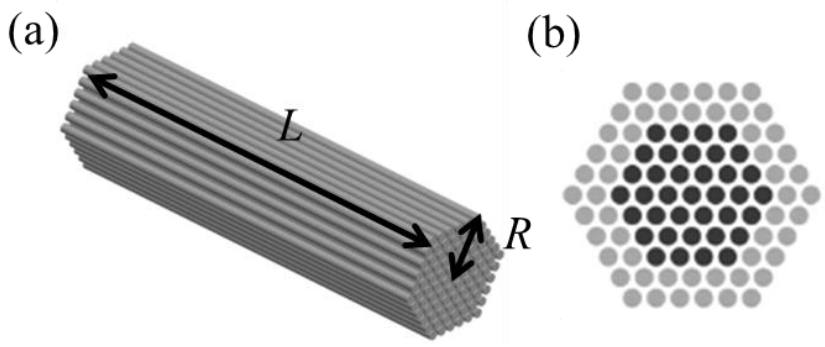

Figure 4-3 (a) A CNT bundle sample labeled with defined length L and radius R. (b) Mid cross-section (shaded tubes are selected as effective calculation area).

Eq. 24 implies that a topological charge can be both negative and positive, analogous to electric charges. In addition, similar to dislocations in crystalline materials, they are subjected to migrate and annihilate. However, their first appearance is often found around the rope center, where they start to accumulate and gradually form a hollow space. The hexagonal arrangement on the outer layers will evolve into a circular shape by

non-uniform expansion. Since twist of cohesive bundle is demonstrated as packing circles on a bundle equivalent cone surface, this non-uniformity is similar to packing charges on a spherical surface known as the famous Thomson Problem [109].

4.3. Energetics and Mechanics of Bird Cage Transformation

A spindle shape is the starting point of all twisted CNT ropes. Figure 4-4 describes the twisting of a rope with hexagonal packing, containing 91 CNTs, each with length L = 67.8 nm. The rope has an initial radius of 8.6 nm. The simulated morphologies, Figure 4-4a, display an increase in the twist angle β measured between the outermost CNTs and the rope axis. (The twist angle is lower for the internal CNTs.) Additionally, there is a dwindling down in profile to form a "spindle" morphology. This progression is possible due to the smooth vdW sliding and the employed free boundaries, which allow for the relaxation of the tensile strain accumulated in the individual CNTs. As the rope twists, the individual helical shape of the constituent CNTs with length L implies that the length of the bundle shortens with the radial distance from the bundle center. Associated with this process, there is an increase in bending energy (Figure 4-4b left).

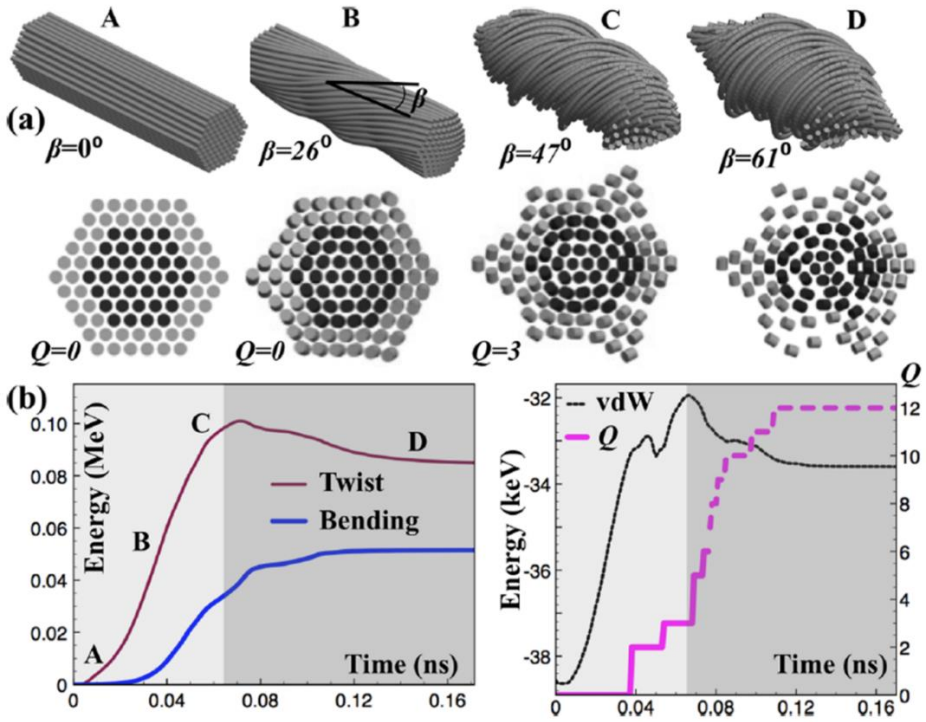

Figure 4-4 (a) Rope morphologies at different twist angles β. Cross sections and Q values are shown below. The CNT length is L = 67.8 nm. (b) Time evolution of the energy stored in the parallel and vdW contacts and of Q. The light-gray area is the loading stage (steady loading with 1.0 nm·nN/ps). The dark-gray area is the stabilization stage under T = 64 nm·nN. A–D mark the rope morphologies shown in (a).

If sliding is strictly prohibited by the applied boundary conditions and/or by the artificial corrugation effects, then the individual CNTs would experience elongation and therefore carry large tensile forces. In Figure 4-5, fixed and free boundary conditions are compared upon twisting. No radial expansion is seen in the fixed boundary condition and yet the strain energy is still increasing even though torsional loads are maintained in Phase II of Figure 4-5a. On the other hand, free boundary condition provides an energy relaxation mechanism that would involve hydrostatic pressures acquired in the interior of the rope and increased contact between CNTs. [107, 108] Under free boundary conditions

and sliding with little corrugation, the local CNT rearrangements interrupt the original 6-fold coordination.

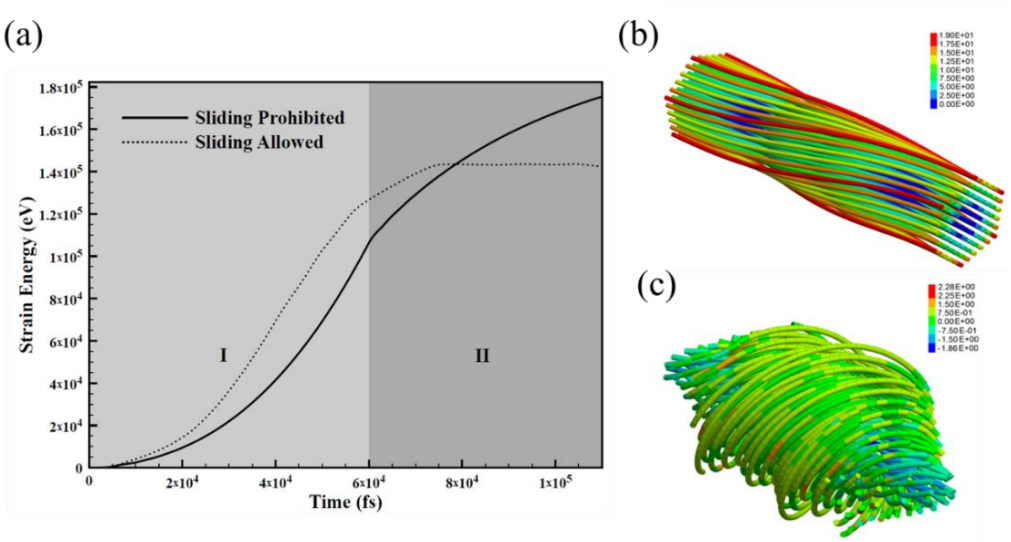

Figure 4-5 (a) Strain energies of twisted CNT rope with two boundary conditions. (L = 67.8 nm, R = 8.75 nm, T = 60 nm·nN and steady loading rate of 1.0 nm·nN/ps). Torsional loads are added in Phase I and maintained in Phase II (b) Local tensile force in twisted rope with sliding prohibited boundary condition (unit: eV/ Å) (c) Local tensile force in twisted rope with sliding allowed boundary condition (unit: eV/Å).

In Figure 4-4b right, structural rearrangements occurring in the core (dark-gray nanotubes) are visible in the changes in vdW energy and topological charge Q. When Q = 0, the rope is packed defect free. Initially, there is a steady increase in the vdW cohesion energy with twist due to changes in R, θ, and γ between the distinct elements in the vdW contact. When $Q \neq 0$, there is a change in packing that interrupts the decrease in cohesive energy. The positive values of Q indicate an excess in 5-fold defects. For example, the Q = 2 charge is due to two 5-fold defects. Negatively charged 7-fold packing defects are also encountered. The jump to Q = 3 is due to the emergence of a 7-fold and two 5-fold defects. Finally, when the applied twist is only maintained (the dark-gray areas in Figure

4-4b, there are still significant packing rearrangements as indicated by the increase in Q. These changes are effective at lowering the vdW energy in spite of the surface introduced with the creation of the two "spindle" ends.

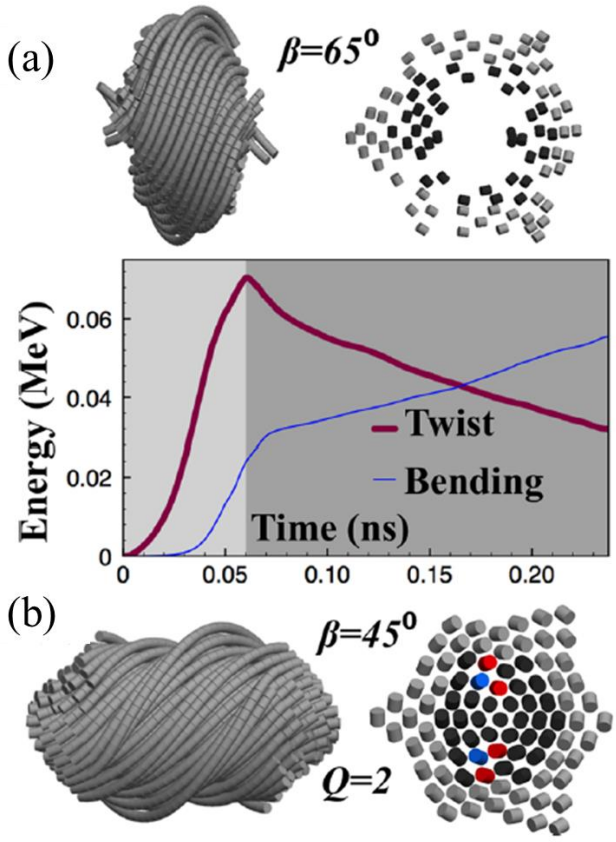

Figure 4-6 (a) "Bird caging" of a twisted CNT rope with L = 41 nm invisible in its cross-section (top). The strain energy during "bird cage" formation. The light-gray area is the loading stage. The dark-gray area is the stabilization stage under T = 64 nm·nN (bottom). (b) Alternative "spindle morphology" arising when the rope is only under geometric twist. In the cross-section, red and blue elements represent 5- and 7-fold packing defects, respectively.

When short and thick CNT ropes are under torsional, they start to demonstrate unique interesting behavior, known as "bird cage", which is observed in twisted macroscopic ropes. The obtained nonmonotonic dependence of cohesive energy on twist,

showing improvement in cohesion when $Q \neq 0$, is consistent with the predictions of previous simulations. [104, 105] It confirms that packing defects are caused by a packing frustration effect. Nevertheless, these packing defects and the formation of local voids, which originate instead in the relaxation of the torsional energy into bending energy, are responsible for $Q > 6$ in the final stages of twisting (dashed line in Figure 4-4b). This explanation transpires more clearly from the similar simulations presented in Figure 4-6a, which considered a shorter CNT rope comprising 91 CNTs with L = 41 nm. Due to the smaller CNT length, this rope presents a smaller vdW cohesive energy. Upon twisting, it develops a large void in its core. Void formation represents an effective way to relax the twist energy stored in CNTs: as can be seen in Figure 4-6a bottom, 41% of the twist energy is released into bending associated with the formation of the bird cage. We have performed complementary simulations on the same rope in which the twist stored in individual CNTs was only geometric. (We ensured the lack of physical twist by carrying out additional relaxations of all angular degrees of freedom, including those of the grip elements, at each incremental step.) We now obtained spindles with small Q values, such as the one shown in Figure 4-6b exhibiting 5- and 7-fold packing defects. Such packings with $Q \leq 6$ are expected when the deformation energy of the filament is small. [104]

To further illustrate the role of twist and bending energy, we perform another group of studies are conducted to approach the pure bending states. Instead of keeping torsional moments, the positions of end grip elements are now fixed but allowed free spin

such that physical twist energy can be released when the moments are removed. The remaining twist energy is confined by geometric twist energy naturally generated from helices of individual tubes. Topological charges under this alternative boundary condition can be significantly reduced to around 6. The 8 topological charges in Figure 4-7f is a consequence of the breakdown of the original assumption that elements in the mid cross section have little out-of-plane motion. In highly twisted morphologies, symmetry is no longer preserved and the calculation of charges loses significance. However, the comparisons between left and right column shown in Figure 4-7 indicate no vacancy in core area is created. In other word, these alternative simulations confirm the role of the large physical twist in the bird cage formation.

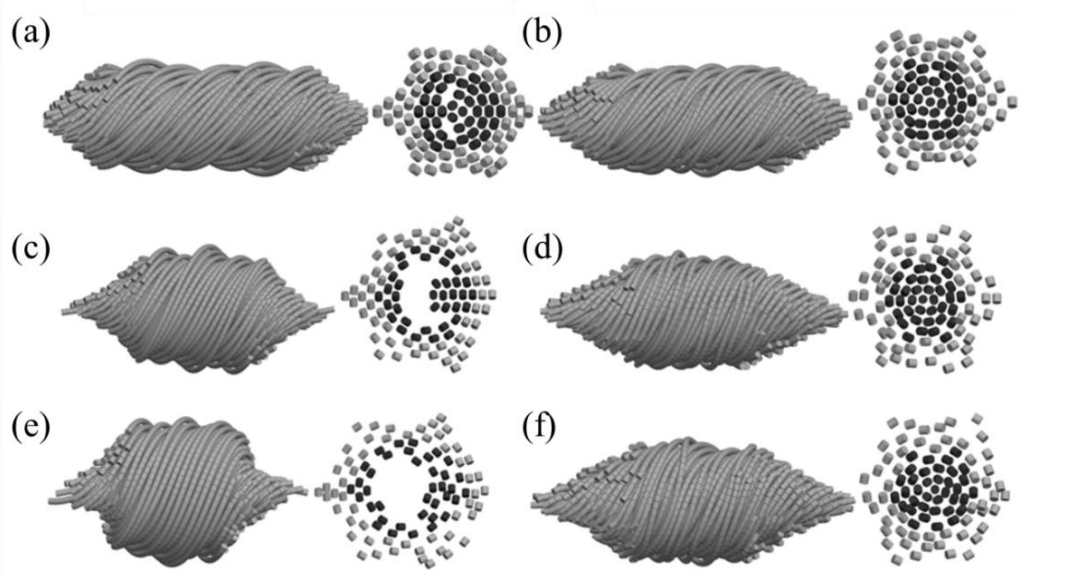

Figure 4-7 Morphologies of twisted CNT rope under boundary two boundary conditions: constant moments (left) and twist relaxation (right). (a-b) T = 40 nm·nN; (c-d) T = 52 nm·nN; (e-f) T = 64 nm·nN. Ropes shown here have L = 67.8 nm and R = 8.7 nm.

Table 4-1 Summary of twist conditions and resulting morphologies shown in Figure 4-7.

Cases	Torsional Load (nm*nN)	Boundary Conditions	Topological Charges	Twist Angle θ (^{0})	Morphology	Rope Radius (nm)
a	40	Constant Moments	12	38.2	Bird Cage	10.5
b	40	Twist Relaxation	4	49.8	Stable Spindle	11.23
c	52	Constant Moments	92	58.93	Bird Cage	13.72
d	52	Twist Relaxation	5	66.57	Stable Spindle	11.5
e	64	Constant Moments	124	68.8	Bird Cage	14.5
f	64	Twist Relaxation	8	70.68	Stable Spindle	12.0

4.4. Energetics and Mechanics of Helix Transformation

For long and thin twisted CNT ropes, a "spindle" is not necessarily the lowest-energy state. The simulation showcased in Figure 4-8 uncovers the formation of a helical geometry when twisting an initially straight rope containing 91 CNTs with L = 163 nm. The evolution of the twist and bending energy components during this deformation is presented in Figure 4-8d. The first shown spindle in Figure 4-8a corresponds to the end of the loading process. When T = 64 nm·nN on the grip elements is maintained, we initially observe a sizable increase in bending energy, which is associated with the progression of the spindle profile. Next, a small lateral instability triggers a dramatic energy transfer, which is marked as Phase III in Figure 4-8d. There is a significant twist-bending transition: 36% of twist energy is released in form of bending within this short chaotic period. This energy redistribution is associated with the formation of a two-windings helix, which at the end of the equilibration stage becomes compact (Figure 4-8c). Regarding the morphology, there is a distortion of rope axis at the

beginning, followed by coiling from two ends. In Phase IV, stable rope helix forms after a shrinkage of pitch and the rope now is condensed to minimize the vdW energy.

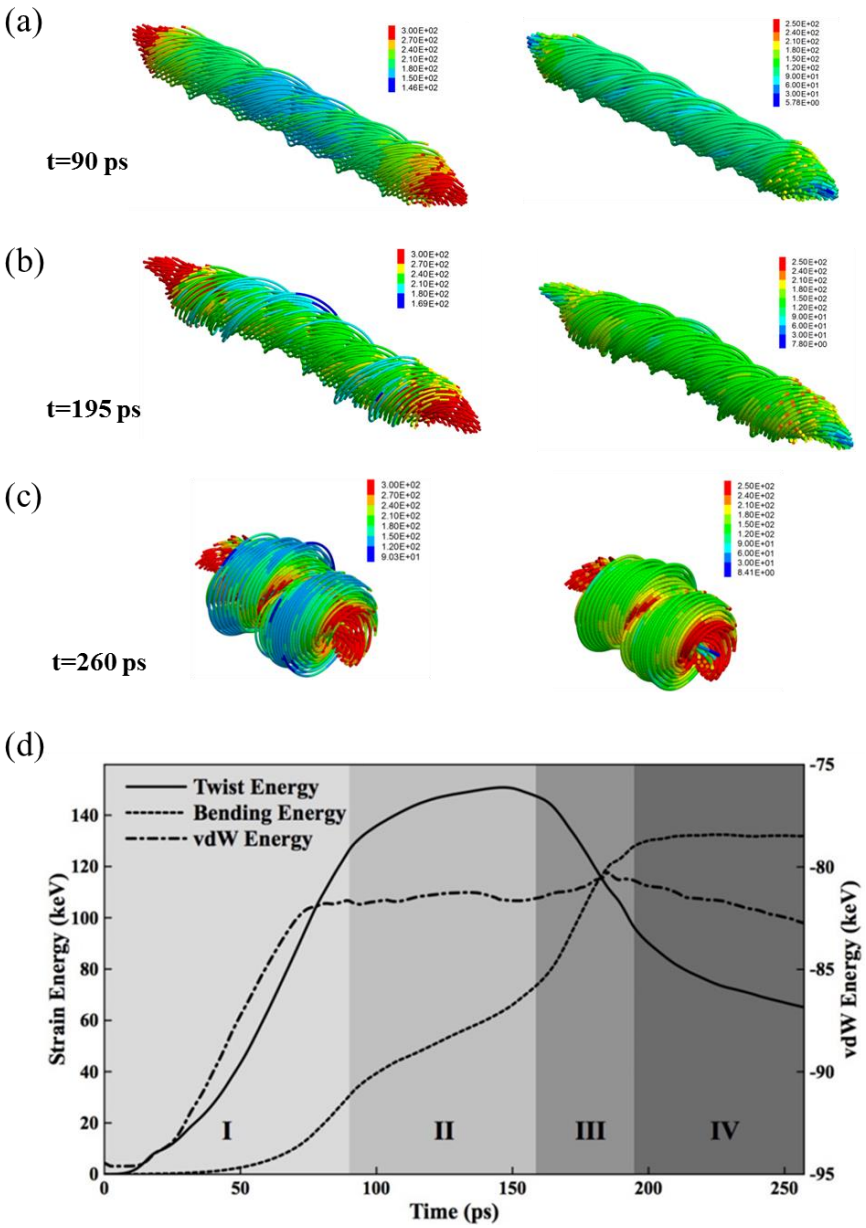

Figure 4-8 (a-c) Straight-to-helix transformation in a rope with L = 163 nm. Color bars show the distribution of torsional moments (left) and bending moments (right) in unit of eV on the corresponding distinct element. (d) Time evolution of the strain energy stored in the parallel bonds. Light area I is loading (steady rate with 0.68 nN·nm/ps). Dark gray region IV is the stabilization stage where T = 64 nN·nm. A–C mark the morphologies shown in (a-c).

For a broader view, helix formation in ideally crystalline ropes 17.2−24.1 nm in diameter comprising CNTs up to 326 nm in length is investigated, which provide better understand of the transformation happening within 50 ps. When the transformation undergoes (Figure 4-9), the structure collapses in the axial direction. Windings start to form as the structure becomes compact. A fully converted helical geometries with similar pitch and radii is found. The pitch is roughly the diameter of the rope in initial state and is a characteristic length of the helix.

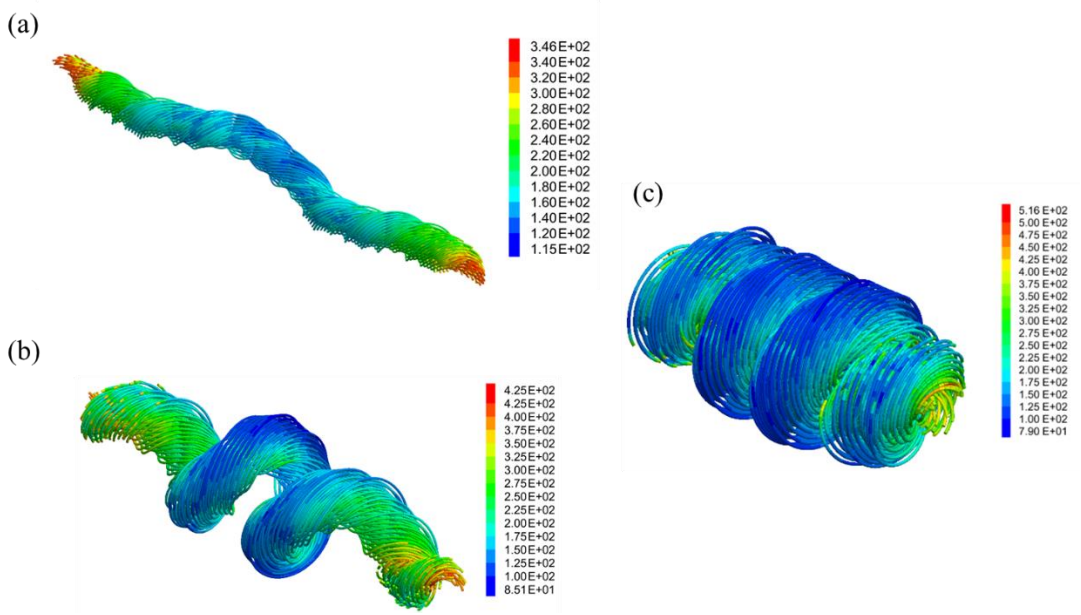

Figure 4-9 Helix formation of a highly twisted long-thin CNT rope (L = 326 nm, R = 8.75 nm) subjected to torsional moments (T = 60 nN·nm, loading rate = 0.53 nN·nm/ps) (a) Helix transformation initiated by a distorted rope axis. (b) Formation of winding. (c) Morphology of compact helices with four windings. Color bars show the distribution of bending moments magnitude on each element in unit of eV.

4.5. Reversibility and Stability of Twisted CNT Ropes

The morphology transformation discussed previously falls into plastic

deformation region, meaning fully recovery of the structure to initial state is not possible by solely removing the torsional loads. CNT ropes first undergo elastic twist occurs, followed by plastic twist when the loading exceeds a critical value, namely twist elastic limit. Playing an important role in plastic twist, topological charges are responsible for breaking down the hexagonal closed packed structure permanently. Dimensions of the bundle are crucial parameters to determine its mechanical properties, especially for relatively short bundle. To investigate on the length effect, a CNT bundle with radius of 5.15 nm (N = 4) is twisted with different torsional moments. Five values of length are chosen: 27.12 nm, 40.68 nm, 54.24 nm, 67.8 nm and 81.36 nm in this study.

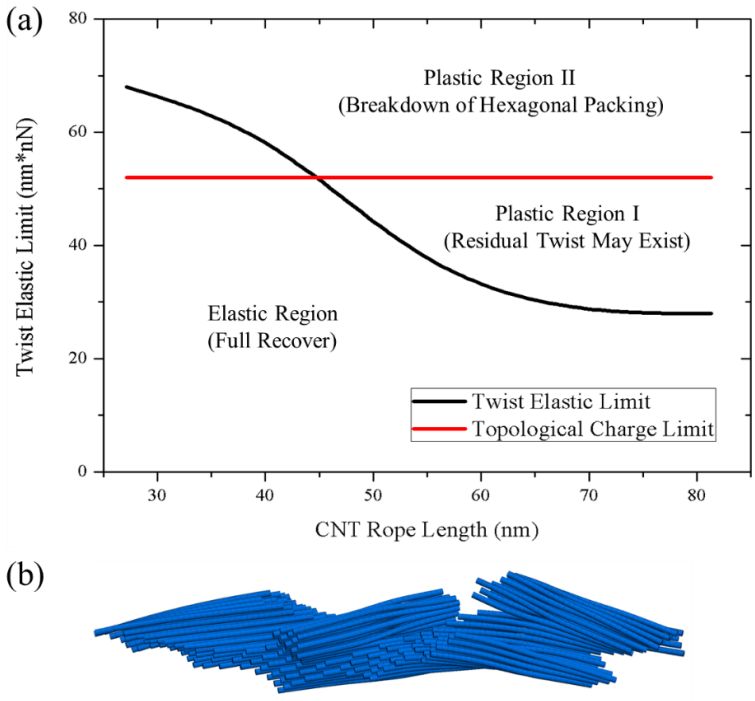

Figure 4-10 (a) Elastic and plastic twist of an N = 4 CNT bundle with various lengths. (b) A typical failure in plastic region II.

As can be seen in Figure 4-10a, topological charges appear at T = 52 nN·nm regardless the length of the rope. The line of twist elastic limit, below which bundles can fully recover from the deformation, is larger for short bundle, while becomes smaller and less sensitive to length beyond 67.8 nm. For long CNT rope, the appearance of topological charges can have equivalent meanings with plastic deformation, since the breakdown of symmetry cannot be recovered in rigid CNT systems. In Plastic Region I, a rope has certain residual twist ($\beta < 10^0$) which may relax in a slow rate depending on the scale of the system. Meanwhile, in Rlastic region II, the hexagon packing that is interrupted by topological charges will not fully reverse.

For extremely short rope, especially, when the axial length is comparable to diameter, topological charges do not influence on the elasticity. Short tubes have benefit to easily adjust themselves when unloading. With the help of alignment moments provided by vdW potential, the tubes reorient and finally the hexagonal packing is fully recovered. Short rope also does not have plastic region I, namely no residual twist. Upon high loading beyond T = 72 nN·nm, peeling and separation are observed as failure modes (Fig. 4-10b).

Besides reversibility, stability is also dependent on geometric dimensions. As discussed before, morphologies of highly twisted CNT rope transform into either bird cage or helix. To investigate this dependence, it is convenient to define aspect ratio $\gamma = L/R$.

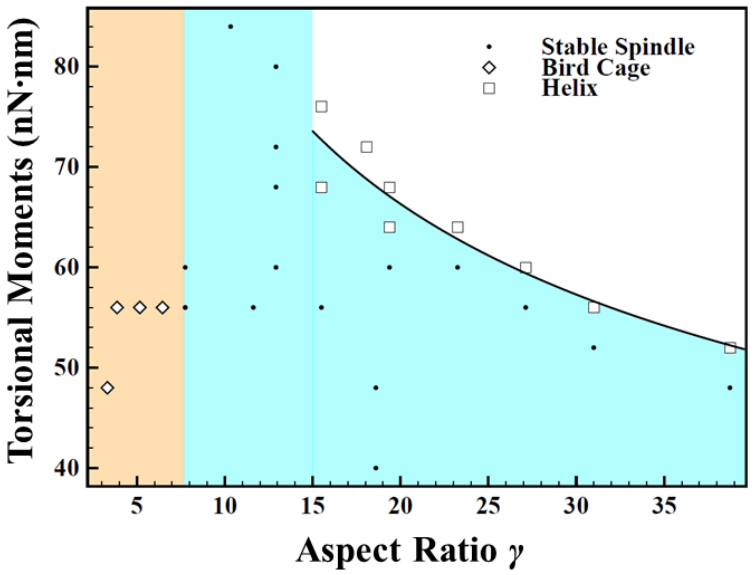

Figure 4-11 Twisted CNT rope morphology phase diagram. Pink region represents Bird Cage favored region; Light blue region represents stable spindles; White region is helix favored region.

The phase diagram shown in Figure 4-11 suggests a general condition for stability of twisted CNT rope. Twisted ropes with γ larger than 15 tend to be axially unstable, when loads exceed a critical value that scales as $\gamma^{-0.36}$, which differs from the γ^{-1} straight-to-helical transition scaling specific to thin elastic rods. [110] Higher loads lead to helix formation as a main mode for twist relaxation. Thick and short ropes with γ less than 8 are considered to form Bird Cages. Upon twisting, excessively generated topological charges are responsible for twist relaxation. A narrow intermediate range between 8 and 15 represents a stable spindle that is able to safely convey torsional loads up to 85 nN·nm, without axial distortion or bird caging.

4.6. Packing Defects and Spontaneity of Twist

The study of topological defects implies that packing of tubes affects the energetics. It is then natural to expect some artificial defects that break down the symmetry may favor the spontaneity of twist state by offering a lower energy state. Similar to the types of defects in crystal structure, defects of packing can also have point and line defects. A point defect here is defined as missing one or several tubes inside the rope. A line defect is created by taking away an array of tubes along the radius or other certain directions.

To investigate the influence of packing defects on twist behavior, torsional moments are applied to a certain level and then completely removed for relaxation. Here, loading and unloading of external axial moments serve as a triggering factor to raise the system energy. Residual twist is evaluated after relaxation by measuring the relative shift angle between two ends.

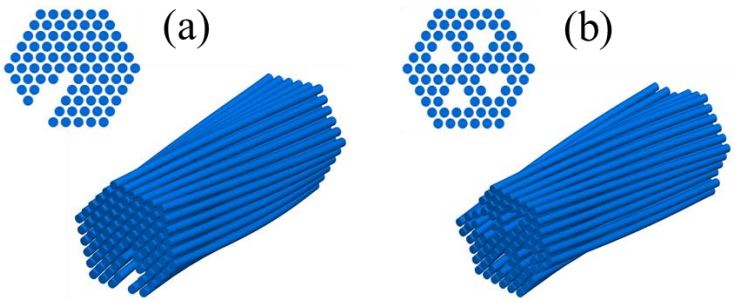

Figure 4-12 Residual twist of defected bundle with their defect type presenting: (a) A line defect (b) Four point defects.

As an example, we consider a CNT bundle with $N = 6$ (91 tubes) and $L = 54.2$ nm. As shown in Figure 4-12, in case a, 8 tubes are taken out to create a wide line defect. In case

b, 12 tubes are missing and four large point defects are formed. It has to be pointed out that small point or narrow line defect, like missing of one single tube or one array of tubes, is not sufficient to break down the symmetry and nor to lead to residual twist. Besides, loading should be controlled within the elastic regime to guarantee full recovery and easy sliding.

A certain degree of residual twist is found after relaxation. Due to the nature of high stiffness of CNT, heavily twisted ropes at an expense of strain energy can never be found spontaneous. Figure 4-13 depicts the shift angle of three defected CNT ropes. Since the defects presented here are artificially generated regarding their location, width and length (defined as "short" if the missing section does not go through the entire bundle length), the results serve as a proof of concept to understand the defects influence on twist phenomena.

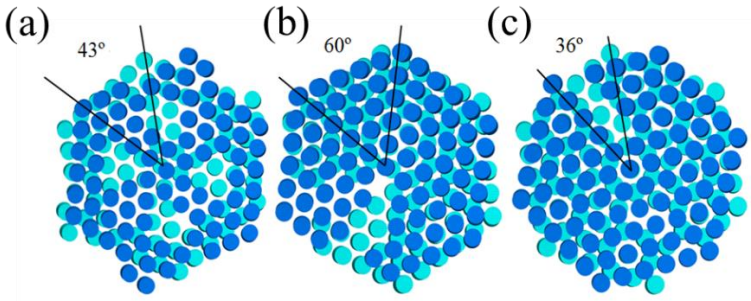

Figure 4-13 Shift angle of CNT bundle with three kinds of defects (view along axial direction): (a) Four-point defects; (b) A wide single-line defect; (c) Two narrow short-line defects (Blue and cyan color represent the left and right end, respectively).

Shift angles in these three cases vary from 36º to 60º, depending on the length and width of the defects. Narrower and shorter line defects tend not to favor the spontaneous twist as much as wider and longer ones. More simulations indicate that the optimal

number of point defects is two, which may favor twist up to 50º. The morphologies of these residual twisted structures are distinguishable from those in torsional tests. One important feature is that most of the individual tubes are still straight. In other word, the entire structure has little physical twist, while their arrangement by changing the orientation introduce some geometric twist.

Table 4-2 Summary of shift angles and energetics of three cases shown in Figure 4-13.

Case	Shift Angle per Unit Length (^{o}/nm)	Residual Strain Energy (eV)	Initial vdW Energy (keV)	Final vdW Energy (keV)
a	0.7934	35	-26.7	-26.8
b	1.107	50.5	-22.9	-23.2
c	0.6642	57.2	-28.2	-28.3

From an energetics point of view, the strain free state involves little strain energy, whereas the vdW energy is slightly lower. It can then be concluded that packing defects may rearrange the orientation of each tube to minimize the surface energy. Nonetheless, such modest energy improvement is unable to produce significant amount of twist. In agreement with theoretical derivation [104], large stiffness of CNTs hinders the spontaneity of twist predicted in general bundle of cohesive filaments.

4.7. Concluding Remarks

The presented simulations of twisted CNT ropes demonstrate that MDEM can capture a rich nonlinear behavior. The initial stages of twisting are dominated by the creation of spindle morphologies and packing rearrangements. There is no contradiction

with the thoroughly investigated conclusion that twisting represents a way to enhance the frictional contact between CNTs. [98, 107] Current study is targeting the different regime enabled by the ability to let the individual CNTs slide freely during deformation. After spindle formation, the rope geometry is dominated by the amount of physical twist stored in CNTs. The strain may relax locally, with defects forming similar to the bird cage defects encountered in wire cables. [111] High-aspect-ratio ropes exhibit a robust straight-to helix transition. Twist insertion to produce helical CNT ropes has been accomplished in experiments [98, 112] and yet has never been simulated. Our simulated helical ropes resemble the experiment ones in compactness (the formed loops are in contact) and "liveliness" (they can untwist) characteristics. Due to the computational restrictions, the MDEM simulated ropes are still shorter and thinner than the experimental ones. Simulating larger ropes would require a more computationally efficient MDEM model, with a larger number of atoms captured in one distinct element. Based on these results, the method can offer further important insights into the structure and mechanics of helical and super-helical CNT ropes and, more broadly, into the complex and widespread problem of finding the relationship among the geometry, internal packing, and fiber mechanics in twisted agglomerates comprising semi-flexible nanofibers. The MDEM scheme emerges as a complementary tool to theory, where the regime of fiber deformation energy dominating the cohesion between fibers remains a challenge.

Chapter 5 Carbon Nanotube Networks by Computational Design[5]

5.1. Introduction

Depending on the chiral vector characterizing the symmetry of conceptually rolling a graphene sheet into a tube, SWCNTs can be either metallic or semiconducting. As-produced SWCNT materials typically contain a combination of these two electronic types. However, recent advances in purification have ushered in an era of research focused on highly monodisperse SWCNTs with ideal colloidal dispersion. [113-115] These purified materials feature a porous structure of SWCNT bundles that show tremendous potential for applications, including transparent conductors, field-effect transistors, and functional layers in photovoltaic devices. [116, 117]

Ultrathin SWCNT networks are electrically conducting and one of the most feasible and promising applications of these films relates to flexible electronic devices. [118] So far, only a limited number of studies have focused on both the mechanics and electrical properties of pristine type-purified SWCNT films. [119-122] Flexural studies of length and type-purified SWCNT films deposited on polydimethylsiloxane substrates, for example, offer a glimpse of the remarkable mechanics (Young's Modulus in order of TPa)

[5] Portions of this chapter have been published in *ACS Applied Materials & Interfaces* (DOI: 10.1021/acsami.7b01434)

of individual SWCNTs, [123] but the weakness of significant strain softening even at small strains [119-121] is also inevitable.

As having been demonstrated in the previous chapters, self-assembling process driven by attractive vdW forces introduces bundling and alignment, which can be intensified by externally applied strain. The network structure evolves under strain disturbance, often irreversibly. As a consequence, the sheet resistance of flexible SWCNT films can be detrimentally impacted by flexure. [102] Although this type electrical sensitivity serves as basic functioning mechanism for strain sensors, the majority of flexible electronics applications demand structural stability, and this type of strain response is clearly undesirable. Physically, two sources of electrical resistance are presented in a percolated network, namely, intrinsic resistance of a SWCNT and the contact resistance between connected SWCNTs. Since the former is practically unchanged under the applied deformation, it follows that a dominant portion of the unwanted increase in resistance suggests a loss of SWCNT-SWCNT contacts, typically at their junctions. Thus, the mechanical and electrical response are tied together, and resolving the durability issue is vital to realizing the next generation of flexible electronics SWCNT-based materials.

To tackle the strain-softening and durability issue, several strategies that have been explored involve strengthening the SWCNT junctions by coating with graphene [124,

[125] and introducing covalent bonding via irradiation. [124, 126-129] By irradiating chemically active carbon atoms through the CNT structures, all types of sp^3, sp^2 and sp bonds can present either individually or in form of combinations. Much stronger than vdW interaction, these covalent bonds prohibit the relative motion via sliding between CNTs and therefore are able to strengthen the entire CNT system. [130] Unfortunately, the dose of irradiation should be carefully controlled, which otherwise leads to vacancies and Stone-Wales defects of CNT surface could reduce the strength by as much as 60% [131] due to breakage of structural integrity. [132, 133] Most importantly, covalent bonds adversely affects the intrinsic SWCNT characteristics, and it is therefore a less suitable strategy for SWCNT films for flexible electronics applications. [129] Since the preservation of intrinsic properties is crucial, we propose a new nanoparticle (NP) filler approach scheme that leaves intact the individual SWCNTs. The added NP phase introduce additional non-covalent interfaces and thereby preserves the exceptional properties of SWCNTs.

This chapter first explores MDEM representation of pristine and hybrid CNT complex networks. Then, through uniaxial tensile tests, mechanical properties are accessed, followed by an investigation of topological stability under external loading. At the end of this chapter, cyclic loading condition is applied to evaluate the energy dissipation and stability against fatigue.

5.2. MDEM Representation of CNT Network

With a rise of observation scale from nanometer to centimeter, CNT network becomes thin film, sheet or buckypaper. From microscopic point of view, CNT network is made of randomly orientated single or bundled CNTs densely packed and entangled in a few thin layers. The MDEM representation of complex network starts with randomly generated "seeds" within a square domain, which define the centroid of each individual CNT. Each tube is growing by adding distinct elements along randomly chosen straight axis. Out-of-plane angle is allowed but confined within 2 degrees such that the entire network is entangled. When the growth reached the domain boundary, periodic boundary conditions (PBC) are applied. Nevertheless, PBC, only enforced in network generation stage, is removed later in relaxation and mechanical tests, as we intend to study the edge effect. Particles, without preferred orientation, are uniformly distributed inside the network. (The detailed contact model involving with NP-NP and NP-CNT is discussed in the next section) Despite the non-overlapping algorithm of PFC in particle generation, a brief pre-relaxation time is still needed to avoid overlap between particles and CNTs.

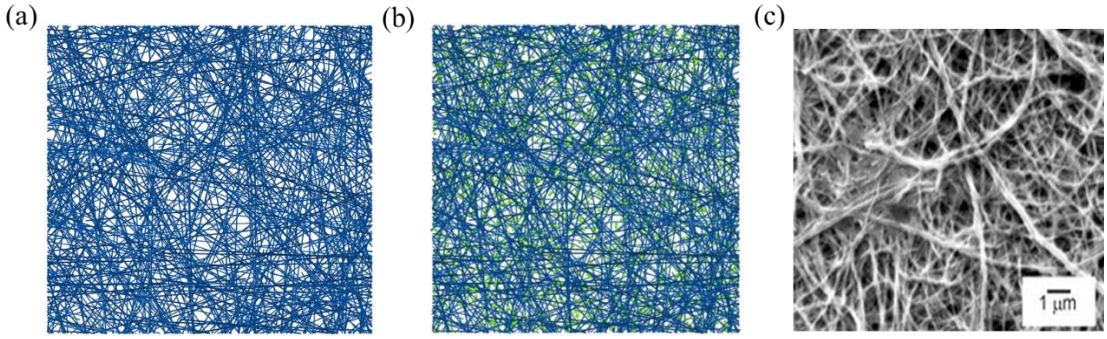

Figure 5-1 MDEM representation of a medium size CNT network: (a) Pristine; (b) Hybrid with 2000 NPs (c) CNT network under electron microscopy [134].

A sample of ready-to-relax network is depicted in Figure 5-1a and b in comparison with a network sample obtained from experiment. Three size of networks are considered in this work, referred as "small", "medium" and "large". Their physical properties are listed in Table 5-1. In this thesis, we mainly focus on the medium size network, since it is more representative in their mechanical properties and also compromises reasonable computational effort. Individual CNT length is chosen to be comparable to the size of network to better study representative fiber properties instead of that of a cluster of small and short fragments. Density and porosity are designed around 0.2 g/cm^3 and 80% to match the experimentally measured values. [135, 136]

Table 5-1 Physical properties of CNT networks designed in MDEM models

Film Size (nm) Length Width Thickness	Number of CNTs	Individual CNT Length (nm)	Number of Si Nanoparticles	Density (g/cm^3)	Porosity (%)
300 300 11	200	271	0/1000/2000	0.18/0.36/0.54	79.1
500 500 11	350	475	0/2000/4000	0.20/0.33/0.46	77.0
1000 1000 11	500	949	0/5000/10000	0.14/0.22/0.30	83.5

Although the current MDEM model cannot fully match the large scale in hundreds of microns, the mechanics of network is essentially the same: randomly distributed and highly entangled CNT fibers interacting with each other through long range vdW forces. One should notice that another difference between the network topology shown in Figure 5-1a and c is bundling and bending are ubiquitously presented. As will be investigated in the Section 4, vdW adhesion is the driven force that reshapes

the landscape of CNT network morphologies.

5.3. Development of Nanoparticle Contact Models[6]

In this work, we consider Si nanoparticles as second phase to fill in the pores of CNT networks. The primary reason for Si as selected materials is because Si is nontoxic, abundant, and it currently dominates the microelectronics industry. At the nanoscale under quantum confinement, silicon also acquires attractive photonic traits, such as a bandgap photoluminescence. In terms of functionality, mixing Si NPs with SWCNTs thus has potential relevance to a variety of devices, such as nanoscale heterojunctions [137, 138] and light-emitting diodes [139].

When nanoparticles (NP) are embedded in CNT films, two types of vdW interactions, namely, NP-NP and NP-CNT, are to be considered. Since the construction of contact models in MDEM requires a full picture of potential energy as input, we first perform molecular dynamics simulations to access the nanomechanics in atomistic level.

Starting with NP-NP interaction, a pair of NPs, 2.5 nm in radius (each has 3870 atoms inside) are initially created with a center-to-center separation distance of 2.5 nm. (As revealed in the pore size analysis in the following sections, such choice of dimension ensures an effective filling without significantly perturbing the relaxed pristine SWCNT network.) One particle is fixed in position, while the other one is displaced by 0.01 Å in

[6] Work in this section is done in collaboration with Dr. Igor Ostanin and his student Grigory Drozdov from Skolkovo Institute of Science and Technology, Mosco, Russia.

each step towards their center line. Classical Tersoff potential [140] (ϵ = 0.01743 eV, σ = 0.3828 nm and $d_{cutoff} = 3.0$ nm) is applied to calculate the vdW energy. Similarly, for the NP-CNT interaction, the fixed Si particle is replaced by a segment of (10, 10) CNT, 10 nm in length. Based on same classical Tersoff potential (ϵ = 0.008902 eV, σ = 0.363 nm and $d_{cutoff} = 3$ nm), vdW energy is integrated at each static position.

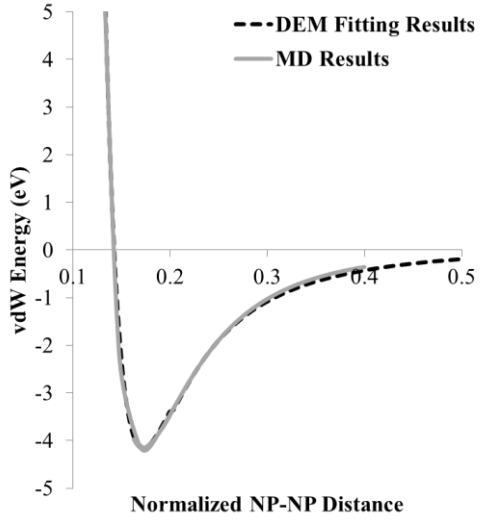

Figure 5-2 MDEM fitting of NP-NP potential using isotropic model in Eq. 25.

In MDEM, nanoparticles are treated as rigid perfect spheres and thus coarse grained as point masses with a simple isotropic potential model between them:

$$V(D) = 4\epsilon_0\left(\frac{A}{D^{\alpha}} - \frac{B}{D^{\beta}}\right), \tag{25}$$

where V is the vdW energy, which is only dependent on D, a center-center distance normalized by the radius of NP. All the other parameters are determined by fitting Eq. 25 with the potential energy from MD simulations (summarized in Table 5-2). This isotropic

model is inspired by the well-known L-J potential and is sufficiently accurate to describe the nanoparticle interaction in MDEM (Figure 5-2).

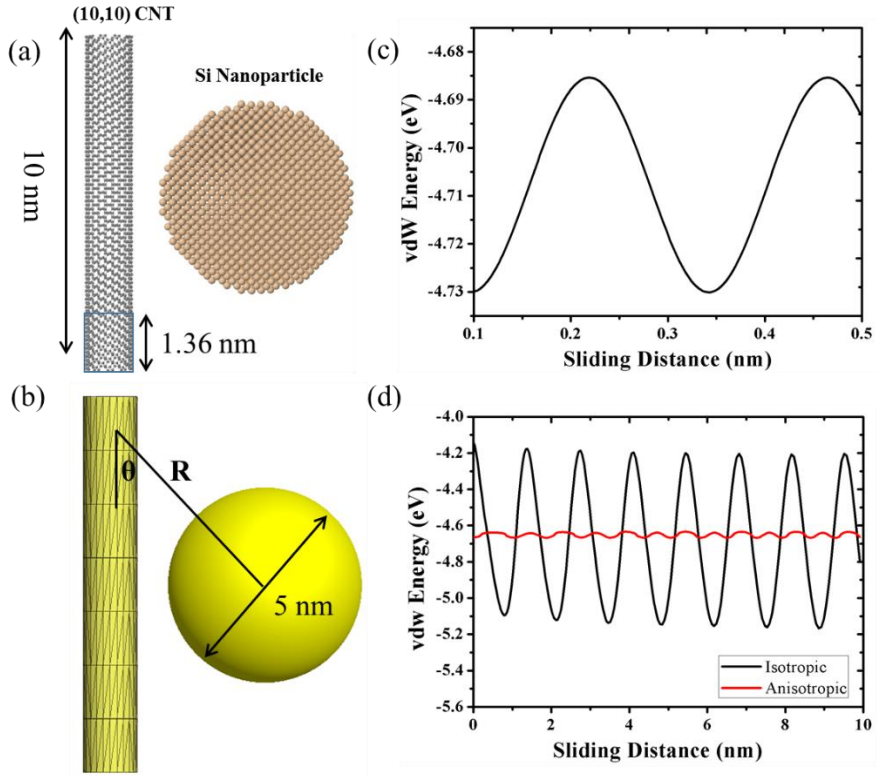

Figure 5-3 (a) Atomistic model of Si nanoparticle and a segment of CNT. (b) Atomistic model incorporated into MDEM representation. (c) Atomistic vdW interaction energy of a sliding nanoparticle along the CNT at equilibrium spacing of 0.346 nm. The periodicity of energy curve is a natural result of length of unit cell, but not artifact. (d) Mesoscopic potential corrugation due to isotropic model compared to modified anisotropic model.

Such simple isotropic model, nevertheless, is unable to accurately describe the complex anisotropic behavior between CNT and NP. As can be seen in Figure 5-3a and b, a CNT segment is now discretized by 7 distinct elements each 1.36 nm in length, while the NP is still modeled as a rigid sphere. Unlike NP, the presence of CNT axis eliminates its isotropy. When a NP is sliding along this axis, isotropic model of Eq. 25 introduces

large vdW potential corrugations (Figure 5-3d). It is essential to point out that at atomistic scale, corrugations naturally exist due to the periodicity of the unit cell in a CNT (Figure 5-3c), while at mesoscale the large variation of potential energy are purely artificial products from isotropic distinct elements. The unwanted energy barrier caused by such artifacts will prohibit NP from smooth sliding, which does not reveal the genuine nanomechanics.

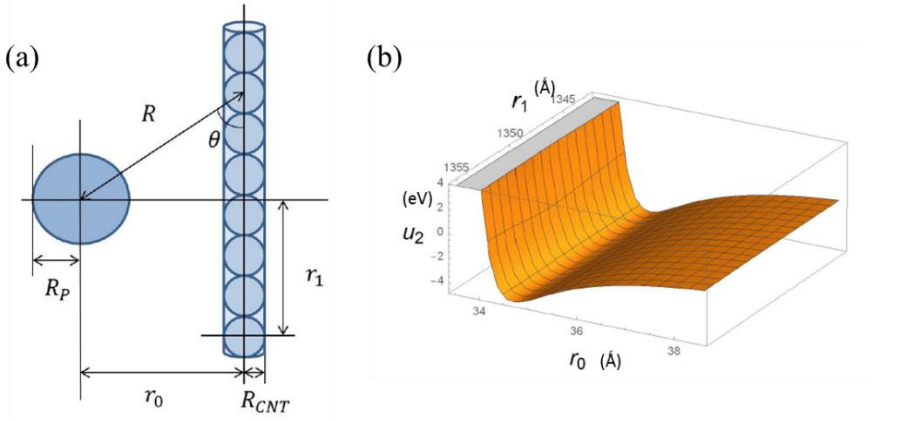

Figure 5-4 (a) Schematic illustration of NP-CNT interaction. (b) Plot of the NP-CNT vdW potential as obtained with the developed MDEM contact.

This difficulty can be overcome by introducing an angle dependence in V. The anisotropic model is well documented in the previous works and Chapter 2 for CNT-CNT interaction:

$$V(R,\theta) = 4\epsilon_0\left(\frac{A}{D(R,\theta)^{\alpha}} - \frac{B}{D(R,\theta)^{\beta}}\right), \tag{26}$$

$$U(R,\theta) = V(R,\theta) f_c(R), \tag{27}$$

D is now a distance modified by a shifting angle θ between NP and an element on CNT

(Figure 5-4a). To determine other four parameters, two steps of fitting need to be done. First, without sliding (r_1 is fixed), the total vdW energy between NP and 7 elements is:

$$u_1(r_0) = \sum_{i=0}^{6} U(\sqrt{r_0^2 + (r_1 - 2iR_{CNT})^2}, \arctan(\frac{r_0}{r_1 - 2iR_{CNT}})). \quad (28)$$

If each NP-CNT distance in MD simulation is denoted as R_i with corresponding vdW energy v_i, the standard deviation generated by using Eq. 28 is:

$$S_1 = \sqrt{\sum_i (u_1(R_i) - v_i)^2}. \quad (29)$$

Second, with consideration of translational sliding (r_1 is a variable), we consider a long enough CNT with n segment (n = 200, for example). The total potential energy becomes:

$$u_2(r_0, r_1) = \sum_{i=0}^{n} U(\sqrt{r_0^2 + (r_1 - 2iR_{CNT})^2}, \arctan(\frac{r_0}{r_1 - 2iR_{CNT}})). \quad (30)$$

Shifting r_1 by a random distance Δr ($\Delta r < 2R_{CNT}$) in each step, the standard deviation of resulting energy difference will be:

$$S_2(r_1, r_0) = \sqrt{\sum_{i=0}^{2R_{CNT}/\Delta r} \left(u_2(r_1, r_0) - u_2(r_1 - \Delta r, r_0)\right)^2}. \quad (31)$$

The focused fitting region is around the equilibrium position obtained in MD, where U is lowest. The corresponding r_0 is 34.62 Å. Then, the target function S for minimization can be written as:

$$S = S_1 + S_2(200R_{CNT}, 34.62), \quad (32)$$

where R_{CNT} is 6.78 Å. Bringing four parameters in Eq. 26 into consideration, the minimization of standard deviations yields: $S_1 = 0.057$ and $S_2 = 1.5$, with constant *A, B,* α and β listed in Table 5-2 below.

Table 5-2 Parameters of CNT-CNT, CNT-NP and NP-NP vdW contact models.

Contact Models	ϵ_0 **(eV)**	*A*	*B*	α	β
CNT-CNT [65]	0.003733	0.0223	1.31	9.5	4
CNT-NP	0.005407	58.1	14.2	8.34	3.32
NP-NP	0.009105	0.0188	0.2519	5.62	4.3

The fitted anisotropic function is plotted in Figure 5-4b. The smoothness of such potential well along the translational direction will guarantee the motion of NP almost identical to their corresponding behavior in nanoscale, except for the small potential energy fluctuation due to unit cell periodicity, which has negligible influence in mesoscale.

5.4. Relaxation and Bundling Effect

Due to vdW attraction, adjacent CNTs will assemble into triangular crystalline packing (discussed in Chapter 3) for sake of energy minimization and will further evolve in bundled ropes. The highly entangled topology, on the other hand, is acting against such bundling by hindering the free motion of tubes. Bending strain energy thus increases as a penalty. The structure is considered to be stable given these two energy terms are either balanced or unchanged.

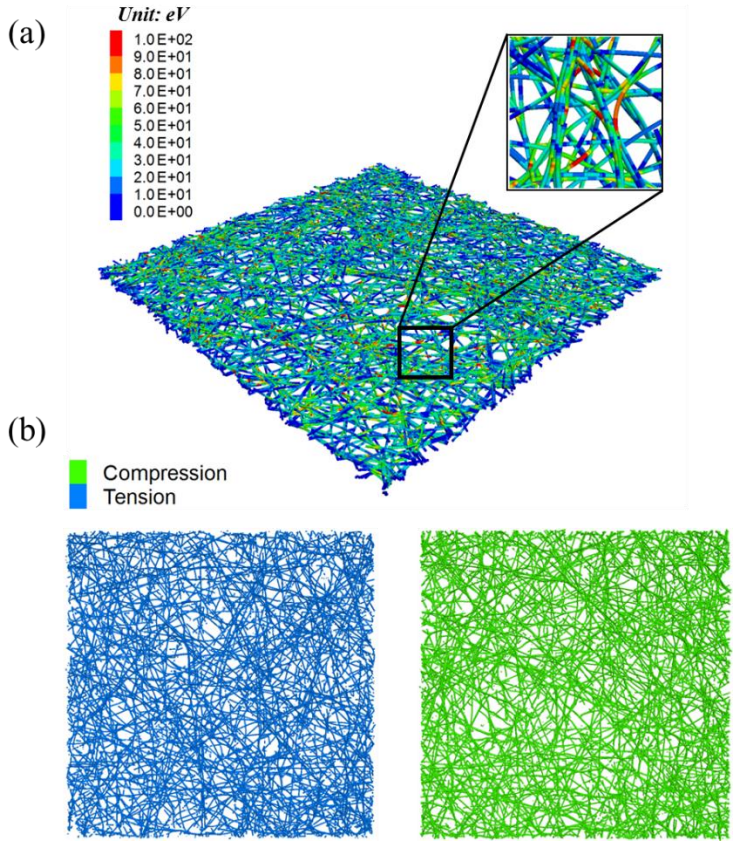

Figure 5-5 (a) MDEM simulated SWCNT network, measuring 500 nm x 500 nm x11 nm in size, after 4.5 ns relaxation. Color reflects the magnitude of the bending moments stored by the parallel contact bonds. Inset details a SWCNT bundle and a bent SWCNT. (b) Force chains (tension and compression) in the relaxed SWCNT network.

Relaxation has dominating impact on stability and mechanics (details discussed in next section). To arrive at a stable structure, the random network of straight SWCNTs (Figure 5-1a) is allowed to evolve in time under the influence of the non-bonded interactions. Figure 5-5a and b displays the characteristics of a typical free standing MDEM simulated network featuring a structure of entangled SWCNT bundles. This network (referred as medium size) was constructed from 350 SWCNTs each 475 nm in length, and has a density of only 0.2 g/cm^3.

As documented in Figure 5-6a, the "hands-off" MDEM relaxation leads to a significant total-energy lowering, despite the accumulation of strain in SWCNTs. In the initial stages (not shown), the relaxation is dominated by the excluded volume (i.e., repulsive non-bonded component) interactions, which act to quickly separate SWCNTS that are crossing too closely. The landscape in relaxed network now shares major similarities (bundling and bending) with Figure 5-1c. Again, on the ns time scale, the relaxation process is driven by the attractive vdW interactions, which act to increase bending energy and lower vdW cohesive component. For example, the network in Figure 5-5a stores significant strain energy, 96% of which is the bending visible also in the color code. In addition to shear stress, the network also stores a small amount of tensile and compressive stress, which is isotropically distributed (Figure 5-5b).

Besides energy, a concept of "aligned pairs" in element basis is introduced to quantify the bundling effect in the network. An aligned pair is defined as two distinct elements located in a parallel manner with a spacing distance closed to their equilibrium distance (1.7 nm). In terms of implementation in PFC, the aligning criteria are set as two elements with crossing angle $\gamma < 10°$ and spacing $d < 1.8$ nm (in tolerance of a small distance sliding or shifting). When both conditions are met, they are counted as an aligned pair. Counting the number of aligned pairs quantifies the degree of bundling inside the network under time evolution.

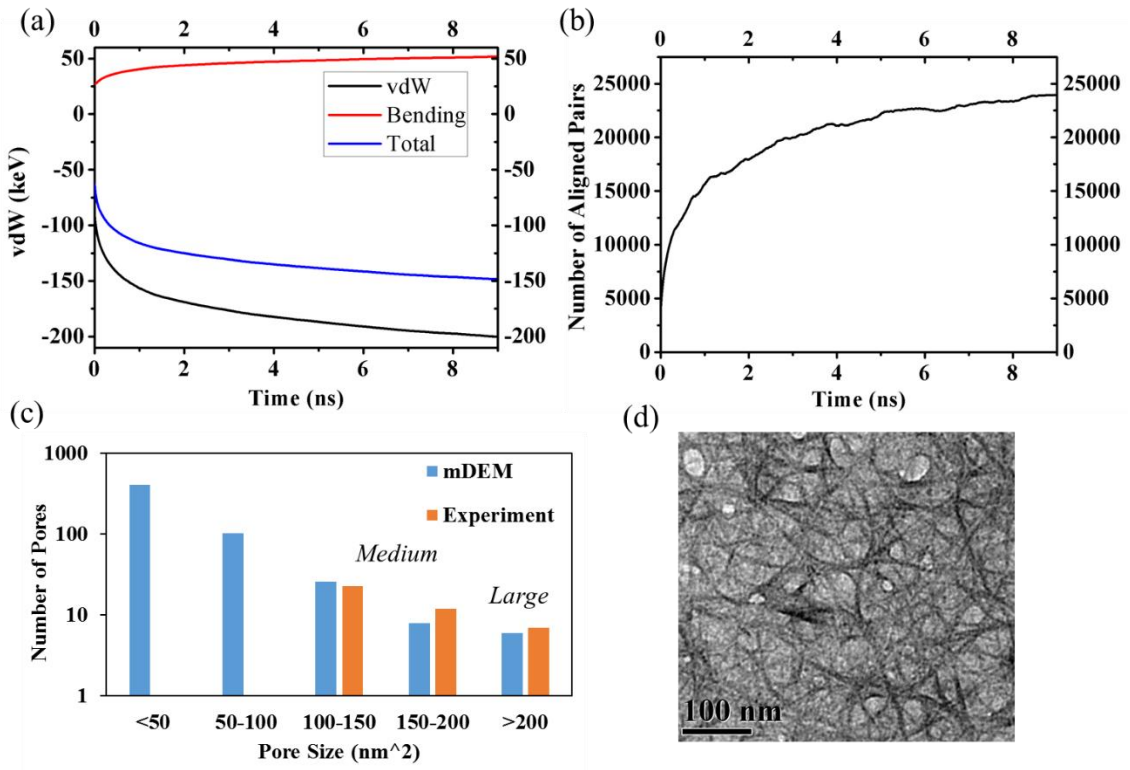

Figure 5-6 Property changes during the relaxation process of the medium size CNT network (a) Energy evolution (b) Number of aligned pairs (c) Pore size of the relaxed network compared to experimental data (d) CNT network prepared in experiments[7].

During the relaxation process leading to structure shown in Figure 5-5a, there is a significant increase in the number of distinct elements in vdW contact that are also aligned. From microstructure's point of view, this behavior reflects network relaxation via zipping process, [124, 141, 142] a topological transformation in which crossed SWCNTs gradually bind. After 2 ns, the increase in the number of aligned pairs slows down significantly, and that the network structure appears to stabilize at around 4 ns. In agreement with experiments, [102, 141] the formation of SWCNT bundles is massive (see the inset of Figure

[7] Sample was prepared in experiments conducted by collaborator Prof. Erik Hobbie from North Dakota State University, Fargo, ND.

5-5a), i.e. local aggregates of several SWCNTs. Note that the SWCNT bundling during the film relaxation is well captured here owing to the realistic description of vdW interactions provided by the anisotropic mesoscopic vdW potentials. [54, 65]

The third factor to trace the relaxation process is the pore size. In porous materials, as an approximation, we measure the "pore area" with imaging processing in their 2D projection. Irregular shaped pores are represented by pixels in black and these contiguous "black pixels" are recognized as pores. The simple method allows us to calibrate the film morphology with a distribution of pore size. The characteristic dimensions of many "medium" (100-to-200 nm^2) pores and "large" (200-to-300 nm^2) pores listed in Figure 5-6c, are in good agreement with the ultrathin networks prepared through the vacuum filtration of aqueous SWCNT solutions (Figure 5-6d). [102]

Now, with particles, the relaxation differs significantly. The randomness of initial ready-to-relax network already introduces pores and entanglement. The presence of particles around entangled crossing point or filling in the pores can delay the aligning process and thus preserve the topology. As a proof of concept, we pick up a pair of CNTs 67.8 nm in length (50 elements each). They are set at equilibrium spacing (1.71 nm) but with a crossing angle of 30º (Figure 5-7a). After placing a particle between the arms, hands off relaxation follows. By tracking the aligned pairs defined previous in Section 3, the aligning process can be accurately detected. Without the particle, such simple

configuration fully aligned around 0.75 ns. The presence of one particle doubles the relaxation time which can be further delayed to 2.3 ns if two particles are placed on each side. It is worth nothing that the particle, eventually squeezed out due to unbalanced vdW forces, delays the aligning process but does not ultimately lock the structure. Yet, it is expected that the complexity in network topology can cage the particles and handicap their motion as well. Under such scenario, network-particle system will be stabilized in a mutual benefit way.

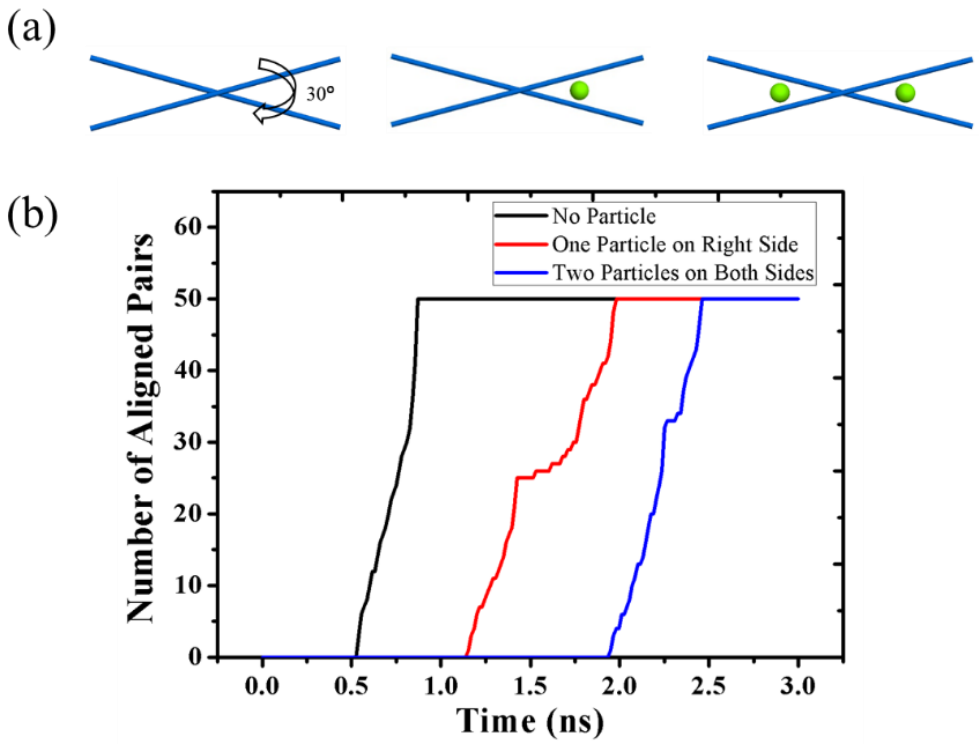

Figure 5-7 Particle influence on alignment: (a) A simple demo of two CNTs with a 30-degree crossing angle interfered by no particle, one particle and two particles on both sides. (b) Time evolution of aligned pairs of three configurations.

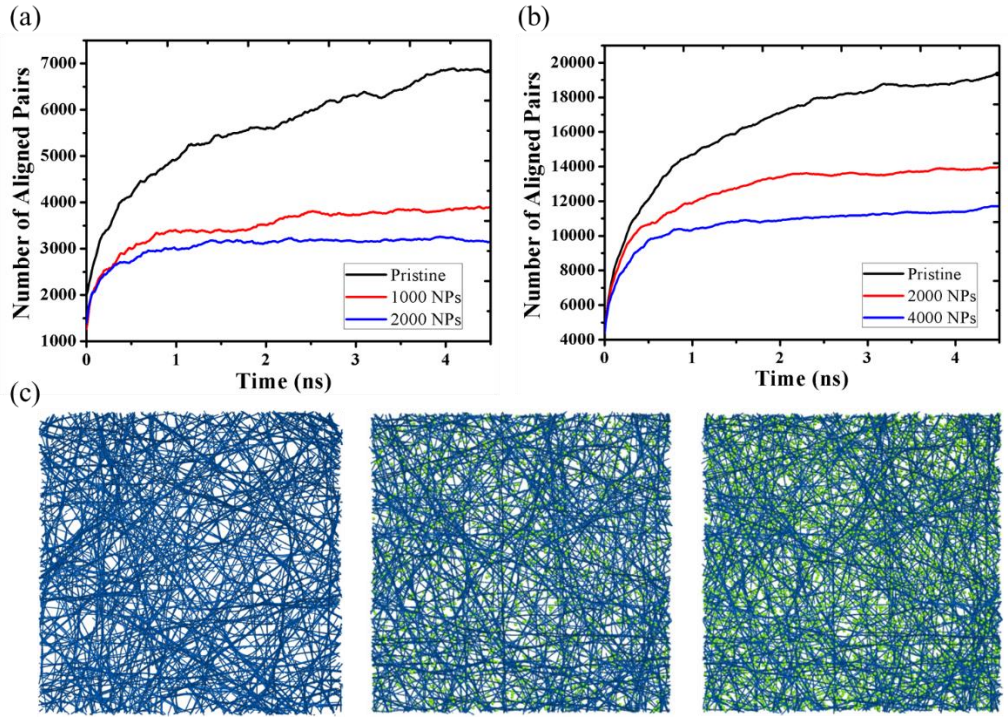

Figure 5-8 Number of aligned pairs in relaxation under the influence of NPs (a) Small size network (b) Medium size network (c) Relaxed medium size CNT networks in three cases: pristine, filled with 2000 NPs and 4000 NPs (correspond to a volume fraction of 4.8% and 9.5%).

The theory of excluded volume in polymer science [143] can be borrowed to explain the delay of alignment. Particles naturally occupied the space between two crossing CNTs and through vdW interaction, they present strong repulsive forces against their neighbors. Such foreign repulsion temporarily counterbalance the aligning force supplied by vdW attraction from two CNTs. To further validate this concept in bulk materials, NPs are deposited in ready-to-relax network. Given 4.5 ns for relaxation, the networks in pristine state consist of massive bent bundles, while with particles, most CNTs are preserved to be straight (Figure 5-8c). The entire structure undergoes little change since CNTs become sessile from motion. More evidence can be found through

number of aligned pairs. In Figure 5-8a, small size pristine network is never stable as number of aligned pairs keeps increasing. With particles, however, the bundling is significantly prevented after 2 ns. In Figure 5-8b, medium size pristine network stabilizes around 3 ns, but 2000 particles help advance this time to 2 ns. By doubling the concentration to 4000 particles, the stabilizing time is up to 1 ns.

Two conclusive statements can be drawn from analyses in Figure 5-8. First, nanoparticles effectively stabilize the network structure by offering repulsive forces against the vdW attraction leading to bundling. Second, stability of pristine network is dependent on dimensions. Shorter CNTs create less entanglement to prevent bundling. Hence, the small size network is hardly stable at least from current observation time scale.

5.5. Elasticity and Deformation Mechanism

The implementation of nanoparticle contact models in MDEM enables modeling hybrid CNT network. Mechanical properties of the CNT networks are accessed through uniaxial tensile tests. In MDEM simulations, two thin layers of distinct elements at the left and right edges of a film were designated as grips. Displacement controlled loading was enabled by prescribing that both grips accelerate from zero to the given velocity during 0.6 ns. This acceleration period is used to reduce the undesired dynamic response, which is significant in case of instantaneous acceleration of the grips. In the series of

simulations discussed, the network is elongated at the constant strain rate of 10^{-7}/fs. Stress is obtained from unbalanced forces accumulated from the gripped elements. Since a constant cross-sectional area is assumed, engineering strain-stress relation is expected.

There are two reasons to relax the network before tests. First, from point of view of manufacturing, composite CNT thin film is often through vacuum filtration of particles into the pores [102]. The network structure prior to filtration is thus already relaxed.

Table 5-3 Young's Modulus of pristine CNT networks before and after relaxation measured from uniaxial tensile tests.

Configurations	Relaxed	Ready-to-Relax
Small	5.4 GPa	7.0 GPa
Medium	9.9 GPa	13.1 GPa
Large	8.3 GPa	9.5 GPa

Second, relaxation reduce possible artifacts in the model. In small strain regime (<2%), we measure the Young's modulus of both ready-to-relax and relaxed network, summarized in Table 5-3. Relaxed networks have lower Young's moduli which fall into the reported values of 0.2 - 12.2 GPa of pristine buckypaper (random network) [144] and significantly smaller than 100 - 150 GPa of fully aligned bundles [145] as expected. Stress-strain relations of unrelaxed network depicted in Figure 5-9 (dash lines) have non-zero starting points. Although only straight CNTs are generated in initial state, there are still physical overlaps at some junctions. Without relaxation, such overlaps introduce

internal strain and further raise the stress level, which is an artificial effect. It is now evident that relaxation is a prerequisite for mechanical tests. Through multiple tests, we also note that as the size of network increases, the measured moduli are more consistent. Although small size has advantage of saving computation resource, the lack of stability and representability makes it unsuitable for mechanical tests. It is therefore ruled out for further studies.

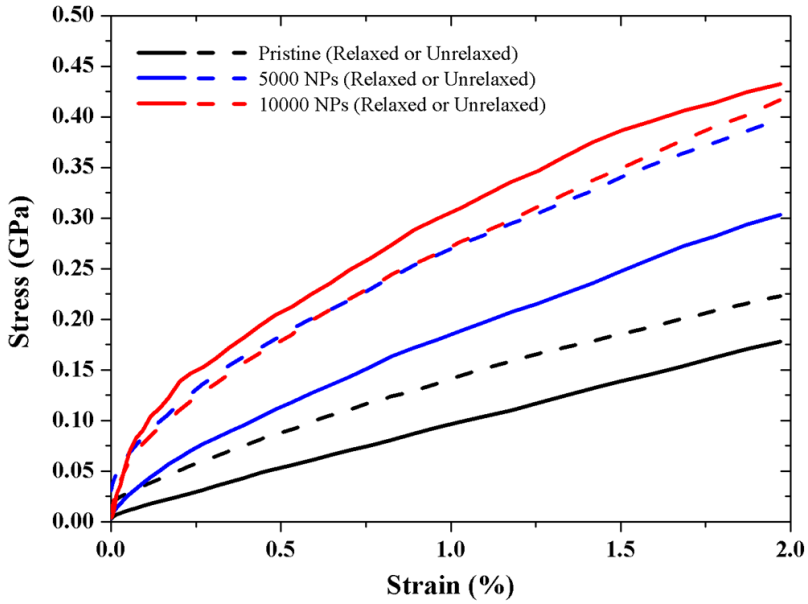

Figure 5-9 Engineering stress-strain relations obtained through 2% uniaxial tensile tests on large size CNT networks. Particles are deposited either before or after relaxation. Moduli of pristine, 5000 NPs and 10000 NPs are measured as 9.5 GPa, 21.5 GPa and 22.8 GPa for unrelaxed network; 8.3 GPa, 13.3 GPa and 15.0 GPa for relaxed networks.

To match the realistic scenario, CNT network is relaxed for 4.5 ns (150,000 cycles in MDEM simulation) and particles are deposited afterwards. With an externally applied strain up to 2%, we focus on mainly the elastic regime (strain range of 1% - 2%). Figure 5-9 displays the strain-stress relations compared to the previous unrelaxed networks.

Young's moduli are measured as 8.3 GPa, 13.3 GPa and 15.0 GPa in relaxed networks. With presence of 10000 NPs, Young's modulus is enhanced by 93% compared to pristine network. Since the network is already relaxed, the enhancement is a solo result from the particles.

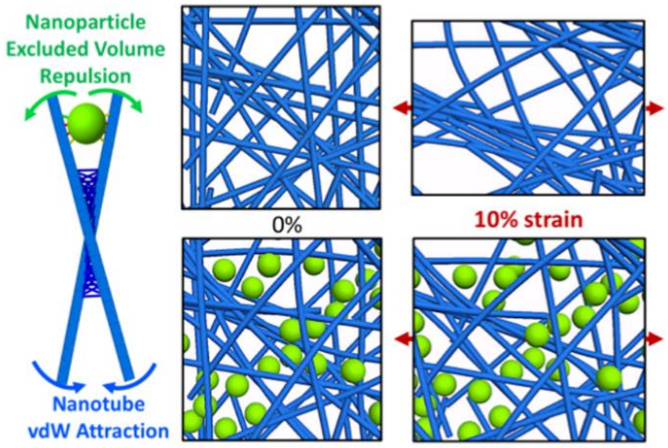

Figure 5-10 Role of nanoparticles in mechanics of CNT network.

The excluded volume repulsion, discussed in Section 4, enables load transfer through the vacancies, namely, pores inside the network. Figure 5-10 captures the local load transfer effect from the nanoparticles. Under 10% strain, pristine network is largely bundled, with a simultaneous loss of stable triangular framework. With particles, local frameworks are substantially supported and the entire structure is well maintained. The repulsive forces from nanoparticles redistribute the load transfer paths in a uniform manner.

Deformation in such porous materials happens through either sliding between

tubes or transferring loads on tubes. There are two procedures to transfer loads through the network during the tensile tests. The desired and primary procedure is to pass tensile forces on directly individual CNTs, which have superior ability to resist tensile deformation. When tension is applied, those tubes sharing the load direction will first undergo stretching. The secondary procedure is through reorientation, meaning CNTs scattering around now have to reorient in tension direction and then make a contribution. By monitoring the tensile force on parallel bond contacts, one can visualize these two procedures during the deformation process and quantify the load transfer ability. As can be seen in Figure 5-11a, at 1% strain level, there are random isolated spots in the network starting to develop tensile forces. Prior to 1% strain, little tension is carried by tubes, meaning that the deformation is dominated by sliding between CNTs rather than their elongation. Sliding via vdW interaction is an undesired deformation mode that weakens the structure, since the high stiffness of CNT is hardly contributing. This also explains the lower stress level of pristine network shown in Figure 5-9.

With particles, tensile forces are uniformly carried by CNTs on the edges (Figure 5-11b). As elongation proceeds, tension propagates through the center, similar to deformation of crystalline solid. With more CNTs now are resisting tension, mechanical strength of the entire structure is also enhanced. At the final stage of 2% strain, large tension has already developed through the network, while in pristine case, many CNTs on edges are still subjected to sliding mode.

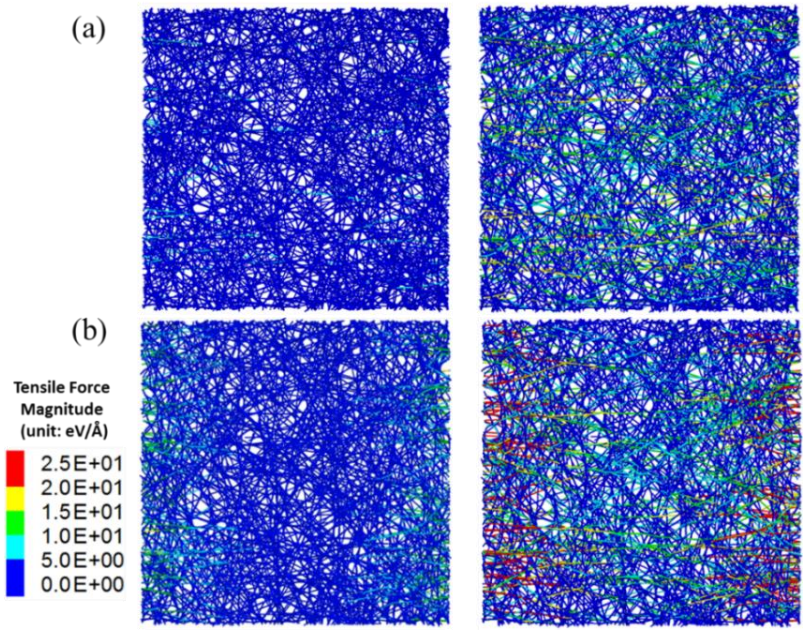

Figure 5-11 Tensile force development within large size CNT network: (a) Pristine network under 1% and 2% strain; (b) Hybrid network with 10000 NPs under 1% and 2% strain. Particles are not shown for clarity.

Load transfer ability is quantified by measuring percentage of CNTs that convey tensile loads. Figure 5-12 displays the force chain of large size network under 2% elongation. It is found that 57% and 84% of CNTs are under tension in pristine and hybrid case, respectively. In pristine network, CNTs under compression are generally wavy and bent, indicating a lateral shrinkage exists. In hybrid network, the remaining CNTs are in vertical direction that cannot contribute to load transfer in horizontal direction. Therefore, 84% is reaching the maximum percentage of CNTs that are able to contribute in effective load transfer without disturbing intrinsic topology of the network.

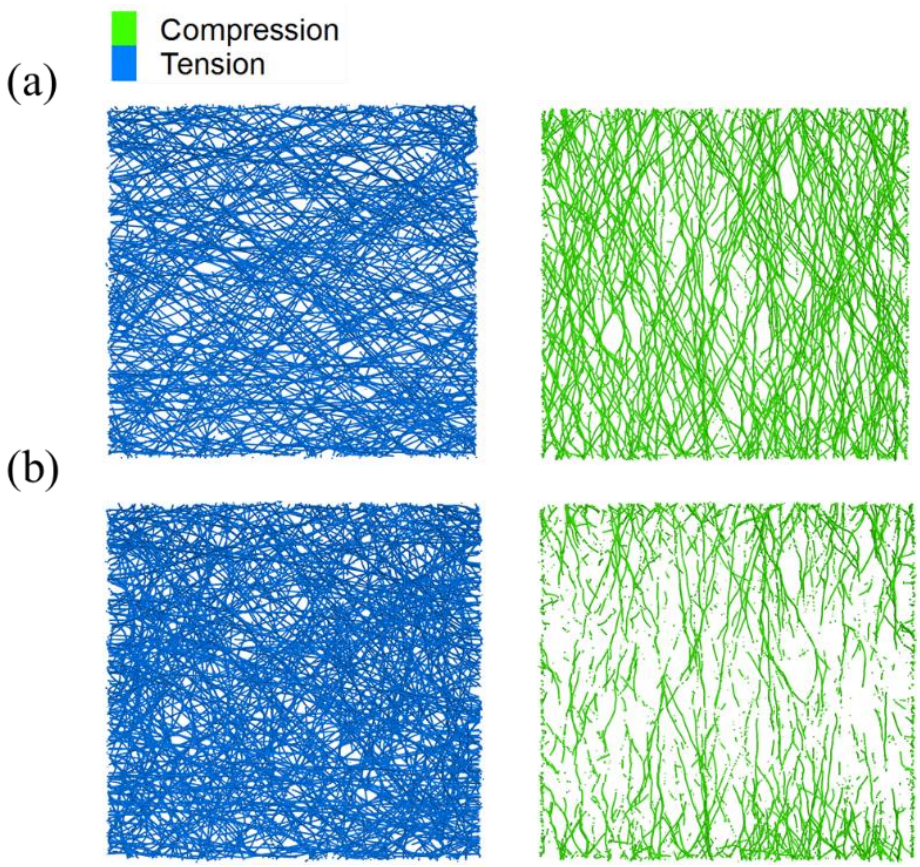

Figure 5-12 Force chain (tension and compression) of large size CNT network under 2% tensile strain: (a) Pristine network; (b) Hybrid network filled with 10000 NPs.

Large externally applied strain will lead to yield of the network. In crystalline solid, yield is often viewed as breaking bonds and shifting atomic layer with motion of dislocations. In amorphous CNT network, yield can be viewed as rearrangement of individual tubes in an irreversible manner. If a relaxed network is assumed to be quasi-stable, an external strain will break the equilibrium by disentanglement and then favors alignment in tensile direction. Therefore, when yield occurs, the secondary load transfer procedure is also activated. As Figure 5-12b shows, to further promote load transfer, either larger tensile forces should be carried on individual CNTs or those

vertically aligned CNTs have to be reoriented in order to make a contribution. Figure 5-13a demonstrates the strain-stress relation up to 20% strain together with an evolution of aligned pairs to detect the degree of bundling due to such forced alignment. Yield is estimated at 3% strain (Point A) for pristine network, while at 6% strain (Point B) for hybrid network. Nanoparticles are capable to postpone yield.

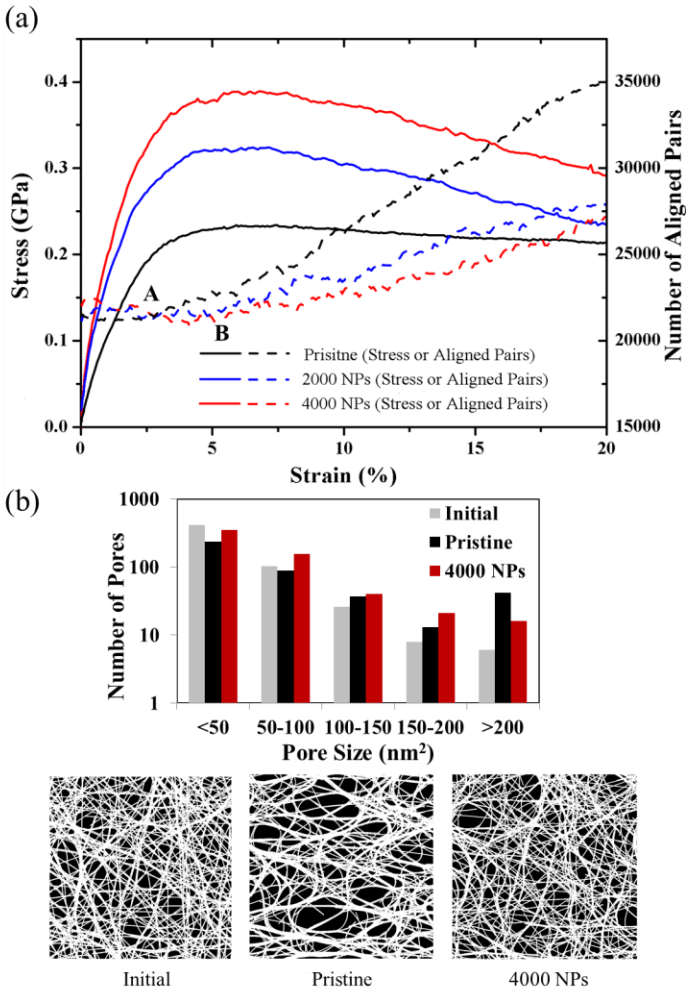

Figure 5-13 (a) Engineering stress-strain curves and evolution of aligned pairs in large size pristine and hybrid CNT networks. Point A and B represent yield points of pristine and hybrid networks, respectively. (b) Pore size distribution in the initial and stretched CNT networks. Local microstructures highlighting opening of pores during stretching are shown below.

As the network elongates, it decreases significantly its lateral dimensions. Although the tensile stress in individual SWCNTs is modest even at large strains (for the 20% elongated coupon see the color code in Figure 5-14a, a neck develops. These unusual microstructural changes originate in the poor load transfer. Without exploiting the tensile forces on individual CNTs, the structure is now forced to reorient tubes in order to compensate increase of loads. First, starting from the edges, the gripped CNTs begin to slide out of the network. The sliding triggers a massive zipping relaxation as aligned pairs augments drastically after yield (Point A in Figure 5-13a), indicating that zipping-relaxation starts at 3% strain and becomes substantial at larger strains. At 20% strain, the microstructure evolves to almost double its number of aligned contacts, and thus to lower the vdW cohesive energy. This relaxation process is associated with a significant increase in bending strain. CNTs that fail or only partially reorient are now subjected to bending. For example, we find that the 20% stretched network doubled its amount of stored bending energy. At the same time, the network acquired a negligible amount of tensile stress during the massive relaxation. The side effect is also visible by inspection in the thickening of the bundles and the increase in the size of the larger pores of the network (Figure 5-13b). External forces shift the pore size distribution and 42 large pores (>200 nm^2) are found inside the stretched pristine network compared to only 6 in the initial state.

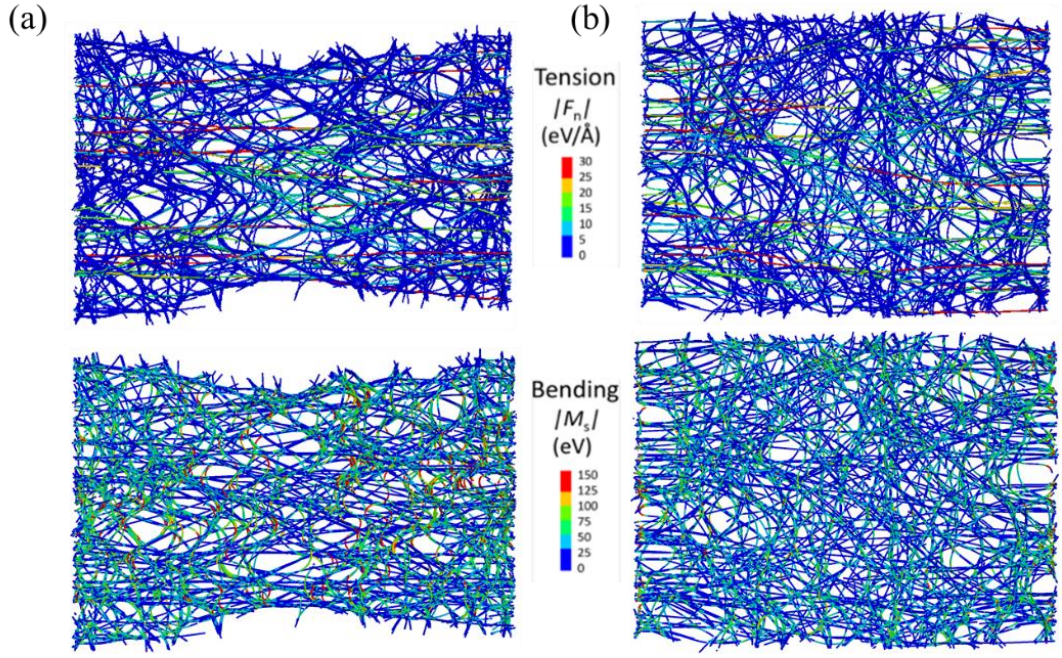

Figure 5-14 Medium size CNT network (same as in Figure 5-5a) under strain showing 37% transversal shrinking in the middle compared to the initial state. Color reflects the magnitude of the tensile force (above) and bending moment (below) stored by the parallel contact bonds. (a) Pristine; (b) Hybrid with 4000 NPs.

Hybrid network behaves in a strikingly different manner under 20% strain. A direct comparison between Figure 5-14a and b reveals that the effectiveness of the added excluded volume contacts. In hybrid network, necking is totally absent with a uniform but negligible shrinkage of 2%. By inspecting the color code, one can observe that the individual CNTs carry more tensile load. Compared with the pristine case, there is significantly less non-affine bending deformation. The evolution of the number of aligned pairs, Figure 5-13a, indicates that zipping relaxation process is significantly inhibited. For example, under 20% strain, the increase in the number of aligned pairs is about 50% less than in the pristine case. The major contribution in aligned pairs comes from the gripped

edges where CNTs start to be pulled out and disentangled, suggesting that yield occurs first at edges. Even though the secondary load transfer procedure is activated, the primary procedure still dominates due to failure of alignment of most central tubes. Additionally, the pore size data presented in Figure 5-13b indicates that the added excluded volume interactions are effective in limiting the growth of the larger pores.

Finally, uniaxial tensile tests proceed with 300% strain at which CNT network undergoes substantial fractures. The strain rate is set as $5\times10^{-7}/fs$ to compensate computational cost. It needs to point out in Figure 5-15a that high strain rate yields larger tensile strength and modulus due to time-dependent relaxation during the tests. Instead of linear portion, we focus on the qualitative post-yield behavior.

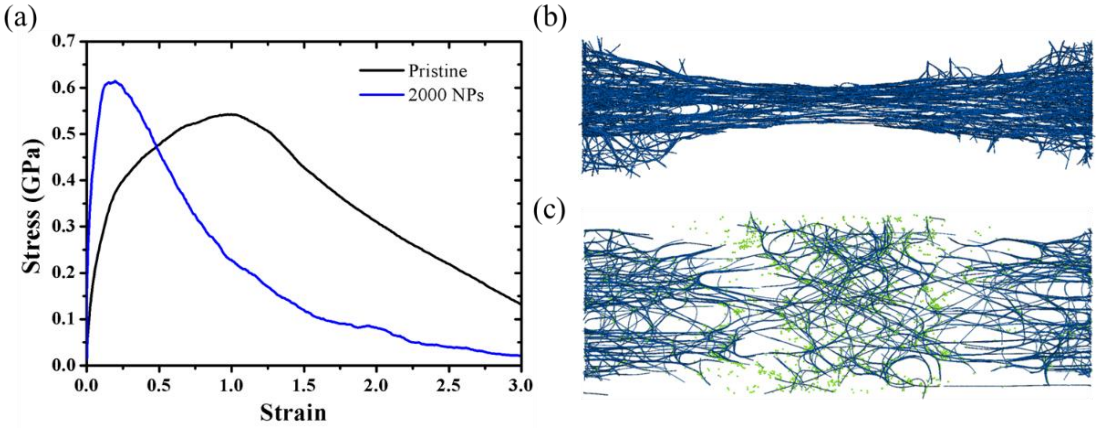

Figure 5-15 (a) Strain-Stress curves of pristine and hybrid medium size CNT films up to 300% strain. (b) Morphology of pristine film under 200% strain. (c) Morphology of hybrid under 200% strain.

As can be seen in Figure 5-15c, excessive presence of particles now lowers the deformability of the network. Instead of alignment, pulling out of CNTs on the gripped

edges serve as major deformation mode after yield. With particles CNT films are generally stiffer before reaching 20% elongation. Once passing the small strain stage, their much heavier mass makes most particles unable to follow the motion of CNTs and thus fail to maintain entanglement in elongated regions. The stagnation of particles in the center part of such films, however, still hinders CNT's motion. A severe separation on two sides is inevitable, which leads to early stage failure at 50% strain. At 200% strain, it breaks into three parts. As the stress drops rapidly, the mechanical enhancement is entirely reversed in contrast with small strain state. Nevertheless, such failure is strain rate and species dependent. Lighter particles are expected to follow the motion of CNTs under much smaller rate. Smaller strain rate may be imposed but is computationally expensive in with the current coarse grained model. A new contact model with larger scale and new NP species can be developed as future direction of study.

On the other hand, pristine film behaves in a completely different manner. It undergoes a consistent shrinkage in the center part, where CNTs are aligned in tensile direction (Figure 5-15b). Such alignment leads to bundle-like behavior and maintain certain amount of load transfer, even though vdW adhesion is weak. Necking developed at 20% continues and eventually leads to drop of stress at 150%. At 200% strain, there is no complete separation although necking is significant at the center part. The large strain tensile tests indicate particles strengthen CNT networks at small strain range (mostly in elastic regime), while their inertia nature determines such enhancement is not consistent

throughout the film under larger strain. Toughness reduces from 1.1 GJ/m^3 to 0.61 GJ/m^3. One could thus compromise the toughness and stiffness of a CNT film based on the concentration or mass of deposited nanoparticles.

Table 5-4 Summary of uniaxial tensile tests of pristine and hybrid networks. Young's Modulus and percentage of CNTs in tension are measured at 2% strain before yield; Lateral shrinkage (i.e. necking) is measured at 20% strain.

Size	Number of NPs	Young's Modulus (GPa)	CNTs in Tension (%)	Lateral Shrinkage (%)
Medium	Pristine	9.9	61.8%	11.7%-15%
	2000	12.0	70.1%	3.4%
	4000	14.4	75.8%	1.4%
Large	Pristine	8.3	56.6%	13.7%-23.5%
	5000	13.5	79.7%	3.5%
	10000	15.0	84%	1.6%

Table 5-4 summarizes all tensile tests on medium and large size networks. With deposition of Si NPs, alignment can be effectively prevented and the film maintains its network topology. On the other hand, pristine CNT films suffer non-uniform shrinkage under tensile force. Besides the structure, particles can also significantly improve the load transfer ability and thus provide larger Young's Moduli.

5.6. Cyclic Loading Condition

CNT networks are not perfect elastic materials due to temperature and frequency dependent energy dissipation. [141] Inter tube entanglement, zipping-unzipping process [55, 56] and pulling out tubes [43] under external loading promote such dissipation process. In MDEM, the feature of energy dissipation [146] is captured by a Voigt model built in the

vdW contact model, containing a linear spring and dashpot connected in parallel. Effective dissipative forces are added on to the explicit laws shown in Table 2-3. The dashpot dictates a linear relation between dissipative forces and the relative normal or shear velocities:

$$F_n^v = c_n v_n \text{ and } F_s^v = c_s v_s. \quad (33)$$

Viscosity coefficients c_n and c_s are defined as:

$$c_n = 2\psi\sqrt{mk_n} \text{ and } c_s = 2\psi\sqrt{mk_s}, \quad (34)$$

where m is the mass of each element, k_n and k_s are stiffnesses of the contact model, chosen as 100 eV/nm^2 for both. The damping ratio ψ is calibrated through a top-down approach to reproduce the experimental measurements. [43, 68] Tensile tests on CNT ropes from previous work [68] have demonstrated a damping ratio of 0.03 as approximation.

Energy dissipation is evaluated through cyclic loading condition. In a compression-tension cycle, compressive strain of 1% is reached and tensile strain is then applied to restore the network to original shape. The strain rate is set as an average value in a half cycle with the consideration of acceleration and deceleration period. The first study focuses on energy dissipation of pristine networks (medium size) under different strain rate conditions. Dissipation and stability are evaluated from six loading-unloading cycles with various strain rates: $1.32\times10^{-7}/fs$, $7.97\times10^{-8}/fs$ and $3.63\times10^{-8}/fs$.

The second study investigates on the role of particles in energy dissipation. The strain rate is set as $5.7\times10^{-8}/fs$ for both compression and tension. Dissipation is evaluated from the net toughness (area under strain-stress curves considering the sign of strain/stress) encircled by each loading-unloading loop and Young's Moduli are calculated from tensile session in three cycles.

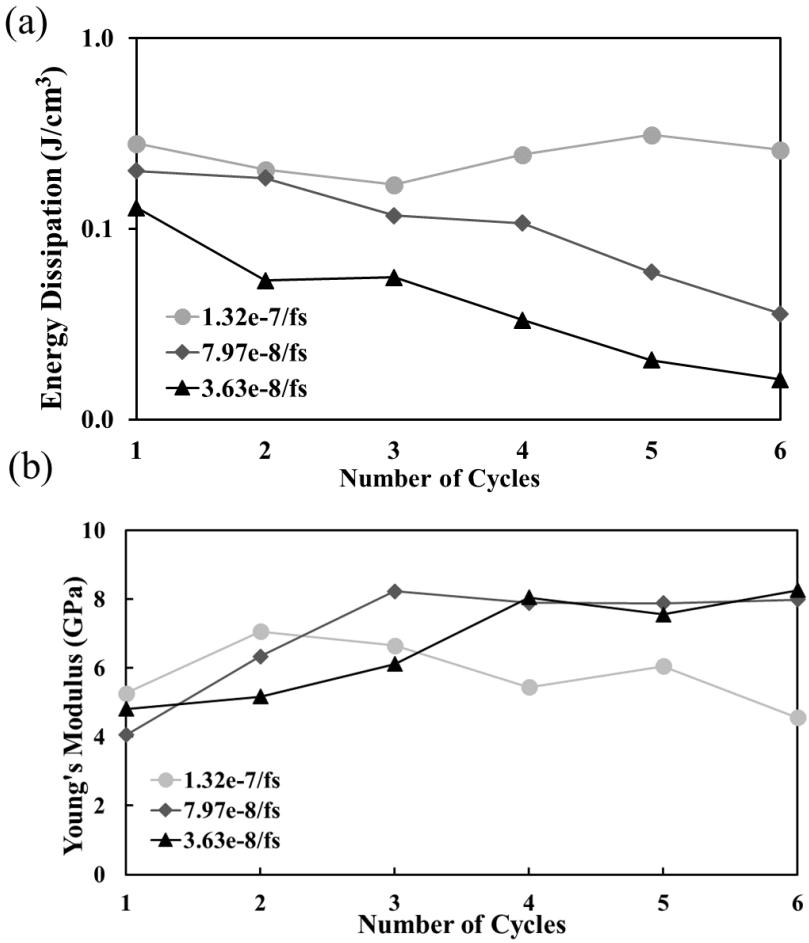

Figure 5-16 (a) Energy dissipation and (b) Young's Modulus measured in each loading-unloading cycle with different strain rates.

Same to the tensile tests before, stress is calculated as a cumulative response of

forces on the gripped elements normalized by the cross-sectional area of the thin film. As expected, higher strain rate leads to severe sliding and larger energy dissipation (Figure 5-16a). Large strain rate also promotes instability. It is noted that after six cycles, the energy dissipation drops one order of magnitude in low strain rate state. The energy dissipation of 0.1 J/cm^3 matches existing coarse grained MD data [142] very well. As can be seen in Figure 5-16b, under moderate strain rate, the network topology becomes stable against fatigue as Young's Modulus (measured in strain range from -0.7% to -0.2%) becomes convergent and approaching the value in Table 5-4. In terms of time domain, strain rates have little impact on the phase difference between stress and strain. It is found stress leads strain by approximately 0.3 period in all three cases.

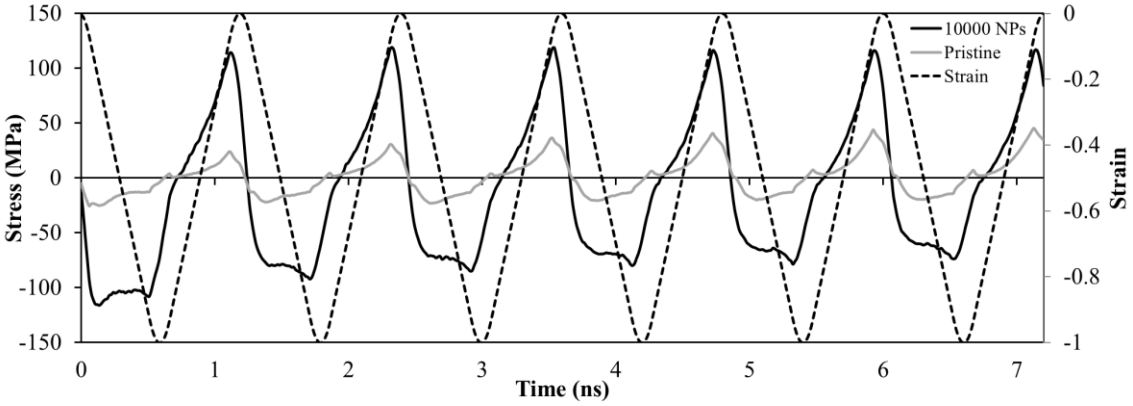

Figure 5-17 Stress measured under cyclic loading condition for pristine and hybrid network with the reference of applied cyclic strain.

The phase shift between stress and strain in pristine network indicates the load propagation and transfer ability. As shown in Figure 5-17, in the compression region of pristine network, stress does not follow strain from 0% to -1%, while the peak of tensile

region almost overlaps with strain. Such different responses of compress and tension are due to “local effects”. When compressed, instead of sliding, CNTs on edges will also reorient or even bend, which divert load transfer towards the center. In hybrid network, stress leads strain by 0.1 period in both tension and compression region, meaning load transfer is equally effective in both regions. In addition, with NPs as confinement, negative local effects such as reorientation and bending are limited.

Table 5-5 Young’s Modulus (unit: GPa) measured in cyclic loading tests for pristine and hybrid CNT networks; 95% Confidence Interval is an estimation based on assumption of normal distribution.

Number of Cycles	Pristine	5000 NPs	10000 NPs
1	2.25	14	18.1
2	2.75	14.3	18.6
3	3.32	14.5	18.3
4	3.91	14.1	18.3
5	4.3	14.4	18
6	5.1	14	18.5
95% Confidence Interval	N/A	(14.1,14.4)	(18.1,18.5)

In Table 5-5, variant Young’s Moduli of pristine network measured in tensile region further confirm the poor load transfer. In pristine networks, after compression, tensile strain will restore CNTs on edges to their initial orientation, which gives relatively small stress response. Young’s Moduli measured in pre-compressed network are much smaller than direct measurement with tensile tests (Table 5-4). Meanwhile, hybrid networks provide a consistent response in terms of a narrow range of moduli measured in 6 cycles. Tensile loads gradually propagate from the edges to the center (Figure 5-11) without local effects. It is expected that hybrid network may have better resistance to

fatigue loading conditions.

There are limitations for these preliminary studies. A simple Voight model may not be accurate to capture the non-linear energy dissipation in CNT sliding and the number of cycles is insufficient to directly access the fatigue behavior. Future works should address these issues in order to provide a comprehensive understanding of CNT network behavior under high frequency cyclic loading conditions.

5.7. Concluding Remarks

MDEM is successfully adapted in modeling complex CNT networks to understand the time dependent structural evolution via relaxation. Van der Waals attractive forces drive bundling effect and larger pores opening and eventually impact on mechanical behaviors. Embedded Si nanoparticles have the ability to interfere the bundling effect by extended volume forces.

Uniaxial tensile tests are implemented to access the mechanical response under various loading states. At small loading state, poor load transfer in pristine network leads to severe sliding and yield at 3% strain. The presence of nanoparticles effectively transfers the load through pores. Instead of sliding, individual CNTs convey stretching loads and thus Young's Modulus is enhanced by at least 80%. At 20% deformation, necking in pristine CNT network becomes severe due to alignment of CNTs under large external loading. Hybrid network has negligible shrinkage in lateral direction and yet

pulling out tubes on edges is also evident. At large deformation (>100%), necking continues through massive alignment but also maintains a mild level of load transfer. In hybrid network, particles hinder the motion of tubes in the center and are directly responsible for early failure.

With an introduction of viscous damping model, energy dissipation is found between loading-unloading cycles based on strain rates. Massive sliding in pristine network gives smaller Young's Modulus than static loading conditions, while hybrid networks have ability to resist such fatigue.

From experimental point of view, incorporation of NPs into CNT materials can be achieved using several possible approaches, including in situ synthesis [147, 148] and two-step processes such as an initial assembly of the nanotube network followed by the subsequent deposition of the NP phase on top of the SWCNTs. Some potential deposition routes include vacuum filtration, [149] direct deposition of the NPs from a gas phase immediately following their synthesis, [150] or Langmuir-Blodgett-type approaches that exploit the formation of a NP monolayer on the surface of an immiscible fluid, such as water. [151] The precise choice of the deposition scheme will be dictated by the nature of the NPs, such as solubility and surface treatment. Each approach will likely yield variations in the precise morphology of the hybrid.

In general, optimizing the properties of interest of these hybrids implies exploring

a large parameter space. Since an exhaustive experimental study of how nanoparticle size, composition (metallic vs. semiconducting) and surface chemistry act in concert to impact targeted properties (modulus, conductivity, durability) is prohibitive, the MDEM method opens the possibility the processing of stable SWCNT systems, including aerogels. [125, 152] NP-SWCNT vdW contact models can be developed in the same manner as here. Additionally, it is anticipated that the MDEM can be coupled with graph theory approaches [153] to identify and characterize probable conduction pathways in the SWCNT network and thus to predict the electric transport of the network.

Chapter 6 Mechanics of Nanocystalline Particles[8]

6.1. Introduction

The general mechanical behavior of nanoscale materials is of great interest for engineering applications such as new ultrastrong structural materials, microelectronics, and micro- and nano-electromechanical devices and systems. After exploring the role of Si nanoparticles in CNT network, we are extending the modeling work in hierarchically structured nanocrystalline hollow Au and CdS (Cadmium Sulfide) nanospheres [154-156]. For example, the Au nanospheres are about 100 nm in diameter, and feature a nanocrystalline shell with a thickness ranging from 20 to 50 nm, and grain size around 10 nm. Such combination provides an interesting opportunity to explore the effects of structural hierarchy on the global deformation mechanisms. The failure mechanisms of Au and CdS nanocrystalline agglomerates have been studied by direct indentation tests [155] showing both plastic and brittle behavior, respectively. Unfortunately, modeling and simulation fall behind experimentation. Various numerical modeling approaches, such as finite element [155] and molecular dynamics (MD) [157, 158], have been implemented to facilitate the understanding of the mechanical behavior in nanoscale systems. However, continuum approaches fail to provide information on the fracture mechanisms of discrete

[8] This chapter presents the preliminary work done in collaboration with Dr. Igor Ostanin from Skolkovo Institute of Science and Technology, Mosco, Russia. The work has been published in *Journal of Engineering Materials and Technology* (DOI: 10.1115/1.4029249, 2015).

granular systems. Despite the success of MD simulations in modeling of nanoparticles up to 40 nm in diameter [157, 158], the direct modeling of larger systems remains challenging due to size and time-scale related computational limitations. Hybrid multiscale approaches, such as quasicontinuum [159, 160] and two-scale models [161, 162], are more suitable for the mechanical modeling of failure processes of such systems. In this chapter, MDEM is implemented as an alternative numerical tool for modeling mechanics of nanoscale crystalline agglomerates. In geomechanics and civil engineering communities, the problems involving mechanics of granular discontinuous media are often addressed with the MDEM, a well-established numerical technique based on the idea of representation of the media as a collection of particles. In the most general formulation [62], MDEM calculates the dynamics of deformable complex-shaped polygonal blocks. However, most applications adopt the simplification of representing the granular media as a collection of rigid spherical particles. [67] Through validation and application demonstrated in large-scale assemblies of carbon nanotubes, MDEM reflects genuine mechanics from molecular to the mesoscopic level.

The objective of this work is to further explore the applicability of the MDEM concept to efficiently simulate the mechanics of nanocrystalline particles. Therefore, to investigate multiple length scales, such as grain size, shell thickness, and diameter of sphere within an individual structure, the nanocrystalline agglomerate is represented as an assembly of spherical particles, where each element represents a monocrystalline block of

material. These particles interact according to specific force–displacement laws, prescribed by contact models that are parameterized here to fit experimental behavior. The framework outlined above appears justified by both MD simulations and experiments that indicated that nanocrystalline materials exhibit failure mechanisms dominated by intergranular, rather than intragranular processes [161, 162].

Chapter 6 is organized as following: Section 2 introduces the key components of the DEM model for nanocrystalline agglomerates and describes the contact models that are used in our exploratory simulations. Section 3 gives an overview of our numerical simulations and provides the qualitative comparison with available experiments, along with discussion of the most notable features of experimental and numerical results.

6.2. MDEM Representation of Nanocystalline Particle

MDEM implementation uses the PFC code, which computes the damped dynamics of a collection of interacting spherical particles with uniformly distributed mass m and scalar moment of inertia ($2/5mR^2$), where R is the radius of a particle. Infinitely rigid walls, imposing forces and moments on particles based on prescribed contact models, can also be introduced. These walls can be either static or moving with the prescribed motion law. The translational and rotational motion of a rigid particle is given by the following equations:

$$\boldsymbol{F} = m\dot{\boldsymbol{v}},\ \boldsymbol{M} = \frac{2}{5}mR^2\dot{\boldsymbol{\omega}}, \tag{35}$$

where $\boldsymbol{F}$ and $\boldsymbol{M}$ are total force and moment acting on a particle, $\boldsymbol{v}$ and $\boldsymbol{\omega}$ are translational and angular velocities.

Eq. 36 is solved with explicit velocity Verlet finite difference algorithm (see detailed information in Chapter 2). The time step is dynamically adjusted to ensure stability. An artificial dissipative damping (for both force and moment equations), described by a local damping parameter α, is introduced for stabilizing the assemblies of moving particles under external load. The magnitude of each component of the damping force and moment is proportional to the corresponding component of the resultant force and moment, and they act in a direction to oppose the corresponding velocity and angular velocity. In our simulations, we used $\alpha = 0.7$. The viscous damping, setup as described in Ref. [67], with the damping ratio $\beta = 0.5$ is used in the course of mechanical test for the purposes of energy dissipation during failure.

The deformation mechanism is accessed through compression test simulations on hollow spherical assembly, but the framework can be straightforwardly generalized onto more complex shapes and loading conditions. To create the initial equilibrated configuration of distinct elements, we use the procedure illustrated with Fig. 6-1a. At the first step, distinct elements are uniformly distributed over volume of a spherical shell with outer and inner radii R_1^p and R_2^p. The radii of distinct elements r_i are uniformly

distributed in a range (r_1, r_2). Then, two spherical walls are created with radii R_1^p and R_2^p. Linear frictionless contact model (described in the Section 3) is prescribed between walls and distinct elements. At the next step, the system is equilibrated, forming stochastic closely packed configuration that models the structure of monocrystalline grains within the agglomerate. Finally, the repulsive linear forces that correspond to equilibrated configuration are set to zero, bonding contact models, described in Section 3 are installed at interfaces, and walls are eliminated.

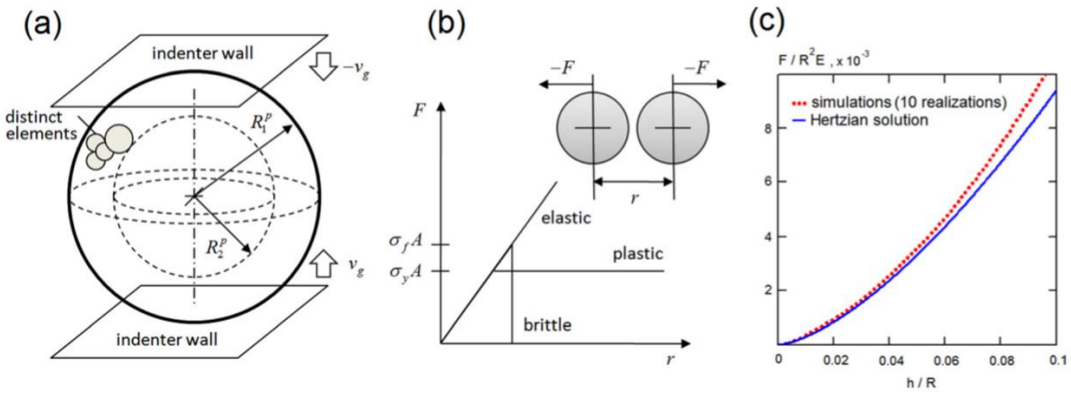

Figure 6-1 (a) Schematic representation of indentation test setup. (b) Force–displacement curves of elastic, plastic, and brittle bond contact models for a simple normal tension test. (c) Elastic response of a spherical nanoparticle averaged over 10 realizations, as compared to an analytical (Hertzian) solution.

The mechanical test is setup in the following way: the nanoparticle is positioned between two flat walls (Fig. 6-1a). The linear frictionless contact model is prescribed between balls and walls. At the initial moment of the test, walls start to move one toward another with fixed velocity, providing constant-rate displacement controlled loading. After reaching maximum strain, the indenter walls are pulled back to their initial positions with the same velocity.

6.3. Contact Models in Nanoparticle Assemblies

By dictating the forces and moments that act in equal and opposite sense on interacting distinct elements, contact models define the constitutive mechanical behavior at the elements' contacts. The contact laws are formulated in terms of generalized coordinates describing mutual position of two interacting entities and generalized forces associated with these coordinates. In experiment, three types of behavior of nanoparticles have been observed, namely, linear elastic deformations, plastic yield, and brittle failure [155]. Different contact models are next proposed to capture qualitatively these types of mechanical behavior.

The linear contact model, first introduced in Ref. [62], is used to describe the linear elasticity of compressed grains. In case of absence of friction and viscous dissipation, the linear model is reduced to simple linear proportionality between the overlap of two interacting entities un and the normal repulsive force F_n:

$$F_n = k_n u_n,\ k_n = \frac{\pi (R^l)^2 E}{L^l}, u_n = R_1 + R_2 - r,$$
$$L^l = R_1 + R_2,\ R^l = \min(R_1, R_2),\ \frac{1}{E} = \frac{1}{E_1} + \frac{1}{E_2}. \quad (36)$$

In the above equations, r is center-center distance between distinct elements (in case of ball-wall interaction, distance from the center of an element to the wall plane); E_1 and E_2 are Young's moduli of two interacting entities; R_1 and R_2 are their radii (flat walls are assumed to have infinite curvature radius). Linear interactions are installed between

the distinct elements, and between the distinct elements and the indenter walls.

Parallel bond is the simplest bonding model, representing the behavior of elastic material with Young's modulus *E* and shear modulus *G*, filling the cylindrical neck region with radius $R^b = \min(R_1, R_2)$and length $L_b = r$ between two bonded elements. Similar to parallel bond in CNT system, it provides an interface of distributed springs, resisting to stretching, shearing, bending, and torsional deformations, according to the incremental laws:

$$\begin{aligned} \Delta x = -k_n^b A^b \Delta F_n,\ \Delta y = -k_s^b A^b \Delta F_s, \\ \Delta\theta = -k_n^b I^b \Delta M_n,\ \Delta\varphi = -k_s^b J^b \Delta M_s, \end{aligned} \tag{37}$$

where A^b, I^b, and J^b are area, moment of inertia, and polar moment of inertia of a cylindrical cross section:

$$A^b = \pi(R^b)^2,\ I^b = \frac{\pi}{4}(R^b)^4,\ J^b = 2I^b. \tag{38}$$

$k_n^b = E/L^b$ and $k_s^b = G/L^b$- distributed normal and shear stiffnesses of a bond contact; variables $\Delta x, \Delta y, \Delta\theta, \Delta\varphi$ denote increments of normal and shear displacement components, and bending and twisting angles; ΔF_n, ΔF_s, ΔM_n, ΔM_s are increments of projections of normal and shear forces, and of bending and twisting moments.

Plastic bond contact model is a generalized through existing parallel bond model to describe plastic deformations of bonds. The model represents elastic-perfectly plastic behavior of the neck region between two bonded grains with Tresca (maximum shear

stress [163]) criterion of plasticity. Considering that the elastic energy of a bonded particle specimen is dominated by normal and shear components, with bending and twisting components negligible, we do not include the partial plastic yield of the neck under bending and twisting. Plasticity under tension/compression and shear is implemented as an additional condition to incremental scheme in Eq. 38: if the normal or shear force exceeds the value corresponding to tensile strength limit σ_y or shear strength limit $\tau_y = \sigma_y/2$, then normal and shear forces are stop incrementing. Instead, corresponding force is multiplied by the factor $1 - |\Delta F_n|$ (or $1 - |\Delta F_s|$), to ensure elastic behavior on the next time step. Such simple implementation has certain drawbacks, e.g., it allows interpenetration (and densification) of the material in certain loading situations. However, it can serve as a starting point in considering plastic deformation of bonded assemblies.

The fourth contact model involved is finite strength bond. Plastic contact bonds are relevant for modeling Au nanoparticles that exhibit significant plastic yield. However, some other types of nanoparticles (e.g., CdS nanoparticles) perform brittle cleavage. In order to model this kind of behavior, we introduce finite strength of bonds that are broken when tensile σ_f or shear limit $\tau_f = \sigma_f/2$ is reached. Our bond breakage model is inspired from the one used in bonded particle model for rock [164]. There are two major differences between the model [164] and our model, namely: (1) the Tresca (and not Mohr–Coulomb) criterion of failure and (2) the absence of linear interactions between bonded elements, which are introduced in bonded particle model for rock to reflect fundamental asymmetry

between tensile and compressive stiffness of a rock specimen, conditioned by the presence of voids and microcracks. In our model, linear frictionless interactions are introduced only between unbonded elements. Our simulations employ a contact model that incorporates the features described in the following section. It prescribes linear frictionless interactions in case of absent or broken bonds between distinct elements as well as in case of element–wall interactions. The elastic bonds prescribed between elements break in either brittle or ductile way, whichever critical stress— σ_f or σ_y (τ_f or τ_y) occurs first (Fig. 6-1b).

6.4. Elasticity and Plasticity of Au Nanoparticles

We first study the elastic-plastic deformation of Au nanoparticles. If the contact forces between bonded particles do not exceed failure limits, bonded assembly of particles deforms elastically (rate dependent viscosity associated with local and viscous damping is negligible in our simulations). In this scenario, the elasticity of parallel bonds that are formed between neighboring grains represents the mechanics of elastic continuum. Since the behavior of an elastic shell under axial loading is complex [165], we consider a case of infinitesimal loading of a spherical particle ($R_1^p = 0$) to calibrate the elastic properties of an aggregate. For this particular case, the Hertz analytical solution is available [166]. For the particle with radius $R = R_2^p$, Young's modulus E, and Poisson's ratio v, it can be given in the following dimensionless form linking compression force F

and sphere axial contraction h:

$$\frac{F}{R^2E} = \frac{1}{3\sqrt{2}(1-\nu^2)}\left(\frac{h}{R}\right)^{\frac{3}{2}}. \quad (39)$$

We have performed simulations of compression test on 10 independent realizations of a spherical aggregate with R = 50 nm, porosity of 40%, grain size varying between 1 and 2 nm, and the density ρ of the particles and elastic parameters of parallel bonds corresponding to those of bulk Au (ρ = 19.3 cm^3, E = 79 GPa, and ν = 0.46). It follows that the elastic behavior is consistent with an analytical solution (Fig. 6-1c). The porosity of the assembly (volume fraction of voids with respect to the shell) affects effective elastic moduli of the shell as well as its total mass. Nevertheless, the selected porosity of 40% gives a behavior consistent with the deformation of a corresponding continuous sphere. Thus, the porosity of initial particle deposition and the density of the particles can be fit to match the overall elastic and inertial properties of the shell.

It is well known from experiment that metallic nanocrystalline particles exhibit irreversible plastic failure in mechanical tests [167]. To reproduce this behavior, plastic bond contact model is activated. It is envisaged that the strength and plasticity observed in the mechanical experiments carried out on these Au nanostructures could be well match by a proper selection of yield strength, σ_y. Therefore, we have performed a series of compression tests on an Au nanoparticle with parameters R_1^p =52 nm and R_2^p =95 nm, with grain sizes varying from 3 nm to 6 nm, and few different values of plastic limit

$\sigma_y = 2\tau_y$. Figure 6-2a illustrates the comparison of force–displacement curves obtained in simulations for the different values of σ_y. It is noted that the values σ_y used in this study are within the range of strength observed in Au nanostructures [168].

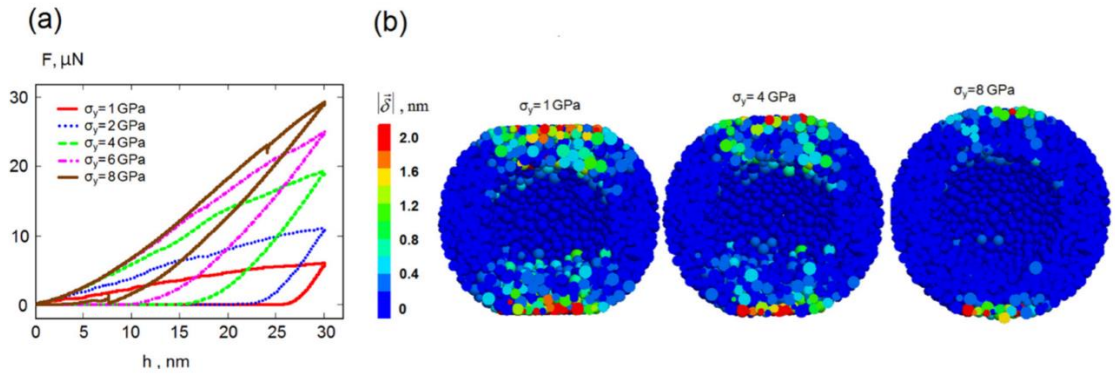

Figure 6-2 (a) DEM stress–strain curves and (b) slip vector diagrams obtained in indentation tests of Au nanoparticle for different values of yield strength σ_y.

The results of simulation qualitatively agree with the results of direct compression tests on Au nanocrystalline particles [167]. The peak value of the curve based on σ_y = 8 GPa appears to best match the experimental strength [167]. Diagrams in Fig. 6-2b present the distribution of a plastic flow in a final state with residual displacements. The relative sliding of the elements during the compressive load is captured by a color code, which is defined as the magnitude of the slip vector [68]:

$$|\delta| = \frac{1}{\lambda_i}\sum_j^{\lambda_i}\left|x^{ij} - X^{ij}\right|. \quad (40)$$

Here, x^{ij} and X^{ij} are the vector differences between the coordinates of elements i and j in the current state and the initial reference state, respectively. λ_i is the number of

nearest neighbors to element i in the initial reference state. It can be observed that the plastic deformation, evident also on the decompression curves of Fig. 6-2b, is localized at the contact regions and has strong dependence on yield strength, σ_y.

6.5. Brittle failure of CdS Nanoparticles

Unlike Au nanoparticle, CdS nanoparticle fails in brittle fracture, which is captured by finite strength bond contact model introduced in previous section. To illustrate the capability of our method to model brittle failure of nanocrystalline agglomerates, we perform a direct modeling of compression test on the CdS nanoparticle described in Ref. [155]. The radii of the particle R_1^p = 75 nm; R_1^p = 105 nm, Young's modulus and Poisson's ratio of CdS are set to be E = 28 GPa and ν = 0.46 [155, 169], the failure strength $\sigma_y = 2\tau_y = 4$ GPa.

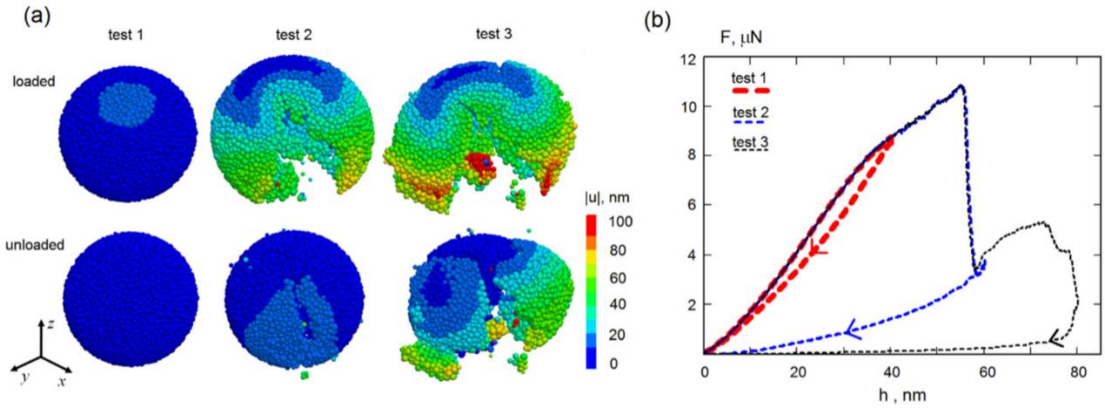

Figure 6-3 Brittle failure of a hollow CdS nanoparticle in indentation tests. Three DEM simulations were carried out: h = 40nm (test 1), h = 60nm (test 2), and h = 80nm (test 3). (a) Geometry of the particle. Color map gives magnitude of displacement. (b) Force–displacement curves of all three tests.

The test was performed for three different peak displacement levels: h = 40 nm

(test 1), h = 60 nm (test 2), and h = 80 nm (test 3). Simulation results are shown in Figure 6-3. In the first test, only isolated events of bond breakage were observed; overall deformation remained nearly elastic with full scale of recovery. In the second test, the specimen has developed a single "meridian" crack that reduced effective stiffness of a particle 3.5 times. However, the response of a damaged structure remained elastic, and upon unloading the damage was healed with closure of the crack. This behavior has involved with artifacts, since in real CdS nanoparticles the brittle failure is accompanied with significant plastic deformation. In the third test, the particle has been cleaved onto separate fragments. It is noted that the failure mechanisms observed in this test, as well as some important details, including peak force and critical strain, are consistent with the results of the nanoindentation tests [155].

6.6. Concluding Remarks

This chapter, as an extending work of MDEM framework successfully used in a context of carbon nanotubes, presents significant potential for modeling the mechanics of nanocrystalline particles and structures. The conventional DEM method presents limitations for describing the deformation of polycrystalline materials composed of large grains with high dislocation storing capacities and high defect mobility. The MDEM strategy outlined here shows promise for simulating deformations in nanocrystalline materials, where intergranular processes dominate the global plastic failure. The proof of

concept presented here is relying heavily on experimental input. The preliminary results from simulations illustrate that MDEM is capable of predicting elasticity, plasticity, and fracture processes occurring in compressed Au and CdS nanoparticles that compare well with the experimental observations. Atomistic-scale MD simulations have provided unprecedented insight into the structural and mechanical properties of nanocrystalline materials [170]. However, simulation times and system size constraints limit the predictive capabilities of this approach. To establish a connection with the mechanical-testing experiments, a multiscale simulation methodology is needed. We envisage that MDEM could serve this purpose, provided that one can successfully train the linear, parallel, plastic, and brittle contacts to reproduce results of atomistic-scale simulations. For example, a more realistic MDEM representation of the grain boundary network appears possible by building specific contact models to represent low angle grain boundaries and other types of important boundaries [161, 170] and also to account for the particle orientation. Used in a multiscale manner, MDEM will allow for "hand off" simulations based on MD data. Neither complex global constitutive models nor assumptions regarding the location and type of failure will be a priori imposed to predict the mechanical response.

Finally, it is noted that each simulation presented here lasted less than an hour on a regular personal computer. Such computational efficiency will greatly facilitate the exploration of the length scales and structural hierarchy on the mechanical response of hollow nanocrystalline particles.

Chapter 7 Conclusions and Future Research Directions

7.1. Conclusions

The major focus of this thesis is to apply recently developed computational model, MDEM, in studying complex CNT nanomaterials and related structures. In Chapter 3, MDEM facilitates the understanding of self-assembled CNT structures formation, namely, rings and rackets. In comparison against both theory and experimental measurement, MDEM simulations successfully predict the most stable configurations and evaluate the mechanical energy storage for energy reservoir applications.

Chapter 4 establishes a theory of twisted CNT fibers. Composed by hexagonal closed packed single tubes, a CNT fiber behaves in a variety of manners based on both aspect ratio and loading condition. Small aspect ratio and large torsional moment leads to formation of Bird Cage, a hollow spindle. The theory of geometric frustration explains such behavior. The twisted system lowers the energy through development of topological defects, vacancies generated inside the fiber. Larger aspect ratio will lead to stable spindle, which can be transformed into helix when the torsional loading is beyond a critical value. The helix transformation also corresponds to an energy transferred from twist to bending.

As a major part of this thesis, Chapter 5 explores the topology and mechanics of CNT network with a second phase of nanoparticles. CNT network is well known for its

application in flexible electronic devices, but its nature of bundling due to vdW attraction will deteriorate its stability as well as electrical conductivity. Through excluded volume repulsion, nanoparticles deposited in pores of the network can effectively prevent bundling and thus enhance the stability. After development of Si NP-CNT contact model, stability of pristine and hybrid networks is evaluated by tracking the bundling effect during the relaxation process. Mechanical properties are then accessed through tensile tests. MDEM simulations provide detailed information about stability and mechanics. As many CNTs fail to align, bundling is effectively reduced in hybrid network. Tensile tests also indicate a great improvement of load transfer, which further increase the Young's Modulus. In large deformation regime (up to 20% strain), a delayed yield and uniform deformation are observed in hybrid network. In contrast, in pristine network, a neck develops and big pores are opening. As expected, the increase of Young's Modulus (stiffness) will sacrifice the overall toughness. Pristine network fails at 200% strain compared to 80% for hybrid network.

Chapter 6 explores the MDEM potential for modeling the mechanics of nanocrystalline particles. Different contact models are implemented to capture the plasticity of Au nanoparticle and the brittle failure of CdS nanoparticles. This proof of concept work demonstrates the flexibility of MDEM when adapted to various granular nanomaterials systems.

7.2. Future Research Directions

Current work has already showcased the accuracy and effectiveness of MDEM in solving nanomechanical problems. Nevertheless, there is still more work for the future.

From the model development point view, current MDEM is based on only one species of defect free CNTs, namely, single-walled (10,10) CNT. The application may require, however, multi-walled CNT with various chiralities. Second, in our recent collaboration with NASA, the flexible CNT network is composed of squeezed tubes with large diameter [103, 171, 172] . Third, CNT systems are also modified through crosslinks [173-175] and functionalized by esterification or amidization [176, 177]. To include these features, one could develop a new parallel bond contact model with calibrated spring constants input from MD. The chemical group may influence the adhesion and friction when CNTs are sliding. Alternatively, a complete description of viscous damping will be the key to capture the phenomena. Fourth, besides CNT systems, it is envisioned that MDEM can also be applied to general fibrous materials. There is already strong evidence from both theory and experiments that CNT fibers assemble the behavior of protein fibers [178-180], especially in self-assembling process driven by vdW attraction. It is therefore possible to expand the model to explore the mechanism of protein folding.

From the application point of view, there is also much work to be done. CNT network with nanoparticles, described in Chapter 5, is expected to be further investigated

in more details. In addition to tensile tests, bending also provides insightful information on load transfer and stiffness. From modeling aspect, despite intensive work in individual CNT bending and buckling deformation, bending of CNT network in bulk remains unexplored.

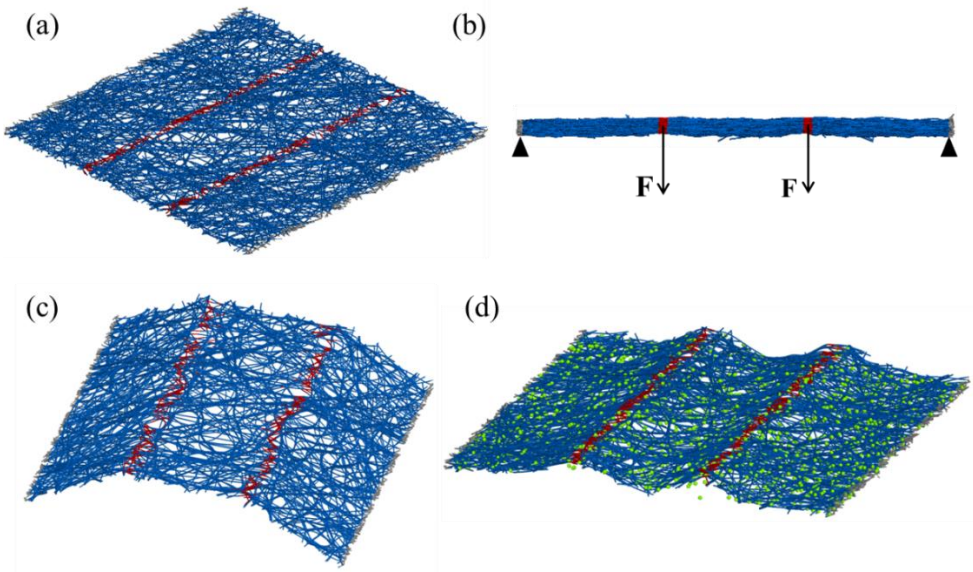

Figure 7-1 CNT Network configuration prepared for bending tests: (a) iso-view and (b) side-view. Loading slices are shown in red and gripped ends are shown in gray. (c) Bent pristine film shows flat center part. (d) Bent hybrid film shows curvy center part.

Four-point bending test is implemented in quasi-2D network by exerting out-of-plane loads on two slices of elements locating at one third the network dimension. The slice is chosen as 15 nm in width, same as the width of ending gripped elements whose motion is fixed in out of plane direction. The motion of the loading slices is controlled (Fig. 7-1a) by applying constant velocities. The responsive forces in return are measured as unbalanced forces collected from the slices. Since such testing configuration is clearly an implementation originated from continuum mechanics, on quantitative level,

it will provide evaluation on modeling porous materials.

As a proof of concept, bending tests are performed on pristine and hybrid network to investigate the deformation mechanism. During the bending, with significant out-of-plane motion, some particles are left behind due to their heavy inertial effect (One Si NP has mass about 40 times to one CNT distinct element). The remaining particles still provide large inertia that delays the deformation at the center part. Compared to the pristine film, hybrid film has a curvy center part (Fig. 7-1d). Given long relaxation time, at later stage of the test, the center part will gradually flatten.

Assuming Euler beams model, continuum mechanics suggests a simple linear force-deflection relation:

$$F = \frac{24DEI}{a(3l^2-4a^2)}, \tag{41}$$

where F is the applied loads, D is the deflection measured at the loading points, EI together is the stiffness, a is the spacing between loading slices and the end grips and l is the dimension of entire network. The slope of F vs. D reflects stiffness of the film. Nevertheless, the preliminary data does not well support the continuum theory. As can be seen in Figure 7-2a, linear dependence of force on deflection does not manifest for entire deflection regime. Instead, the pristine curve fits better in a parabolic form (e.g. $F \sim D^2$). For hybrid network, there is a stagnation region of forces in which the center part of the network becomes wavy (Fig. 7-1d). These observations should be confirmed by

comprehensive studies. Meanwhile, the highly porous structure may vary *I* of the cross-section together with the change of stiffness during the deformation. A numerical relation between *F* and *D* should also be developed.

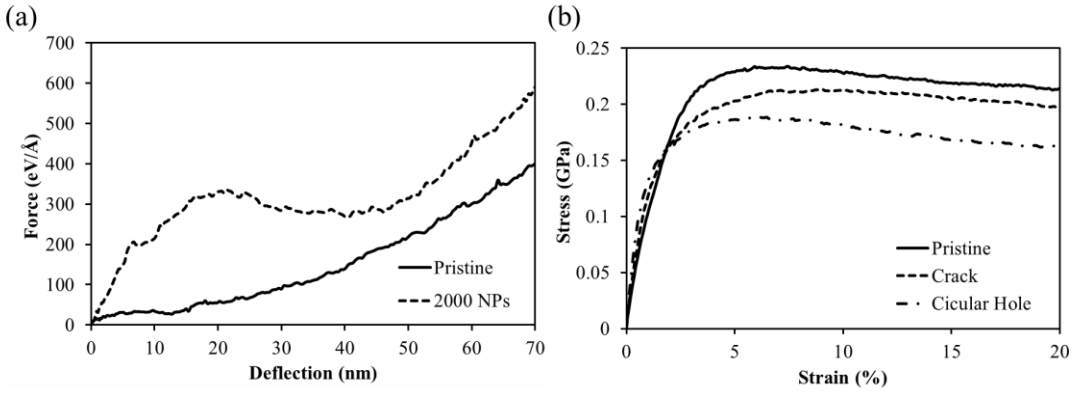

Figure 7-2 (a) Force vs. deflection curves obtained from bending tests on pristine and hybrid CNT networks. (b)Strain-stress curves of CNT networks with defects.

The other potential research direction is to investigate crack in the network system. Crack induced fracture is commonly observed to initiate materials failure. Well-developed fracture mechanics suggests an intensified stress concentrated at the crack tips when the bulk materials are under loading. Once the stress intensity is reached, crack will start to propagate and eventually leads to failure. Even within the safe loading conditions, when cyclic loading is imposed, microcrack can slowly grow after millions of cycles. However, such classic energy approach from Griffith theory [181] does not apply in fibrous materials especially when their discretized nature manifests. Biological tissue (e.g. skin), for instance, is found to resist shear force by alignment of micro fibers. [182] Since both skin and CNT thin film consist of network, they are also expected to share certain

similarities in resisting crack opening.

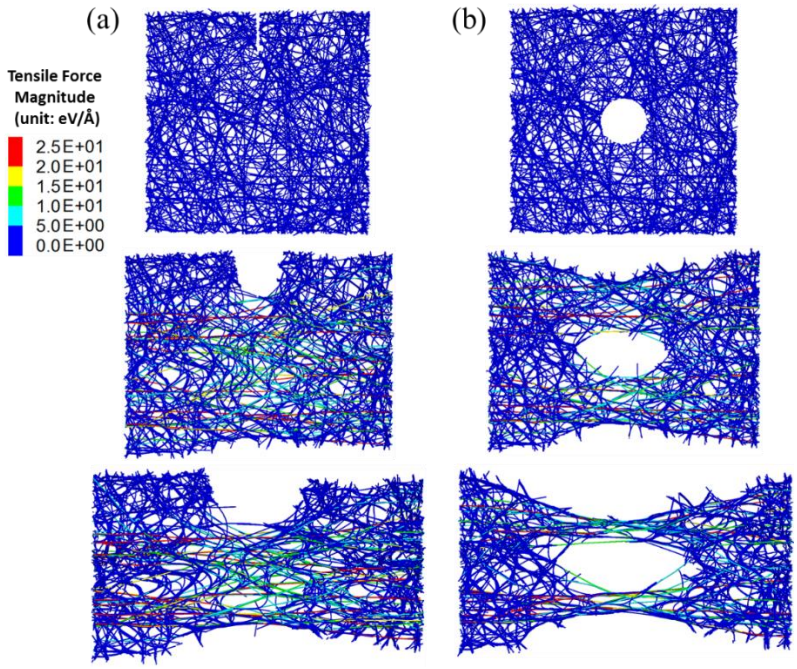

Figure 7-3 Crack development under 0%, 20% and 40% elongation strain (a) A flaw on the edge (b) A circular hole in the center

When stretching a CNT network with a crack inside, crack widening instead of opening or propagating found to be the dominating response. The cracks considered here are a flaw on the edge (100 nm in length) and a circular hole in the center (100 nm in diameter). Figure 7-3 shows the crack develops upon stretching. In both cases, there is no obvious stress concentration. As sliding is intensive, CNTs in intact region align in tensile direction and contribute to load transfer. Because sliding is the dominating factor at small strain regime, a creation of crack or circular hole will not significantly lower the Young's Modulus (Figure 7-2b), which is an indicator of load transfer. After yield, there is minor reduction of stress level due to crack. Alignment of tubes will compensate the stress

distribution and leads to high resilience regardless of crack.

Finally, much of the current work should be extended in general parametric studies. The data obtained in Chapter 5 is based on only three random network topologies. Statistical analysis will demand intensive data collection. Besides, for optimizing network's properties, a series of intrinsic factors can be examined, such as length of individual tubes, distribution and orientations. In terms of second-phase nanoparticles, species, size and concentration are key issues to dictate the mechanical properties. Besides, a percolation theory that evaluates the electrical conductivity should also be modified with the consideration of particles and bent tubes.

In summary, the development and extension of MDEM will facilitate new materials design and study. It provides insightful guidance for materials engineers to implement testing experiments as well as accelerate the industrial application in both low-cost and efficient ways.

References

1. Iijima, S., *Helical Microtubules of Graphitic Carbon.* Nature (London), 1991. **354**: p. 56.
2. Salvetat, J.-P., et al., *Mechanical properties of carbon nanotubes.* Applied Physics A, 1999. **69**: p. 255-260.
3. Yakobson, B.A., P, *Mechanical properties of carbon nanotubes.* Carbon Nanotubes, 2001. **80**: p. 287-327.
4. Bandaru, P.R., *Electrical Properties and Applications of Carbon Nanotube Structures.* Journal of Nanoscience and Nanotechnology, 2007. **7**: p. 1-29.
5. Sun, K.S., MA ; Dutta, M, *Thermal conductivity of carbon nanotubes.* Journal Of Applied Physics, 2009. **105**(7): p. 105.
6. Ebbesen, T.L., HJ ; Hiura, H ; Bennett, JW ; Ghaemi, HF ; Thio, T, *Electrical conductivity of individual carbon nanotubes.* Nature, 1996. **382**: p. 54-56.
7. Yu, M.F., et al., *Strength and breaking mechanism of multiwalled carbon nanotubes under tensile load.* Science, 2000. **287**(5453): p. 637-640.
8. Chen, H.-J.Z., Z.-H. ; Luo, L.-J. ; Yao, S.-Z., *Surface-imprinted chitosan-coated magnetic nanoparticles modified multi-walled carbon nanotubes biosensor for detection of bovine serum albumin.* Sensors and Actuators B: Chemical, 2012. **163**(1): p. 76-83.
9. Liu, Y.C.a.J., *Carbon Nanomaterials for Flexible Energy Storage.* Materials Research Letter, 2013. **1**(4): p. 175-192.
10. F A Hill, T.F.H., A J Hart and C Livermore, *storing elastic energy in carbon nanotubes.* Journal of Micromechanics and MicroengineeringEmail alert RSS feed, 2009. **19**(9).
11. Ajayan, P.M. and O.Z. Zhou, *Applications of Carbon Nanotubes.* Carbon Nanotubes, 2001. **80**: p. 391-425.
12. Chandra, B., *Synthesis and Electronic Transport in Known Chirality Single Wall Carbon Nanotubes*, in *Graduate School of Arts and Sciences*. 2009, Columbia University: New York. p. 2,8.
13. Muhammad Musaddique Ali Rafique, J.I., *Production of Carbon Nanotubes by Different Routes— A Review.* Journal of Encapsulation and Adsorption Sciences, 2011. **1**: p. 29-34.
14. Björn Hornbostel, M.H., Jirka Cech, Ursula Dettlaff, Siegmar Roth, *Arc Discharge and Laser Ablation Synthesis of Singlewalled Carbon Nanotubes.* NATO Science Series II:

Mathematics, Physics and Chemistry, 2006. **222**: p. 1-18.

15. Kumar, M. and Y. Ando, *Chemical Vapor Deposition of Carbon Nanotubes: A Review on Growth Mechanism and Mass Production.* Journal of Nanoscience and Nanotechnology, 2010. **10**: p. 3739-3758.

16. Mubarak, N.M., et al., *An overview on methods for the production of carbon nanotubes.* Journal of Industrial and Engineering Chemistry, 2014. **20**(4): p. 1186-1197.

17. Bethune, D.S., et al., *Cobalt-catalysed growth of carbon nanotubes with single-atomic-layer walls.* Nature, 1993. **363**(6430): p. 605-607.

18. Cao, C., et al., *Improving Contact Interfaces in Fully Printed Carbon Nanotube Thin-Film Transistors.* ACS Nano, 2016. **10**(5): p. 5221-5229.

19. Wang, C., et al., *Wafer-Scale Fabrication of Separated Carbon Nanotube Thin-Film Transistors for Display Applications.* Nano Letters, 2009. **9**(12): p. 4285-4291.

20. Foroughi, J., et al., *Torsional Carbon Nanotube Artificial Muscles.* Science, 2011. **334**(6055): p. 494-497.

21. De Volder, M.F.L., et al., *Carbon Nanotubes: Present and Future Commercial Applications.* Science, 2013. **339**(6119): p. 535-539.

22. Fang, C., A. Kumar, and S. Mukherjee, *Finite element analysis of single-walled carbon nanotubes based on a rod model including in-plane cross-sectional deformation.* International Journal of Solids and Structures, 2013. **50**(1): p. 49-56.

23. Kasti, N.A., *Zigzag carbon nanotubes—Molecular/structural mechanics and the finite element method.* International Journal of Solids and Structures, 2007. **44**(21): p. 6914-6929.

24. Tserpes, K.I. and P. Papanikos, *Finite element modeling of single-walled carbon nanotubes.* Composites Part B: Engineering, 2005. **36**(5): p. 468-477.

25. Zaeri, M.M., et al., *Mechanical modelling of carbon nanomaterials from nanotubes to buckypaper.* Carbon, 2010. **48**(13): p. 3916-3930.

26. Alder, B.J. and T.E. Wainwright, *Studies in Molecular Dynamics. I. General Method.* The Journal of Chemical Physics, 1959. **31**(2): p. 459-466.

27. Adcock, S.A. and J.A. McCammon, *Molecular Dynamics: Survey of Methods for Simulating the Activity of Proteins.* Chemical reviews, 2006. **106**(5): p. 1589-1615.

28. King, R. and M.J. Buehler, *Atomistic Modeling of Elasticity and Fracture of a (10,10) Single Wall Carbon Nanotube.* MRS Proceedings, 2006. **924**: p. 0924-Z05-02.

29. Talukdar, K. and A.K. Mitra, *Comparative MD simulation study on the mechanical properties of a zigzag single-walled carbon nanotube in the presence of*

Stone-Thrower-Wales defects. Composite Structures, 2010. **92**(7): p. 1701.

30. Cao, G. and X. Chen, *Buckling of single-walled carbon nanotubes upon bending: Molecular dynamics simulations and finite element method.* Physical Review B, 2006. **73**(15): p. 155435.

31. Chen-Li, Z. and S. Hui-Shen, *Self-healing in defective carbon nanotubes: a molecular dynamics study.* Journal of Physics: Condensed Matter, 2007. **19**(38): p. 386212.

32. Mehdi Eftekharia, S.M., Amir Reza Khoeic, *Effect of defects on the local shell buckling and post-buckling behavior of single and multi-walled carbon nanotubes.* Computational Materials Science, 2013. **79**: p. 736.

33. Salaway, R.N. and L.V. Zhigilei, *Molecular dynamics simulations of thermal conductivity of carbon nanotubes: Resolving the effects of computational parameters.* International Journal of Heat and Mass Transfer, 2014. **70**: p. 954-964.

34. Cao, A. and J. Qu, *Size dependent thermal conductivity of single-walled carbon nanotubes.* Journal of Applied Physics, 2012. **112**(1): p. 013503.

35. Ma, J., et al., *Thermal Transport in Single-Walled Carbon Nanotubes Under Pure Bending.* Physical Review Applied, 2015. **3**(2): p. 024014.

36. Friddle, R.W., et al., *Single functional group interactions with individual carbon nanotubes.* Nat Nano, 2007. **2**(11): p. 692-697.

37. Tersoff, J., *Empirical Interatomic Potential for Carbon, with Applications to Amorphous Carbon.* Physical Review Letter, 1988. **61**(25): p. 2879-2882.

38. Stillinger, F.H. and T.A. Weber, *Computer simulation of local order in condensed phases of silicon.* Physical Review B, 1985. **31**(8): p. 5262-5271.

39. Girifalco, L.A., M. Hodak, and R.S. Lee, *Carbon nanotubes, buckyballs, rope and a universal graphite potential.* Physical Review B, 2000. **62**(19): p. 104-110.

40. Yao, Z., et al., *Mechanical properties of carbon nanotube by molecular dynamics simulation.* Computational Materials Science, 2001. **22**(3–4): p. 180-184.

41. WenXing, B., Z. ChangChun, and C. WanZhao, *Simulation of Young's modulus of single-walled carbon nanotubes by molecular dynamics.* Physica B: Condensed Matter, 2004. **352**(1–4): p. 156-163.

42. Ozaki, T., Y. Iwasa, and T. Mitani, *Stiffness of Single-Walled Carbon Nanotubes under Large Strain.* Physical Review Letters, 2000. **84**(8): p. 1712-1715.

43. Filleter, T., et al., *Experimental-Computational Study of Shear Interactions within Double-Walled Carbon Nanotube Bundles.* Nano Letters, 2012. **12**(2): p. 732-742.

44. Kim, W., et al., *Synthesis of Ultralong and High Percentage of Semiconducting*

Single-walled Carbon Nanotubes. Nano Letters, 2002. **2**(7): p. 703-708.

45. Wang, X., et al., *Fabrication of Ultralong and Electrically Uniform Single-Walled Carbon Nanotubes on Clean Substrates.* Nano Letters, 2009. **9**(9): p. 3137-3141.

46. Huang, S., X. Cai, and J. Liu, *Growth of Millimeter-Long and Horizontally Aligned Single-Walled Carbon Nanotubes on Flat Substrates.* Journal of the American Chemical Society, 2003. **125**(19): p. 5636-5637.

47. Horstemeyer, M.F., *Multiscale Modeling: A Review*, in *Practical Aspects of Computational Chemistry: Methods, Concepts and Applications*, J. Leszczynski and M.K. Shukla, Editors. 2010, Springer Netherlands: Dordrecht. p. 87-135.

48. http://www.skf.com/uk/index.html.

49. *Multiscale simulation of thin-film lubrication: Free-energy-corrected coarse graining.* Physical Review E, 2014. **90**(3).

50. *Multi-scale coarse-graining of non-conservative interactions in molecular liquids.* The Journal of Chemical Physics, 2014. **140**(10): p. 104104.

51. *Perspective: Coarse-grained models for biomolecular systems.* The Journal of Chemical Physics, 2013. **139**(9): p. 090901.

52. Buehler, M.J., *Mesoscale modeling of mechanics of carbon nanotubes: Self-assembly, self-folding, and fracture.* Journal of Materials Research, 2006. **21**(11): p. 2855-2869.

53. Buehler, M.J., et al., *Self-Folding and Unfolding of Carbon Nanotubes.* Journal of Engineering Materials and Technology, 2005. **128**(1): p. 3-10.

54. Volkov, A.N. and L.V. Zhigilei, *Structural Stability of Carbon Nanotube Films: The Role of Bending Buckling.* ACS Nano, 2010. **4**(10): p. 6187-6195.

55. Li, Y. and M. Kroger, *Viscoelasticity of carbon nanotube buckypaper: zipping-unzipping mechanism and entanglement effects.* Soft Matter, 2012. **8**(30): p. 7822-7830.

56. Li, Y. and M. Kröger, *A theoretical evaluation of the effects of carbon nanotube entanglement and bundling on the structural and mechanical properties of buckypaper.* Carbon, 2012. **50**(5): p. 1793-1806.

57. Wang, Y., et al., *Ring windings from single-wall carbon nanotubes: A distinct element method study.* Applied Physics Letters, 2013. **103**(18): p. 183902.

58. Wang, Y., et al., *Twisting Carbon Nanotube Ropes with the Mesoscopic Distinct Element Method: Geometry, Packing, and Nanomechanics.* Langmuir, 2015. **31**(45): p. 12323-12327.

59. Wang, Y., et al., *Rings and rackets from single-wall carbon nanotubes: manifestations of mesoscale mechanics.* Soft Matter, 2014. **10**(43): p. 8635-8640.

60. Wang, Y., et al., *Excluded Volume Approach for Ultrathin Carbon Nanotube Network Stabilization: A Mesoscopic Distinct Element Method Study.* ACS Applied Materials & Interfaces, 2017. **9**(15): p. 13611-13618.

61. Ostanin, I., et al., *Mechanics of Nanocrystalline Particles With the Distinct Element Method.* Journal of Engineering Materials and Technology, 2015. **137**(2): p. 024501.

62. Cundall, P.A. and O.D.L. Strack *A discrete numerical model for granular assemblies*. Geotechnique, 1979. **29**, 47-65.

63. Ubach, P.A., et al., *Application of an enhanced discrete element method to oil and gas drilling processes.* Computational Particle Mechanics, 2016. **3**(1): p. 29-41.

64. O'Sullivan, C., *Particle-based discrete element modeling geomechanics perspective.* International Journal of Geomechanics, 2009. **11**(6): p. 449-464.

65. Ostanin, I., et al., *A distinct element method for large scale simulations of carbon nanotube assemblies.* Journal of the Mechanics and Physics of Solids, 2013. **61**(3): p. 762-782.

66. Anderson, T., et al., *Toward Distinct Element Method Simulations of Carbon Nanotube Systems.* Journal of Nanotechnology in Engineering and Medicine, 2010. **1**(4): p. 041009-041009.

67. Inc., I.C.G., *PFC 3D (Particle Flow Code in 3 Dimensions) Version 4.0*. 2008.

68. Ostanin, I., R. Ballarini, and T. Dumitrică, *Distinct Element Method Modeling of Carbon Nanotube Bundles With Intertube Sliding and Dissipation.* Journal of Applied Mechanics, 2014. **81**(6): p. 061004-061004.

69. Ahlskog, M., et al., *Ring formations from catalytically synthesized carbon nanotubes.* Chemical Physics Letters, 1999. **300**(1–2): p. 202-206.

70. Martel, R., H.R. Shea, and P. Avouris, *Ring Formation in Single-Wall Carbon Nanotubes.* The Journal of Physical Chemistry B, 1999. **103**(36): p. 7551-7556.

71. Richard, M., S. Herbert, and R.A. Phaedon, *Rings of single-walled carbon nanotubes.* Nature, 1999. **398**(6725): p. 299.

72. Wang, W., et al., *Bending single-walled carbon nanotubes into nanorings using a Pickering emulsion-based process.* Carbon, 2012. **50**(5): p. 1769-1775.

73. Chen, L., et al., *Controlling Reversible Elastic Deformation of Carbon Nanotube Rings.* Journal of the American Chemical Society, 2011. **133**(25): p. 9654-9657.

74. Chang, C., et al., *Ring formation mechanism of single-walled carbon nanotubes: Energy conservation between curvature elasticity and inter-tube adhesion.* Chemical Physics, 2012. **393**(1): p. 123-128.

75. Zheng, M. and C. Ke, *Elastic deformation of carbon-nanotube nanorings.* small, 2010. **6**(15): p. 1647-1655.

76. Markus J. Buehler, Y.K., Huajian Gao, Yonggang Huang, *Self-Folding and Unfolding of Carbon Nanotubes.* Journal of Engineering Materials and Technology, 2006. **128**: p. 3-10.

77. C.R. Chang, L.H.L., J.H. Liu, W. Chen, *Ring formation mechanism of single-walled carbon nanotubes: Energy conservation between curvature elasticity and inter-tube adhesion.* Chemical Physics Letters, 2012. **393**: p. 123-128.

78. Carlson, A. and T. Dumitrică, *Extended tight-binding potential for modelling intertube interactions in carbon nanotubes.* Nanotechnology, 2007. **18**(6): p. 065706.

79. Nikiforov, I., et al., *Wavelike Rippling in Multi-walled Carbon Nanotubes under Pure Bending.* Appl. Phys. Lett., 2010. **96**: p. 123107.

80. Thess, A., et al., *Crystalline Ropes of Metallic Carbon Nanotubes.* Science, 1996. **273**(5274): p. 483-487.

81. Hill, F., T. Havel, and C. Livermore, *Modeling mechanical energy storage in springs based on carbon nanotubes.* Nanotechnology, 2009. **20**(25): p. 255704.

82. Hill, F.A., *Mechanical Energy Storage in Carbon Nanotube Springs*, in *Mechanical Engineering*. 2011, Massachusetts Institute of Technology. p. 45-46.

83. Hill, F.A., et al., *Storing elastic energy in carbon nanotubes.* Journal of Micromechanics and Microengineering, 2009. **19**(9): p. 094015.

84. Zhang, D.-B. and T. Dumitrică, *Elasticity of ideal single-walled carbon nanotubes via symmetry-adapted tight-binding objective modeling.* Applied Physics Letters, 2008. **93**(3): p. 031919.

85. Hobbie, E.K., et al., *Empirical evaluation of attractive van der Waals potentials for type-purified single-walled carbon nanotubes.* Physical Review B, 2012. **85**(24): p. 245439.

86. Kim, Y.A., et al., *Thermal stability and structural changes of double-walled carbon nanotubes by heat treatment.* Chemical Physics Letters, 2004. **398**(1–3): p. 87-92.

87. Salvetat, J.-P., et al., *Elastic and Shear Moduli of Single-Walled Carbon Nanotube Ropes.* Physical Review Letters, 1999. **82**(5): p. 944-947.

88. Fry, D., et al., *Anisotropy of Sheared Carbon-Nanotube Suspensions.* Physical Review Letters, 2005. **95**(3): p. 038304.

89. Zhou, W., et al., *Self-folding of single- and multiwall carbon nanotubes.* Applied Physics Letters, 2007. **90**(7): p. -.

90. Lu, W. and T.-W. Chou, *Analysis of the entanglements in carbon nanotube fibers using a*

self-folded nanotube model. Journal of the Mechanics and Physics of Solids, 2011. **59**(3): p. 511-524.

91. Bohr, J. and K. Olsen, *The ancient art of laying rope.* EPL (Europhysics Letters), 2011. **93**(6): p. 60004.

92. Jiang, K., Q. Li, and S. Fan, *Nanotechnology: Spinning continuous carbon nanotube yarns.* Nature, 2002. **419**(6909): p. 801-801.

93. Ericson, L.M., et al., *Macroscopic, Neat, Single-Walled Carbon Nanotube Fibers.* Science, 2004. **305**(5689): p. 1447-1450.

94. Li, Y.-L., I.A. Kinloch, and A.H. Windle, *Direct Spinning of Carbon Nanotube Fibers from Chemical Vapor Deposition Synthesis.* Science, 2004. **304**(5668): p. 276-278.

95. Mirzaeifar, R., Z. Qin, and M.J. Buehler, *Mesoscale mechanics of twisting carbon nanotube yarns.* Nanoscale, 2015.

96. Chun, K.-Y., et al., *Hybrid carbon nanotube yarn artificial muscle inspired by spider dragline silk.* Nature Communications, 2014. **5**: p. 3322.

97. Fennimore, A.M., et al., *Rotational actuators based on carbon nanotubes.* Nature, 2003. **424**(6947): p. 408-410.

98. Lima, M.D., et al., *Electrically, Chemically, and Photonically Powered Torsional and Tensile Actuation of Hybrid Carbon Nanotube Yarn Muscles.* Science, 2012. **338**(6109): p. 928-932.

99. Zhang, D.B., R.D. James, and T. Dumitrică, *Electromechanical characterization of carbon nanotubes in torsion via symmetry adapted tight-binding objective molecular dynamics.* Physical Review B, 2009. **80**(11): p. 115418.

100. Jeong, B.-W., J.-K. Lim, and S.B. Sinnott, *Elastic torsional responses of carbon nanotube systems.* Journal Of Applied Physics, 2007. **101**(8): p. 084309.

101. Qian, D., W.K. Liu, and R.S. Ruoff, *Load transfer mechanism in carbon nanotube ropes.* Composites Science and Technology, 2003. **63**(11): p. 1561-1569.

102. Harris, J.M., et al., *Electronic Durability of Flexible Transparent Films from Type-Specific Single-Wall Carbon Nanotubes.* ACS Nano, 2012. **6**: p. 881-887.

103. Kim, J.-W., et al., *Polyaniline/Carbon Nanotube Sheet Nanocomposites: Fabrication and Characterization.* ACS Applied Materials & Interfaces, 2013. **5**(17): p. 8597-8606.

104. Bruss, I.R. and G.M. Grason, *Topological defects, surface geometry and cohesive energy of twisted filament bundles.* Soft Matter, 2013. **9**(34): p. 8327-8345.

105. Bruss, I.R. and G.M. Grason, *Non-Euclidean geometry of twisted filament bundle packing.* Proceedings of the National Academy of Sciences, 2012. **109**(27): p.

10781-10786.

106. Grason, G.M., *Frustration and packing in curved-filament assemblies: from isometric to isomorphic bundles.* Soft Matter, 2013. **9**(29): p. 6761-6772.

107. Mirzaeifar, R., Z. Qin, and M.J. Buehler, *Mesoscale mechanics of twisting carbon nanotube yarns.* Nanoscale, 2015. **7**(12): p. 5435-5445.

108. Vilatela, J.J., J.A. Elliott, and A.H. Windle, *A Model for the Strength of Yarn-like Carbon Nanotube Fibers.* ACS Nano, 2011. **5**(3): p. 1921-1927.

109. Wales, D.J., H. McKay, and E.L. Altschuler, *Defect motifs for spherical topologies.* Physical Review B, 2009. **79**(22): p. 224115.

110. Love, A.E., *Treatise on the Mathematical Theory of Elasticity*. 1927: Dover Books.

111. Costello, G.A., *Theory of Wire Rope*. 2007: Springer-Verlag: New York.

112. Shang, Y., et al., *Highly Twisted Double-Helix Carbon Nanotube Yarns.* ACS Nano, 2013. **7**(2): p. 1446-1453.

113. Fagan, J.A., et al., *Length fractionation of carbon nanotubes using centrifugation.* Adv. Mater., 2008. **20**: p. 1609-1613

114. Arnold, M.S., et al., *Sorting carbon nanotubes by electronic structure using density differentiation.* Nat Nano, 2006. **1**(1): p. 60-65.

115. Yanagi, K., Y. Miyata, and H. Kataura, *Optical and conductive characteristics of metallic single-wall carbon nanotubes with three basic colors; Cyan, magenta, and yellow.* Appl. Phys. Express 2008. **1**: p. 034003.

116. Baughman, R.H., A.A. Zakhidov, and W.A.d. Heer, *Carbon nanotubes - the route toward applications.* Science, 2002. **297**: p. 787-792

117. Wu, Z., et al., *Transparent, conductive carbon nanotube films.* Science, 2004. **305**: p. 1273.

118. Cao, Q. and J.A. Rogers, *Ultrathin films of single-walled carbon nanotubes for electronics and sensors: A review of fundamental and applied aspects.* Adv. Mater., 2008. **21**: p. 29-53

119. Hobbie, E.K., et al., *Wrinkling and strain softening in single-wall carbon nanotube membranes.* Phys. Rev. Lett., 2010. **104**: p. 125505.

120. Harris, J.M., et al., *Structural stability of transparent conducting films assembled from length purified single-wall carbon nanotubes.* J. Phys. Chem. C, 2011. **115**: p. 3973-3981

121. Harris, J.M., et al., *Elasticity and rigidity percolation in networks of type-purified single-wall carbon nanotubes on flexible substrates.* Soft Matter 2013. **9**: p. 11568-11575

122. Hobbie, E.K., et al., *Empirical evaluation of attractive van der Waals potentials for type-purified single-walled carbon nanotubes.* Phys. Rev. B, 2012. **85**: p. 245439.

123. Dumitrică, T., M. Hua, and B.I. Yakobson, *Symmetry-, time-, and temperature-dependent strength of carbon nanotubes.* Proc. Natl. Acad. Sci. USA 2006. **103**: p. 6105-6109.

124. Kim, K., M. Tsui, and M. Islam, *Graphene-Coated Carbon Nanotube Aerogels Remain Superelastic While Resisting Fatigue and Creep Over -100 °C to 500 °C.* Chem. Mater., 2017.

125. Kim, K.H., Y. Oh, and M.F. Islam, *Graphene coating makes carbon nanotube aerogels superelastic and resistant to fatigue.* Nat Nano, 2012. **7**(9): p. 562-566.

126. Krasheninnikov, A.V. and F. Banhart, *Engineering of nanostructured carbon materials with electron or ion beams.* Nat. Mater., 2007. **6**: p. 723-728.

127. Filleter, T. and H.D. Espinosa, *Multi-scale mechanical improvement produced in carbon nanotube fibers by irradiation cross-linking.* Carbon, 2013. **56**: p. 1-10.

128. O'Brien, N.P., M.A. McCarthy, and W.A. Curtin, *Improved inter-tube coupling in CNT bundles through carbon ion irradiation.* Carbon, 2013. **51**: p. 173-184.

129. Wang, C., et al., *Electronically selective chemical functionalization of carbon nanotubes: Correlation between Raman spectral and electrical responses.* J. Am. Chem. Soc., 2005. **127** p. 11460-11468.

130. Ostanin, I., R. Ballarini, and T. Dumitrică, *Distinct element method for multiscale modeling of cross-linked carbon nanotube bundles: From soft to strong nanomaterials.* Journal of Materials Research, 2015. **30**(01): p. 19-25.

131. Mielke, S.L., et al., *The role of vacancy defects and holes in the fracture of carbon nanotubes.* Chemical Physics Letters, 2004. **390**(4–6): p. 413-420.

132. Charlier, J.C., *Defects in Carbon Nanotubes.* Accounts of Chemical Research, 2002. **35**(12): p. 1063-1069.

133. Hembram, K.P.S.S. and G.M. Rao, *Origin of structural defects in multiwall carbon nanotube.* Materials Letters, 2012. **72**(0): p. 68-70.

134. Petrik, L., P. Ndungu, and E. Iwuoha, *Hall Measurements on Carbon Nanotube Paper Modified With Electroless Deposited Platinum.* Nanoscale Research Letters, 2010. **5**(1): p. 38-47.

135. Whitby, R.L.D., et al., *Geometric control and tuneable pore size distribution of buckypaper and buckydiscs.* Carbon, 2008. **46**(6): p. 949-956.

136. Sears, K., et al., *Recent Developments in Carbon Nanotube Membranes for Water Purification and Gas Separation.* Materials, 2010. **3**(1): p. 127.

137. Harris, J.M., et al., *Nature of Record Efficiency Fluid-Processed Nanotube–Silicon Heterojunctions.* The Journal of Physical Chemistry C, 2015. **119**(19): p. 10295-10303.

138. Rigoni, F., et al., *A cross-functional nanostructured platform based on carbon nanotube-Si hybrid junctions: where photon harvesting meets gas sensing.* Scientific Reports, 2017. **7**: p. 44413.

139. Wang, S., et al., *High-Performance Carbon Nanotube Light-Emitting Diodes with Asymmetric Contacts.* Nano Letters, 2011. **11**(1): p. 23-29.

140. Rappe, A.K., et al., *UFF, a full periodic table force field for molecular mechanics and molecular dynamics simulations.* Journal of the American Chemical Society, 1992. **114**(25): p. 10024-10035.

141. Xu, M., et al., *Carbon Nanotubes with Temperature-Invariant Viscoelasticity from –196° to 1000°C.* Science, 2010. **330**: p. 364-1368.

142. Wang, C., et al., *Mechanotunable microstructure of Carbon Nanotube Networks.* ACS Macro Lett., 2012. **1**: p. 1176-1179.

143. Edwards, S.F., *The statistical mechanics of polymers with excluded volume.* Proceedings of the Physical Society, 1965. **85**(4): p. 613.

144. Xu, G., et al., *The feasibility of producing MWCNT paper and strong MWCNT film from VACNT array.* Applied Physics A, 2008. **92**(3): p. 531-539.

145. Zhu, H.W., et al., *Direct Synthesis of Long Single-Walled Carbon Nanotube Strands.* Science, 2002. **296**(5569): p. 884-886.

146. Ostanin, I., *Multiscale modeling of carbon nanotube materials with distinct element method*, in *Civil Engineering*. 2014, University of Minnesota: University of Minnesota Digital Conservancy. p. 146.

147. Raney, J.R., et al., *In situ synthesis of metal oxides in carbon nanotube arrays and mechanical properties of the resulting structures.* Carbon, 2012. **50**(12): p. 4432-4440.

148. Park, H.-A., et al., *High visible-light photochemical activity of titania decorated on single-wall carbon nanotube aerogels.* RSC Advances, 2016. **6**(27): p. 22285-22294.

149. Jae Hyun, L., et al., *Tin nanoparticle thin film electrodes fabricated by the vacuum filtration method for enhanced battery performance.* Nanotechnology, 2009. **20**(23): p. 235203.

150. Mandal, R. and R.J. Anthony, *Aging of Silicon Nanocrystals on Elastomer Substrates: Photoluminescence Effects.* ACS Applied Materials & Interfaces, 2016. **8**(51): p. 35479-35484.

151. Wang, Y., et al., *Mechanical properties of self-assembled nanoparticle membranes:*

stretching and bending. Faraday Discussions, 2015. **181**(0): p. 325-338.

152. Kim, K.H., Y. Oh, and M.F. Islam, *Mechanical and Thermal Management Characteristics of Ultrahigh Surface Area Single-Walled Carbon Nanotube Aerogels.* Advanced Functional Materials, 2013. **23**(3): p. 377-383.

153. Simoes, R., et al., *Applications of the Graph Theory to the Prediction of Electrical and Dielectric Properties of Nano-filled Polymers.* Composite Interfaces, 2010. **17**(5-7): p. 407-422.

154. Huang, C., et al., *Capturing Electrochemically Evolved Nanobubbles by Electroless Deposition. A Facile Route to the Synthesis of Hollow Nanoparticles.* Nano Letters, 2009. **9**(12): p. 4297-4301.

155. Shan, Z.W., et al., *Ultrahigh stress and strain in hierarchically structured hollow nanoparticles.* Nat Mater, 2008. **7**(12): p. 947-952.

156. Cabot, A., et al., *Sulfidation of Cadmium at the Nanoscale.* ACS Nano, 2008. **2**(7): p. 1452-1458.

157. Valentini, P., W.W. Gerberich, and T. Dumitrică, *Phase-Transition Plasticity Response in Uniaxially Compressed Silicon Nanospheres.* Physical Review Letters, 2007. **99**(17): p. 175701.

158. Hale, L.M., et al., *Dislocation morphology and nucleation within compressed Si nanospheres: A molecular dynamics study.* Computational Materials Science, 2012. **54**: p. 280-286.

159. Tadmor, E.B., M. Ortiz, and R. Phillips, *Quasicontinuum analysis of defects in solids.* Philosophical Magazine A, 1996. **73**(6): p. 1529-1563.

160. Dupont, V. and F. Sansoz, *Multiscale Modeling of Contact-Induced Plasticity in Nanocrystalline Metals*, in *Trends in Computational Nanomechanics: Transcending Length and Time Scales*, T. Dumitrica, Editor. 2010, Springer Netherlands: Dordrecht. p. 151-172.

161. Péron-Lührs, V., et al., *Multiscale computational modeling of deformation mechanics and intergranular fracture in nanocrystalline copper.* Computational Materials Science, 2014. **90**: p. 253-264.

162. Meyers, M.A., A. Mishra, and D.J. Benson, *Mechanical properties of nanocrystalline materials.* Progress in Materials Science, 2006. **51**(4): p. 427-556.

163. Potyondy, D.O. and P.A. Cundall, *A bonded-particle model for rock.* International Journal of Rock Mechanics and Mining Sciences, 2004. **41**(8): p. 1329-1364.

164. Kachanov, L.M., *Fundamentals of the Theory of Plasticity*. 2004, Mineola, New York:

Dover Publications.

165. Shams, A. and M. Porfiri, *Axisymmetric static and dynamic buckling of hollow microspheres.* International Journal of Non-Linear Mechanics, 2014. **61**: p. 19-31.

166. Landau, L.D., and Lifshitz, E. M., *Theory of Elasticity (Volume 7 of A Course of Theoretical Physics)*. 1970, Pergamon.

167. Lund, M.S., Oh, Y., Smith, A., Muangphat, C., Stauffer, D. D., Huang, C., Hao, Y., Major, R. C., Meletis, E. I., and Gerberich, W. W. *Compression of Hollow Gold Spheres Using an Ultra-Low Noise MEMS Transducer*. in *GRC Noble Metal Nanoparticles*. 2014. South Hadley, MA.

168. Gall, K., J. Diao, and M.L. Dunn, *The Strength of Gold Nanowires.* Nano Letters, 2004. **4**(12): p. 2431-2436.

169. Rockenberger, J., et al., *The contribution of particle core and surface to strain, disorder and vibrations in thiolcapped CdTe nanocrystals.* The Journal of Chemical Physics, 1998. **108**(18): p. 7807-7815.

170. Van Swygenhoven, H. and J.R. Weertman, *Deformation in nanocrystalline metals.* Materials Today, 2006. **9**(5): p. 24-31.

171. Benjamin, D.J., E.W. Kristopher, and M.O. Gregory, *Simulation of mechanical performance limits and failure of carbon nanotube composites.* Modelling and Simulation in Materials Science and Engineering, 2016. **24**(2): p. 025012.

172. Downes, R.D., et al., *Geometrically constrained self-assembly and crystal packing of flattened and aligned carbon nanotubes.* Carbon, 2015. **93**: p. 953-966.

173. Satti, A., et al., *Covalent crosslinking of single-walled carbon nanotubes with poly(allylamine) to produce mechanically robust composites.* Journal of Materials Chemistry, 2010. **20**(37): p. 7941-7943.

174. O'Brien, N.P., M.A. McCarthy, and W.A. Curtin, *Improved inter-tube coupling in CNT bundles through carbon ion irradiation.* Carbon, 2013. **51**(0): p. 173-184.

175. Cui, Y. and M. Zhang, *Cross-links in Carbon Nanotube Assembly Introduced by Using Polyacrylonitrile as Precursor.* ACS Applied Materials & Interfaces, 2013. **5**(16): p. 8173-8178.

176. Chen, J., et al., *Solution Properties of Single-Walled Carbon Nanotubes.* Science, 1998. **282**(5386): p. 95-98.

177. Zhang, J., et al., *Effect of Chemical Oxidation on the Structure of Single-Walled Carbon Nanotubes.* The Journal of Physical Chemistry B, 2003. **107**(16): p. 3712-3718.

178. Hall, D.M., et al., *Morphology selection via geometric frustration in chiral filament*

bundles. Nat Mater, 2016. **15**(7): p. 727-732.

179. Lee, G., et al., *Self-assembled amyloid fibrils with controllable conformational heterogeneity.* Scientific Reports, 2015. **5**: p. 16220.

180. Wang, Y., et al., *Emerging chirality in nanoscience.* Chemical Society Reviews, 2013. **42**(7): p. 2930-2962.

181. Griffith, A.A., *The Phenomena of Rupture and Flow in Solids.* Philosophical Transactions of the Royal Society of London. Series A, Containing Papers of a Mathematical or Physical Character, 1921. **221**(582-593): p. 163-198.

182. Yang, W., et al., *On the tear resistance of skin.* Nature Communications, 2015. **6**: p. 6649.

Appendix A

As observed in some experimental works, CNT rings are usually in forms of bundles, which contain many organized single wall CNTs. The ideal CNT bundles are often organized in hexagonal shape shown in Figure A-1. The previous discussion indicated three types of bonds should be considered. The vdw potential coefficients of these three bonds are D_1 = -2.24 eV/nm, D_2 = -0.96 eV/nm and D_3 = -0.04 eV/nm. This coefficient approaches to zero as the distance between tubes increases. Bond longer than D_3 will have negligible effect. Therefore, to simplify the calculation of vdW potential inside the bundle, only D_1, D_2 and D_3 are included. Total number of tubes in the bundle *n* can be expressed based on number of layer *N* as the following equation:

$$n = (3N - 1)N - (2N - 1) = 3N^2 - 3N + 1.$$

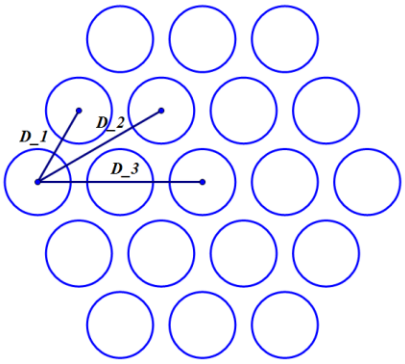

Figure A-1 Configuration of CNT bundle with 3 layers

Consideration of D_1 bonds

The vdw interaction between adjacent CNT is D_1. It is convenient to count the total number of D_1 bond in three directions. For example, when we consider X1 direction, only the D_1 bond parallel to X1 direction will be counted. Since the three directions are equivalent, the total number of D_1 bond is three times of that of each direction.

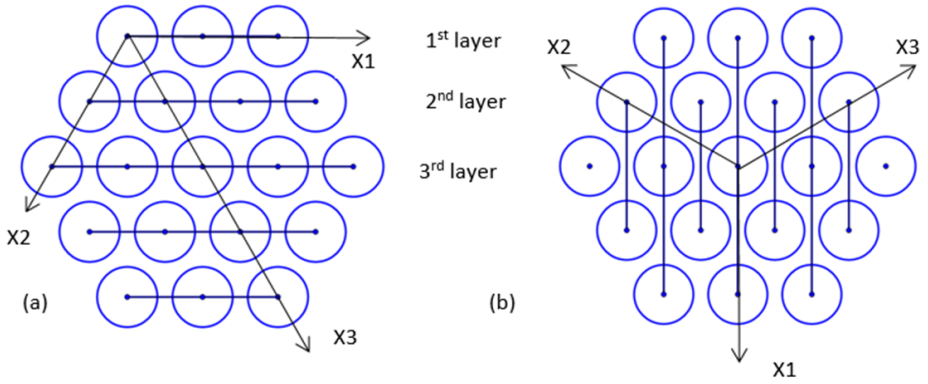

Figure A-2 Schematic diagram of counting (a) D_1 and (b) D_2 bonds

We could define the number of layers in the bundle as n. The first layer containing n tubes has N-1 D_1 bond. The second layer has N+1 tubes but n D_1 bonds. The $(N\text{-}1)^{th}$ layer will have N+N-2 tubes but N+N-3 D_1 bonds. The N^{th} layer will then have N+N-2 bonds. Due to symmetry, it is only necessary to count the upper part of this geometry. Given an N-layer bundle, the total number of D_1 bonds in one direction would be described as:

$$Number\ of\ D_1 bond\ in\ X1\ direction = [(N-1)+N+(N+1)+\cdots(N+N-3)]\times 2 + (N+N-2) = (3N-4)(N-1)+(2N-2).$$

Consideration of D2 bonds

The count of D_2 bond follows the same method. Three directions are firstly defined as in Figure A-2b. In X1 direction, only D_2 bonds parallel to this direction are counted. The first layer has n tubes and n D_2 bonds. The second layer contains N+1 tubes and also N+2 D_2 bonds. The $(N\text{-}1)^{th}$ layer includes N+N-2 D_2 bonds, which connect the upper part and lower part and should be counted once.

$$Number\ of\ D_2\ bond\ in\ X1\ direction = [N+(N+1)+(N+2)\ldots(N+N-2)]\times 2-(N+N-2) = (3N-2)(N-1)-(2N-2).$$

Consideration of D_3 bonds

D_3 bond can also be counted with the same method layer by layer. In X1 direction of Figure 2 (a), first layer has *N*-2 D_3 bonds and second layer has *N*-2+1. Then the $(n\text{-}1)^{th}$ layer will have *N*-2+*N*-2 D_3 bonds. The middle layer has *N*-2+*N*-1 D_3 bonds, which should be counted only once.

$$Number\ of\ D_3\ bond\ in\ X1\ direction = [N-2+(N-2+1)+(N-2+2)\ldots(N-2+N-2)]\times 2+(N-2+N-1) = (3N-6)(N-1)+(2N-3).$$

By knowing the number of D_1, D_2 and D_3 bonds, the vdW interaction per length inside the tube is ready to be calculated:

$$\zeta_n = [(3N-4)(N-1)+(2N-2)]\cdot 3D_1 + [(3N-2)(N-1)-(2N-2)]\cdot 3D_2 + [(3N-6)(N-1)+(2N-3)]\cdot 3D_3 = (3N^2-5N+2)V_1 + (3N^2-7N+4)V_2 + (3N^2-7N+3)V_3 - 19.251N^2 + 32.235N - 12.963\ \ eV/nm.$$

For *N*-1 case, the number of D_1, D_2 and D_3 bonds will be reduced by 3, 2 and 3. Therefore, the cohesive energy coefficients can be obtained by the following equation:

$$\zeta_{n-1} = -19.251N^2 + 32.235N - 6.564\ \ eV/nm.$$

The vdW energy can then be calculated:

$$U_{vdw} = [N\zeta_n - (N-1)\zeta_{n+1}]L + [N\zeta_{n+1} - (N+1)\zeta_n]\Delta l;$$

$$U_{tot}(L,\Delta l) = U_{vdw}(L,\Delta l) + U_{strain}(L,\Delta l) = [N\zeta_n - (N-1)\zeta_{n+1}]L + [N\zeta_{n+1} - (N+1)\zeta_n]\Delta l + 2\pi^2 B\frac{L}{(L-\Delta l)^2};$$

$$\frac{dU_{tot}}{d\Delta l} = [N\zeta_{N+1} - (N+1)\zeta_n] + 4\pi^2 BL(L-\Delta l)^{-3} = 0;$$

$$\Delta l_{n\ turns} = L - \sqrt[3]{\frac{-4\pi^2}{[N\zeta_{n+1}-(N+1)\zeta_N]}BL}. \qquad (1)$$

Here, we assume Δl has some critical values, which equal to the boundary values of each piecewise function.

$$\Delta l_{n\ turns} = \frac{n-1}{n} L. \qquad (2)$$

Solve equations (1) and (2), the shortest required length can be estimated.

$$\frac{n-1}{n} L = L - \sqrt[3]{\frac{-4\pi^2}{[n\zeta_{n+1} - (n+1)\zeta_n]} BL};$$

$$L = N^{1.5} \sqrt{\frac{-4\pi^2}{[N\zeta_{n+1} - (n+1)\zeta_n]} B}.$$

Appendix B

Fig. 3-7a was observed during the characterization of HiPCO SWCNTs that were purified through thermal oxidation at 260 ºC, refluxing in HCl solution, and ultrasonication in nitric acid. Colloidal suspensions were then made from the purified SWCNT powder by sonicating the material in an aqueous solution of sodium dodecylbenzenesulfonate surfactant (SDBS, 0.6% by mass). After cold ultrasonication of the surfactant solution for 10 h, the nanotubes exist as 'ropes' or SWCNT bundles. Atomic-force microscopy (AFM) performed on dried films cast from dilute suspensions gave a mean bundle diameter of 13.5 nm and a mean length of 750 nm.[9] The AFM image shown in Fig. 3-7a was obtained by casting droplets of dilute SWCNT suspension on smooth silicon substrates and repeatedly wicking away excess isopropanol solution. Tapping-mode AFM measurements were performed in air using a Nanoscope IV AFM (Digital Instruments) operated under ambient conditions with phosphorusdoped silicon tips (Veeco; RTESP5, 125 μm length; 30 μm width, normal spring constant, 40 N/m; resonance frequency, 240 kHz to 300 kHz).

For the knot and racket images shown in Fig. 3-7b, c and d, CoMoCat SWCNTs were dispersed in water via ultrasonication with 2% sodium deoxycholate (DOC) surfactant, coarsely centrifuged to remove impurities and bundles, and then purified by length using transient density-gradient ultracentrifugation in aqueous iodixanol solutions. The fraction of interest here was dispersed to the level of individual SWCNTs with mean length of order 700 nm and mean diameter of order 1 nm.[10,11] For AFM characterization, silicon wafers were functionalized with 3-(ethoxydimethylsilyl)-propylamine (APDMES,

[9] D. Fry, et al. Phys. Rev. Lett., 2005, 95, 038304.

[10] J. A. Fagan, et al. ACS Nano, 2013, 7, 3373.

[11] J. A. Fagan, et al. Langmuir, 2008, 24, 13880.

Sigma- Aldrich) by cleaning in a UVO chamber for 15 min followed by immersion into 1% APDMES in isopropanol for 20 min and subsequent rinsing with isopropanol and DI water. The wafers were dried in an oven at 70 ºC for 20 min. SWCNT samples in 10 g L^{-1} DOC were diluted at least $100\times$ with an aqueous solution of 0.2 wt% sodium cholate and 20 mM sodium thiocyanate and deposited on a wafer by casting (5 to 20) μL of the sample, followed by incubation in a closed container for 8 min. After incubation, samples were blown dry using canned nitrogen. AFM imaging was done on a Bruker Dimension Icon AFM in the peakforce tapping mode using ScanAsyst-Air probes.[12]

The measurement of CNT rings and rackets presented in Fig. 3-12 is presented as the following. We diluted a 1% DOC solution of the length-enriched CoMoCat SWCNTs described previously by a factor of 250:20 with purified DI water. Silicon wafer substrates were ultra-sonicated in acetone for 20 min, exposed to UVO plasma for 15 min, and then rinsed with DI water and dried under N_2 several times. The substrates were observed under $50\times$ magnification to ensure cleanliness and then annealed in the SWCNT solution for 2 h before submerging them in an ethanol bath for 19 h to remove all DOC. The sample was then rinsed with ethanol and water several times and dried under N_2. To measure structure dimensions, AFM scans $20\ \mu m \times 20\ \mu m$ in area were collected to identify surfactant-free regions with an appropriate density of nanotubes. When such areas were located, $5\ \mu m \times 5\ \mu m$ scans were made at a scan rate of 3 lines per second. Measurements were made on a Veeco DI- 3100 AFM in tapping mode using Golden Si NSG01 bare 10 nm probes. The in-plane shape dimensions of the observed rackets and rings are large enough to be easily resolved with the 10 nm probes, while the diameters of the constituent ropes were determined from height measurements, which have a much better resolution.

[12] C. Y. Khripin, et al. Anal. Chem., 2013, 85, 1382.